RWTH Aachen University

Master Thesis

Probing the Periodicity of Active Galactic Nuclei with the First G-APD Cherenkov Telescope

---

Author:
Max Mahlke

Supervisor:
Prof. Dr. Thomas Bretz
Prof. Dr. Thomas Hebbeker

*A thesis submitted in partial fulfilment
of the requirements for the degree of*

Master of Science (MSc.)

at the

Physikalisches Institut 3A
Department of Physics

Aachen, September 2017

ABSTRACT

Active galactic nuclei are cosmic laboratories for high-energy physical phenomena. Their erratic variability in TeV γ-rays is seen as key to disentangling the complexity of the numerous intrinsic processes. Theories predict periodic modulations of the γ-ray emission, e.g. for binary black hole scenarios.

Since the first observation of a TeV γ-ray source in 1989, 200 additional sources have been appended to the catalogue of these cosmic accelerators. A multitude of Cherenkov telescope is dedicated to the discovery and understanding of these enigmatic sources.

The *First G-APD Cherenkov Telescope* is pioneering the long-term monitoring of the γ-ray emission of the brightest blazars in the sky using a camera made of silicon photomultipliers. In order to treat the raw data, a heuristic model of the zenith angle dependence of the cosmic ray- and γ-ray rate is derived using basic assumptions from the Heitler model. The model function is used to identify bad-weather observation runs and to correct for the zenith angle dependence in the data.

The variability of the blazars Markarian 501 and Markarian 421 is assessed using a Lomb-Scargle periodogram analysis of the 5-year light curves acquired with the FACT telescope. The spectral indices of the Markarians correspond to flicker noise processes when accounting for the uneven sampling pattern using the spectral window. To investigate the periodicity of the intrinsic red-noise processes, light curves of stochastic processes are simulated and the distribution of powers in their periodograms is evaluated. The periodograms of both Markarian 501 and Markarian 421 are consistent with stochastic processes without underlying periodic modulations.

CONTENTS

INTRODUCTION

1.1 TIME-SERIES ANALYSIS IN ASTRONOMY AND ASTROPHYSICS

Time-series analysis is the fundamental tool in astronomy and astrophysics. Astronomers observe the light arriving from distant objects over time and look for repeating patterns, developing theories through inductive reasoning. Galileo Galilei's discovery of the four largest satellites of Jupiter, the Galilean Moons, is a prime example of this type of analysis. Figure 1.1a shows the time-series Galilei recorded in 1610.

While observations in past centuries were limited to the visible light and, more often than not, the naked eye, today's observations are far more sophisticated, observing sources over the whole range of the electromagnetic spectrum with large magnifications. However, it remains that observations come down measuring the amount of emitted light over time, an example of which being the discovery of the planetary system around TRAPPIST-1, in a distance of 12 light-years from Earth (Gillon et al. 2017), see Figure 1.1b.

The close connection between time-series analysis and astronomy and astrophysics derives from the distances and dimensions of the objects of interest. There is no technology allowing for repeated observations under different initial conditions, nor can the sources be replicated in laboratories to be examined from within.

(a)   (b)
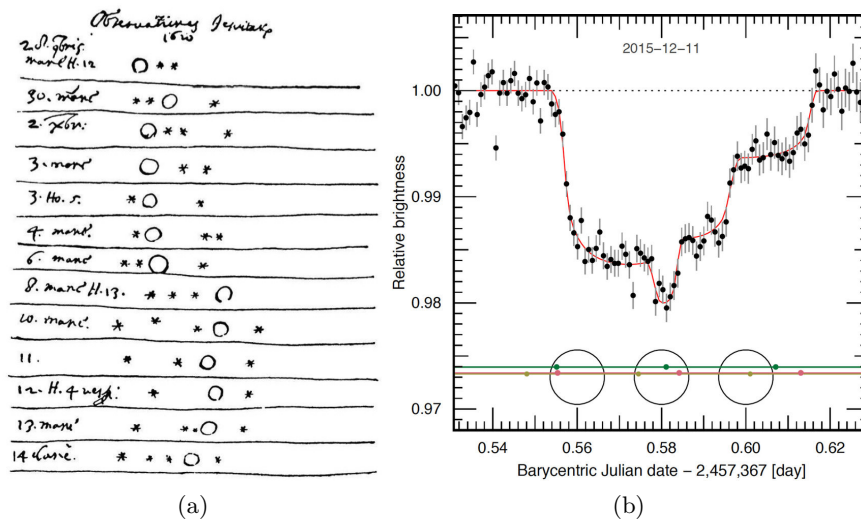
Figure 1.1 *Time-Series Analysis of Periodic Processes* Time-series analysis is the fundamental tool in astronomy and astrophysics. While the instruments have become more sophisticated, the principle research does not differ by much between Galilei's study of the Galilean moons in 1610 and Gillon et al. (2017) observations of the TRAPPIST-1 system in 2015. Figure Credit: [http://www.physast.uga.edu/~rls/astro1020/, Gillon et al. (2017)]

The aim of this thesis can therefore be stated as follows: The amount of light over time emitted from two galaxies, Markarian 501 and Markarian 421, is searched for repeating patterns. In Chapter 2, the non-thermal Universe that these galaxies are part of is outlined. Current models regarding the generation of photons in their source class are presented, with focus on the free parameters in the models that might be constrained by revealing patterns in the light curves. The enigmatic active galactic nuclei are presented, with a closer look on the subclass of the blazars and their variability. The chapter concludes with an overview of proposed mechanisms for periodicity in active galactic nuclei.

Chapter 3 introduces the instruments that observe the very-high energy sky, with special emphasis on the First G-APD Cherenkov Telescope (FACT), the instrument which provides the time-series for this analysis. By looking at the field-of-view of FACT, challenges and repeating patterns in the observation process of sources are pointed out. The distinction between FACT and other VHE γ-ray observatories is outlined.

The treatment of the raw-data recorded by FACT is the subject of Chapter 4. The detection principle of imaging atmospheric Cherenkov telescopes is explained, followed by a heuristic model of the zenith angle dependence of the photon rate measured by the FACT telescope. This model is then used to derive an indicator of bad weather during observations and to correct for the zenith angle dependence in the γ-ray flux.

The heart of the thesis is the search for periodicity in the blazars Markarian 501 and Markarian 421 in Chapter 5. The assessment of variability of data in time-space naturally leads to a look into to Fourier-realm. Here, it is outlined that the gaps in the observations lead to unevenly-sampled light curves, which make statistical interpretation of the data challenging. This challenge is tackled by means of Monte Carlo simulations of the light curves of stochastic processes..

The achieved results, conclusions, and an outlook on the work to come is given in Chapter 6.

1.2 REPRODUCIBLE RESEARCH

The results and figures presented in this thesis are the products of an in-depth analysis. While the thesis aims to describe every step of the data treatment from raw data to interpretation of the results, the reader may not be satisfied with the presented explanation and might want to retrace the steps themselves. Especially in data driven sciences like astronomy and astrophysics, reproducibility is becoming increasingly more difficult due to the required computational architectures, data availability, or the availability of the analysis pipeline. While the first two points are not within the power of the author, the latter is. In order to allow for the reproducibility of the results, all code used to generate figures in this thesis is publicly available at https://git.rwth-aachen.de/tbretz/fact/tree/master/mahlke2017.

While the author *cannot* guarantee that the presented conclusions are correct, he can guarantee that running the analysis with the provided code will yield the same results. Reproducibility, therefore, does not mean correctness, but transparency. Details on the structure of the repository and software used are given in Appendix B.

2

THE TeV γ-RAY UNIVERSE

The research in *very-high energy* (VHE, $E \geq 100\,\text{GeV}$) astrophysics probes the non-thermal Universe by means of messenger particles called *cosmic rays* (CR). The emitters of these cosmic messengers are the most extreme regions in the Universe in terms of physical conditions. Examples are the shock waves in supernova remnants, the interaction of ultra-relativistic particle winds of neutron stars with the surrounding medium forming a *pulsar wind nebula* (PWN), and accreting supermassive black holes at the centre of galaxies, so called *active galactic nuclei* (AGN). The exotic phenomena in these sources have fascinated researches in astrophysics for decades, being cosmic laboratories for theories such as quantum physics and general relativity.

While the thermal Universe, consisting of the light emitted mostly by stars, has been studied to a great extent in the wavelength range of visible light for centuries, the window to the non-thermal Universe and its members was opened in the astronomically speaking recent past by Victor Hess with the discovery of CR radiation (Hess 1912). In order to locate the sources of CRs, the messenger particles have to be traced back to their point of origin. However, the trajectories of charged CRs are subject to deflection by the intra- and extragalactic magnetic fields. As the strength and alignments of these fields are not well known, the CRs appear to come from random directions.

Instead, the measurement of neutral particles like photons and neutrinos is more promising in terms of discovering and characterising sources of the non-thermal Universe. These messenger particles are the products of the interaction of CRs with the *interstellar medium* (ISM). Their observation is a challenging task but promises direct insights into the source's intrinsic mechanisms.

In this work, the observation and interpretation of VHE γ-rays coming from AGN is in the focus. This chapter aims to give a brief overview of current models of the acceleration mechanisms of photons in astrophysical sources before introducing the enigmatic AGN, with a focus on a subclass of *blazars*. Further emphasis is placed on the variability of the measured light curves of these sources and on proposed mechanism for the emission of periodic signals in AGN.

The reader interested in a thorough review of the development of VHE γ-ray astronomy is pointed to Lorenz and Wagner (2012) and to Horan and Weekes (2003) and de Naurois and H.E.S.S. Collaboration (2013) for an overview of the galactic and extragalactic sources in the non-thermal Universe.
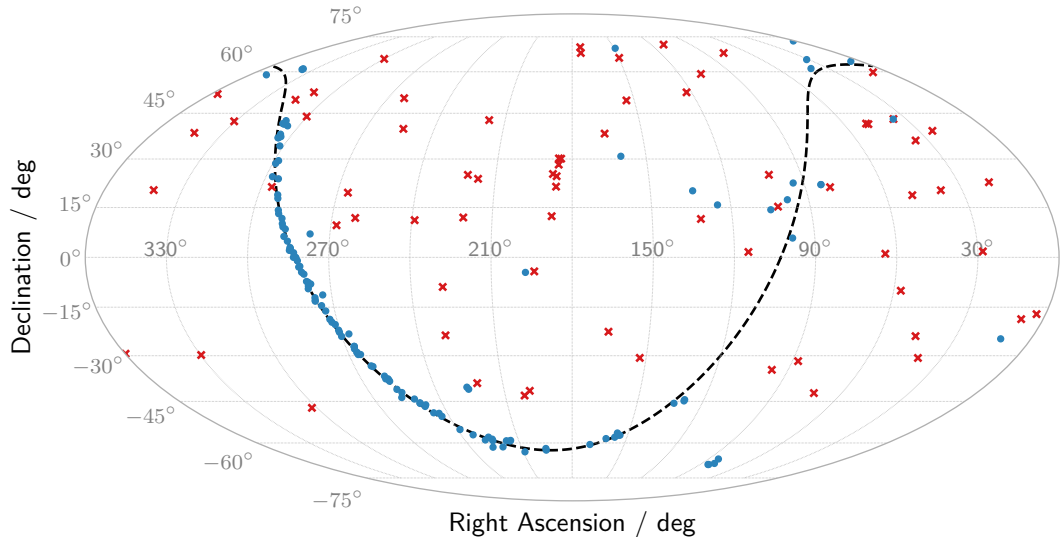
Figure 2.1 *The TeV γ-ray Sky* The 201 sources currently listed in the TeVCat. Plotted are their coordinates in right ascension and declination using the equal-area Mollweide projection. The dashed, black line marks the galactic plane. The red crosses mark the coordinates of active galactic nuclei, which are the most abundant extragalactic sources of TeV γ-rays. The blue dots are sources which are not AGN, mostly consisting of galactic pulsar wind nebulae. The TeVCat can be found at http://tevcat.uchicago.edu.

2.1 ASTROPHYSICAL ORIGINS OF γ-RAYS

The production of VHE γ-rays occurs in sources where accelerated CRs interact with the ambient matter of the ISM and the surrounding radiation fields. Since the first detection of a source of TeV photons in 1989, 200 discoveries have been appended to the catalogue of TeV sources.[1] Galactic sources of TeV photons are mostly PWNe, the most abundant extragalactic sources are the AGN, see Figure 2.1.

The *electromagnetic* (EM) emission of astrophysical sources ranges from radio to γ-rays. In order to compare the emission in different wavebands, a quantity is required which unifies the measured emission in different frequencies and with different detectors. The *spectral flux density* $F(\nu)$ is defined as the rate of energy is which transmitted by electromagnetic radiation at a certain frequency through a unit surface area. Multiplying with frequency of the electromagnetic radiation gives the *flux density*,

$$J(\nu) = \nu F(\nu), \quad [J(\nu)] = \mathrm{erg\, cm^{-2}\, s^{-1}} \tag{2.1}$$

which is used to compare the emission detected by the experiments in different wavebands. The *spectral energy distribution* (SED) or just *spectrum* of a source is its flux density in dependence of the energy or frequency of the emitted radiation. The SED of astrophysical sources is the common quantity to compare their emission spectra (Spurio 2014).

---

1 http://tevcat.uchicago.edu

The generation of photons through the interaction of CRs with the ISM is mainly attributed to three mechanisms. Synchrotron radiation of relativistic electrons[2] accelerated in ambient magnetic fields generates thermal photons with radio- to X-ray frequencies, refer to the red line in Figure 2.2. High-energy (HE, $\sim$30 MeV to 100 GeV) and VHE γ-rays are produced by two possible mechanisms, which are outlined now.

HADRONIC MODEL   A hadronic origin of γ-rays is based on two different proton-initiated particle cascades. The first process begins with collisions of protons or heavier nuclei with ambient protons or nuclei, which dominantly produce charged and neutral pions, with a smaller fraction made of higher mass mesons and baryons (Lorenz and Wagner 2012),

$$p + \text{nucleus} \rightarrow \pi^{\pm}, \pi^0, p', n, \dots \tag{2.2}$$
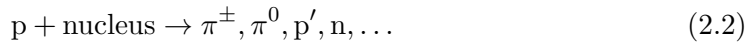
This process is referred to as *astrophysical beam dump*. In the second proton-initiated cascade, the high-energy protons interact with ambient low-energy photons hν in a process called *photoproduction*, again producing pions (Catanese and Weekes 1999),
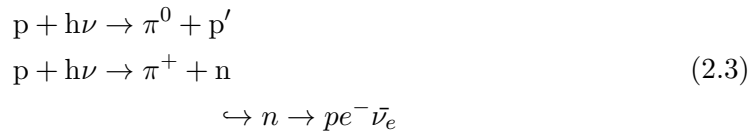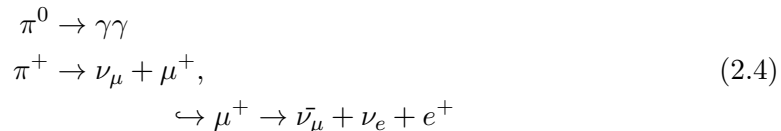
$$\begin{aligned} p + h\nu &\rightarrow \pi^0 + p' \\ p + h\nu &\rightarrow \pi^+ + n \\ &\hookrightarrow n \rightarrow pe^-\bar{\nu}_e \end{aligned} \tag{2.3}$$

The probability ratios between these two processes depends on the environment: For the beam dump mechanism, the determining variable is the ambient *matter* density, while for photoproduction, a high ambient *photon* density is crucial.

Both processes results in neutral and charged pions, which decay according to

$$\begin{aligned} \pi^0 &\rightarrow \gamma\gamma \\ \pi^+ &\rightarrow \nu_\mu + \mu^+, \\ &\hookrightarrow \mu^+ \rightarrow \bar{\nu}_\mu + \nu_e + e^+ \end{aligned} \tag{2.4}$$

The energy spectrum of the γ-ray particles emitted in the π^0 decay shows a steep rise at energies in the order of 100 MeV and traces the energy distribution of the parent proton particles. This characteristic shape is referred to as the pion-decay bump and can serve to identify γ-rays of hadronic origin, see the orange line in Figure 2.2 (Spurio 2014).

LEPTONIC MODEL   The leptonic production of γ-rays is caused by the *inverse-Compton* (IC) mechanism. Ambient low-energy photons hν created by the synchrotron radiation of high-energy electrons gain energy by scattering with high-energy electrons, which increases the photon energy by converting the electron's kinetic energy,

$$e + h\nu_{\text{low}} \rightarrow e_{\text{low energy}} + \gamma. \tag{2.5}$$

The source of the target photons might be the synchrotron radiation of the high-energy electrons themselves, in which case the process is referred to as *self-synchrotron*

---

2 Throughout the thesis, *electrons* refers to both electrons and positrons.

Compton. However, this requires strong ambient magnetic fields. Alternatively, the low-energy photons could be provided by an external process and fed into the IC region. The process is then called *external Compton.* The peak energies of the scattered photons are in the order of GeV to TeV. The shape of the high-energy IC peak in the SED depends the ambient photon density and the Lorentz factor of the relativistic electrons. The blue line in Figure 2.2 illustrates that it can be well approximated using power-laws in most parts of the spectrum (Lorenz and Wagner 2012; Spurio 2014).

Each interaction mechanism leaves its imprint in the SED of a source. Figure 2.2 shows a schematic of common SED models of astrophysical VHE γ-ray sources, illustrating the typical double-bump structure.
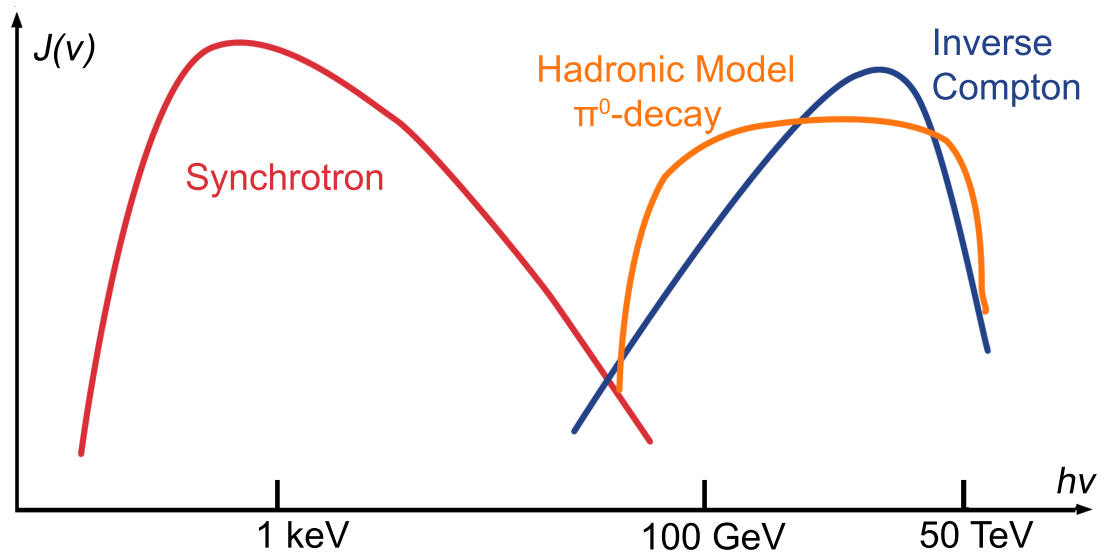

Figure 2.2 *Spectral Energy Distribution Models* The schematic of an SED of an astrophysical source emitting EM radiation from radio- to VHE γ-ray frequencies. Thermal radiation is usually attributed to synchrotron emission of relativistic electrons in a magnetic field (red line). HE and VHE γ-rays are produced in the decays of neutral pions (hadronic model, orange) or in IC scattering of relativistic electrons with photons of ambient radiation fields (leptonic model, blue). Mixed models assume the production of γ-rays by both processes in one source. After Spurio (2014).

Hadronic models are sometimes referred to as *lepto-hadronic* models to indicate that the contribution of leptons is taken into account as well. The fundamental difference between both models is therefore whether the heavy hadrons are accelerated to ultra-relativistic energies. The observation of ultra-high energy CRs suggests that at least in some sources, the VHE γ-rays are of hadronic origin (Dawson et al. 2017). While the observation of neutrinos emerging from a source would provide unambiguous prove that hadronic interactions are taking place, detecting neutrinos is a challenging endeavour due to their elusive nature, and requires large detector volumes and observation times.

As the SED is the characterizing measurement of astrophysical sources, it is used to model their inner processes. A fundamental question is what type of interaction process is responsible for the emission of the HE and VHE γ-rays. The leptonic and hadronic models require different environmental conditions, regarding e.g. the magnetic field strength, photon- or matter number densities. The identification of either process or

a mixed model could therefore lead to insights into the source and constrains of its parameters. However, the SED commonly spans 20 orders of magnitudes in frequency, and current measurements are in general not enough to restrict the leptonic or hadronic origin models sufficiently to rule out one or the other. As the SED of astrophysical sources is time-dependent, contemporaneous multi-wavelength measurements of SEDs as shown in e.g. in Abdo et al. (2011b) are essential to restrict model parameters.

2.2   THE CRAB NEBULA

The first source of the non-thermal Universe to be introduced here was also the first source to be detected in TeV γ-rays: the Crab Nebula, observed in 1989 by the Whipple Observatory (Weekes et al. 1989). Located at a distance of 2 kpc away from Earth,[3] the Crab Nebula belongs to the class of PWN. It consists of rotating neutron star, the Crab Pulsar, which emits magnetic dipole radiation and an ultra-relativistic wind into the remnants of a supernova explosion[4] (Hester 2008). The SED of the Crab Nebula is well described by the leptonic model: The shock between the cold pulsar wind and the hot plasma accelerates electrons and positrons to TeV energies. The accelerated particles interact with the ambient magnetic fields, emitting synchrotron radiation which can be observed from radio- up to the X-ray band. The synchrotron photons are then subject to IC scattering, boosting the photon energies to the TeV range (Aleksić et al. 2015).

Its luminous and long-term steady emission, especially in comparison to other TeV γ-ray sources, have made the Crab Nebula the standard candle of (VHE) astronomy, offering itself as calibration source to compare the performance of a telescope over time or to the performance of other instruments. Its luminosity furthermore serves as unit for TeV observations, where the flux of sources is then given in Crab units (CU). However, Abdo et al. (2011a) and Tavani et al. (2011) reported modulations of the flux levels in the form of flaring states over several days of the Nebula in the HE energy regime, likely linked to the Crab Pulsar.

2.3   ACTIVE GALACTIC NUCLEI

The observational features of AGN are highly dependent on their alignment with respect to the line-of-sight. Some sources are dominated by thermal radiation in the infrared, optical, or even X-ray. Others show large emissions over the whole EM spectrum, with especially high luminosities in the non-thermal wavebands, in HE and VHE γ-rays. The SEDs of AGN are time-dependent, as are the spectral emission lines. The sources are very bright, and far away. These puzzling observations are summarized in the term *quasar*, quasi-stellar object, which was introduced for the sources detected in radio sky surveys which appeared as star-like point sources in optical images but did not resemble any known stellar sources (Edge et al. 1959; Bennett and Simth 1962). In 1963, the red-shift of quasar 3C 273 was determined to be $z = 0.16$ via the Balmer emission lines of hydrogen, proving that quasars are extragalactic sources (Schmidt 1963).

---

3 A parsec (pc) equals 3.26 light-years.

4 The supernova which produced the remnant was recorded in the year 1054 A.D. by Chinese astronomers, who said that a "guest star" was visible over a period of three weeks, even during daytime (Green and Stephenson 2003).

Exposures of 3C 273 are shown in Figure 2.3, in the radio- (left plot), the optical- (middle plot), and the X-ray band (right plot). Different regions of the object light up at different frequencies.
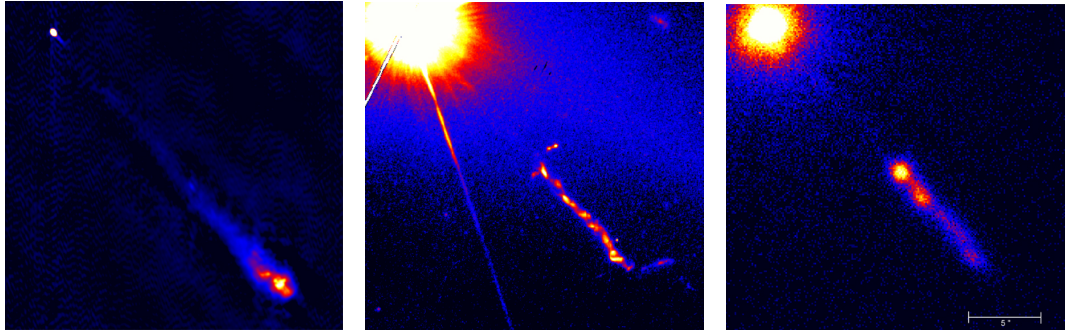

Figure 2.3 *Multi-Wavelength Structure of Quasar 3C 273* The left exposure depicts the quasar 3C 273 in the radio band, the middle one is taken in the optical, and the right one in the X-ray band. The core region of the AGN in the upper left corner flares up in all regimes due to thermal radiation of accreted matter close to the black hole and inverse-Compton scattering of high-energy electrons and thermal photons. Different parts of the relativistic jet can be observed in all three exposures. The scale shown in the bottom right corner of the X-ray exposure is 5". Credit: Radio: MERLIN, Optical: NASA/STScI, X-ray: NASA/CXC.

Three decades of observational efforts cumulated in the Grand Unified Theory of AGN by Urry and Padovani (1995), which concluded that the difference in the observed emission features is caused be the different inclinations of AGN to the line-of-sight to Earth. Nowadays, it is widely accepted that AGN are part of the typical life cycle of a galaxy, determining the properties of the host galaxy and vice versa (Heckman and Best 2014). Still, as their taxonomic classification is more historically than physically motivated, the terminology is often confusing. Some common properties of all AGN can be given nevertheless.

At the core of every AGN is a massive black hole, with masses larger than $10^5\,\mathrm{M}_\odot$ and going up to billions of solar masses or even higher (Rieger and Mannheim 2003). The Schwarzschild radius[5] of the black holes is in the order of light-seconds to light-days. The potential well of the black holes attracts matter and converts the potential energy of the surrounding medium into radiation, fuelling the output of the AGN. The mass of the black hole can therefore be estimated by measuring the luminosity of the AGN over all wavebands.

The black hole is surrounded by a hot, rotating accretion disk of dust, stabilized by the angular momentum of the attracted matter. Typical dimensions for the accretion disk are sub-parsec. It emits mainly thermal infrared, optical, and ultraviolet light. In Figure 2.3, the accretion disk is located in the top left of the exposures. The X-ray observation by the Chandra X-ray Observatory satellite shows that accretion disk is also visible at non-thermal wavelengths. One possible scenario for the emission of X-ray

---

5 The Schwarzschild radius of an object is defined as the radius of a sphere which, if it contained the whole mass of the object, would have an escape velocity larger than the speed of light. Photons can therefore no longer escape the gravitational pull of this object, and it becomes a black hole.

photons is IC scattering in the atmosphere (corona) of the accretion disk, which itself is not hot enough for X-ray emission (Marscher 2006).

The accretion disk is embedded in an axis-symmetric, opaque dust structure called the central torus. The torus dimensions are in the order a 0.1 to 10 parsec. Its opening axis is referred to as the ionization cone. The dust in the torus is in the atomic or molecular phase, leading to the emission of ultraviolet, optical, and near-infrared light.

These basic building blocks are common in all AGN. However, about 10% of all discovered AGN exhibit relativistic outflows leaving the ionization cone along the axis of the black hole. This jet of particles is assumed to be formed by strong magnetic fields acting upon the accretion disk in immediate vicinity of the black hole. As it only shows up in a fraction of AGN, its formation might be linked to the mass of the central black hole or the spin of the accretion disk. The jet then protrudes all constituents of the AGN and reaches extension up to kilo- and megaparsec (Catanese and Weekes 1999). The plasma carried outwards at relativistic velocities by the jet produces EM radiation which is highly collimated. The power and photon frequencies measured on Earth are therefore dependent on the angle between the jet and the line-of-sight to Earth, in agreement with the unified theory of AGN. Different parts of the relativistic jet can be observed in all three exposures in Figure 2.3, suggesting that the jet is inhomogeneous. Observations like these serve to identify the building blocks of AGN when combined with models of the emission zones.

Figure 2.4 summarizes the basic structure and emissions of AGN, including the formation of a jet. The black hole, accretion disk, and torus are depicted on the left, including a hot corona which serves as a source of hot electrons in many leptonic models (Marscher 2006). Magnetic fields which are possibly induced by the accretion disk lead to emission of the two-sided jet. The jet is inhomogeneous, leading to shock fronts as fast-moving parts collide with slower-moving parts. These shock fronts offer photon acceleration sites and can appear to be moving at superluminal speeds from the point of view on Earth, due to the relativistic movement of the emission zones. Also shown are dense clouds towards the central region of the AGN, called *broad line regions* as the temporal dependence of the spectral line features of AGN is attributed to them, and the *narrow line regions*, which contain low-density clouds further out the AGN (Netzer 2015). Note the logarithmic scale in units of the Schwarzschild radius.

If the AGN disk is viewed edge-on, the detected emission is thermal radiation and the AGN is classified as disk dominated AGN. The observed behaviour of the sources gets more extreme and, subjectively, more interesting when the observer is granted a view into the eye of the storm: Down the rotation axis of the accretion disk, into the core region of the AGN. Objects where the relativistic jet points directly at Earth are called *blazars.*

2.4 BLAZARS

Blazars are AGN whose relativistic jet is closely aligned with the line-of-sight to Earth (Urry and Padovani 1995). The EM radiation of these collimated outflows is observed as highly variable emission from radio- to γ-ray frequencies. As the bulk motion of the
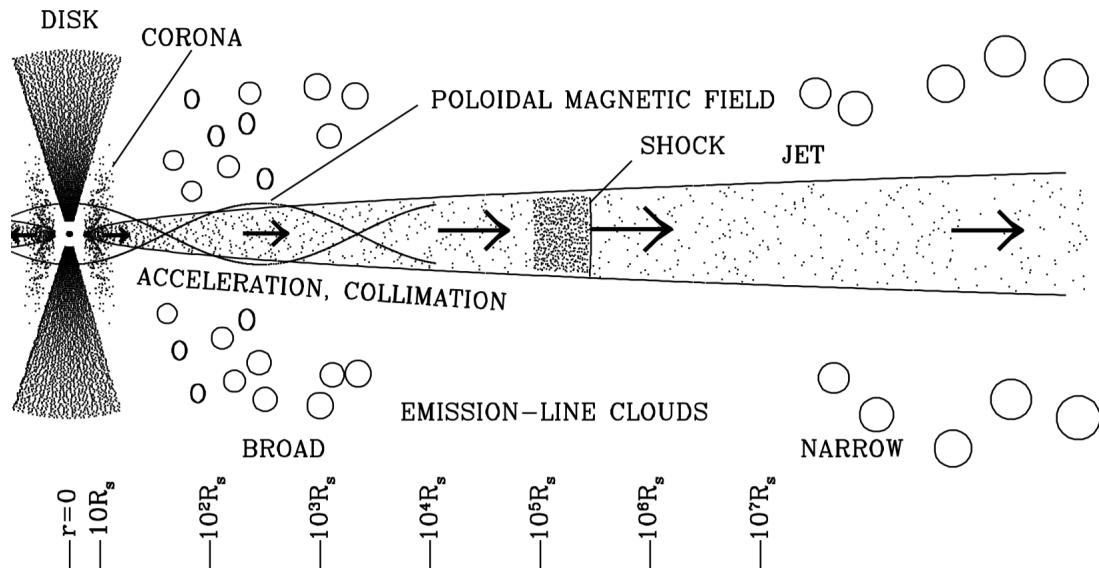
Figure 2.4 *Structure of Active Galactic Nuclei* The basic components of active galactic nuclei are the black hole, the accretion disk, and the large dust torus, shown here towards the left of the sketch. In about 10% of AGN, jets are observed. The relativistic jet is two-sided, only one side is shown. Adapted from Marscher (2005).

plasma is close to the speed of light and directed towards Earth, the emitted radiation is Doppler beamed, increasing the apparent brightness of the jet.

Figure 2.5 shows an observation of PKS 2155-304 by the H.E.S.S. experiment from July 28, 2006 (Aharonian et al. 2007a). The VHE γ-ray emission of this blazar more than doubled in the time-span of 20 minutes, before it decreased by a factor of seven in the following hour. The variability of blazars is thought to arise near the central region and in the relativistic jet. In close vicinity of the black hole, high-energy synchrotron emission can be observed in X-ray. The continuum emission covering the whole electromagnetic spectrum is then generated as the electron density and magnetic field strengths inside the jet decrease with increasing distance to the black hole. The wavelength of the emitted radiation then increases towards the outer regions. Indeed, Figure 2.3 shows that different regions of the jet are responsible for different emission features.

Relativistic jets are not unique to AGN. They often are observed when mass is accreted by a compact object, such as a black hole or a neutron star. The interplay between the accretion disk and the black hole in the formation and acceleration process of the relativistic jet is still an open question (Romero et al. 2017). The same holds for the leptonic or hadronic origin of γ-rays and the location of the emission zone along the jets. Variability observations are seen as keys to the answers. The characteristic time-scale of variability in a light curve puts an upper limit on the size of the emission region due to the causality principle. If the light curves exhibit variability on time-scales of Δt, the emission region has to be confined to a sphere with radius $R \leq c\Delta t D$, where D is the Doppler factor of the relativistic plasma emitting the radiation (Ulrich et al. 1997). The fast variability in the order of minutes therefore indicates that the γ-ray emission site is close to the central region of the AGN or within a localized inhomogeneity in the jet. If the radiation is emitted close to the black hole, it's characteristic time-scale could
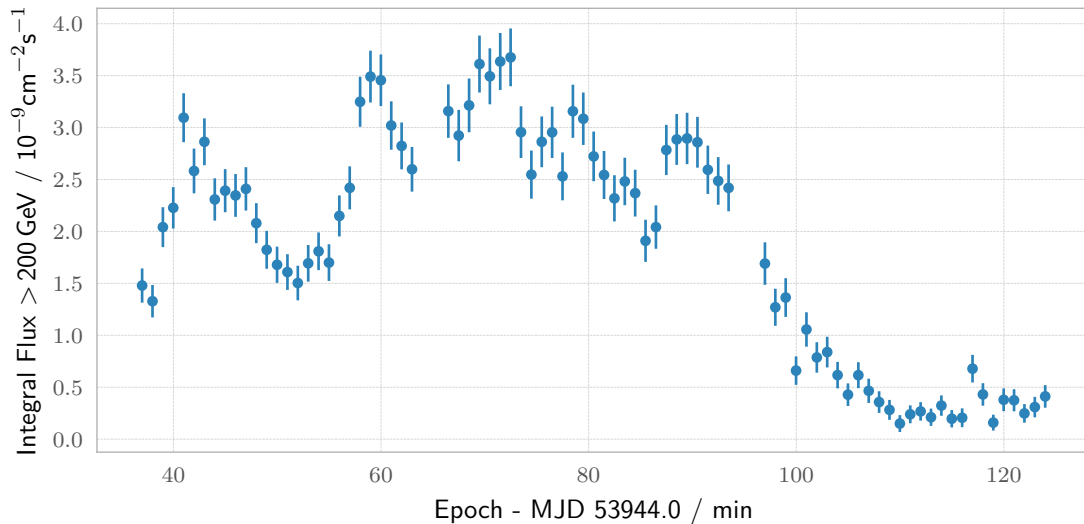
Figure 2.5 *Erratic Variability of Blazars* The highly variable VHE γ-ray emission from the blazar PKS 2155-304 as observed by the H.E.S.S. experiment on July 28, 2006. The data can be found at `https://www.mpi-hd.mpg.de/hfm/HESS/pages/publications/auxiliary/ApJL664_L71.html`. After Aharonian et al. (2007a).

reflect the Schwarzschild radius, which would yield the black hole properties. Therefore, the VHE γ-ray window is essential to studying and disentangling the complex core regions of blazars and the creation of astrophysical jets.

2.4.1 *Periodicity in Blazars*

Periodic modulations of the TeV γ-ray emission in blazars have been derived from a number of models of the core regions of blazars. Their observation and the period of the oscillation would put large constrains on the possible intrinsic source processes. In TeV γ-rays, claimed observations of periodic and quasi-periodic oscillations in blazars are rare. The repeating patterns in light-curves are difficult to unambiguously identify because of the nature of sources. Blazars are complex sources with numerous intrinsic processes occurring simultaneously, with a wide range of characteristic time- and energy scales. Single-band snapshots of their emission are therefore inadequate to disentangle of the complexity and gain insights. Long-term multi-wavelength observations are required to get a complete picture.

Therefore, statistically significant periodicity is usually not found in single-band analysis, but in multi-wavelength campaigns, e.g. in Ackermann et al. (2015), where γ-ray measurements from the *Fermi*-LAT were combined with data from optical- and radio-waveband long-term monitoring processes to reveal a possible quasi-periodic oscillation in PG 1553+113 on a time-scale of 2 years. In the following, a non-exhaustive list of models is given which have been proposed as mechanism for a periodic variability in the VHE flux of AGN, based on either the processes feeding the relativistic outflow or on a helical motion of the jet. Many models require a binary black hole systems (BBHS) at the core of the AGN. Theoretical models of hierarchical galaxy evolution

as well as observational evidence support the claim of BBHS (Begelman et al. 1980; Komossa 2003).

ACCRETION FLOW INSTABILITIES   Shock waves propagating through the accretion disk may lead to periodic modulations of the energy outflow. The expected periods are in the order of $\sim 10^5$s $M_{\mathrm{BH}}/M_\odot$. Assuming a black hole mass of $M_{BH} = 10^9 M_\odot$, these shock waves could yield periodicity on time-scales of weeks (Honma et al. 1992; Ackermann et al. 2015). BBHS could also lead to periodic variation of the accretion flow due to the Keplerian orbital motion of the black hole system. The expected time-scales are in the order of 1 to 25 years (Ackermann et al. 2015).

HELICAL JET MOTION   Due to Doppler beaming of the radiative outflow, any mechanism that periodically changes the line-of-sight between Earth and the jet would cause periodic modulations of the γ-ray emission. Again, BBHS could lead to helical motion of the jet due to the orbital motion of the companions leading to the periodic modulation of the azimuthal velocity of the jet with the angular frequency

$$\Omega = \sqrt{G(M+m)/d^3}, \tag{2.6}$$

where M and m are the black hole masses, d their separation, and G the gravitational constant. Furthermore, perturbations in the accretion disk may lead to jet precession. These perturbations may also be induced by the tidal forces of a BBHS (Rieger 2004; Ackermann et al. 2015).

Again, the (periodic) variability of blazars observed in TeV γ-rays is linked to the central regions of the sources.

2.4.2 *The Markarians*

In this work, the light curves of the two blazars closest to Earth are examined, Markarian (Mrk) 421 and Mrk 501.[6]

MARKARIAN 421   The blazar Mrk 421 was the first extragalactic source discovered in VHE γ-rays (Punch et al. 1992) and has been subject of frequent observation campaigns in the TeV regime ever since (e.g. Acciari et al. 2014; Ahnen et al. 2016; Coutiño de León et al. 2017). At a redshift of $z = 0.031$, it is the closest blazar to Earth (Ulrich et al. 1975). Its flux exhibits large variability with reported flux-doubling times of 15 minutes (McEnery et al. 1997). Correlation studies between X-ray and γ-ray emissions found that the bands are correlated within time differences below 1.5 days, supporting a leptonic origin of the VHE emission, as X-ray and γ-rays are generated by the same electron population (Horan et al. 2009). However, orphan flares in the TeV regime have been observed as well (Sahu et al. 2016). Figure 2.6 depicts the SED of Mrk 421 as measured by multiple experiments ranging from radio to VHE γ-rays during a multi-wavelength campaign between January and June 2009 (Abdo et al. 2011b). Observable are the two bumps in the spectra, with peaks in the X-ray and γ-ray regimes. The VHE

---

6 Even though the catalogue of the Markarian galaxies consist of more than 1 000 sources, in this work, *the Markarians* generally refers to Mrk 421 and Mrk 501.
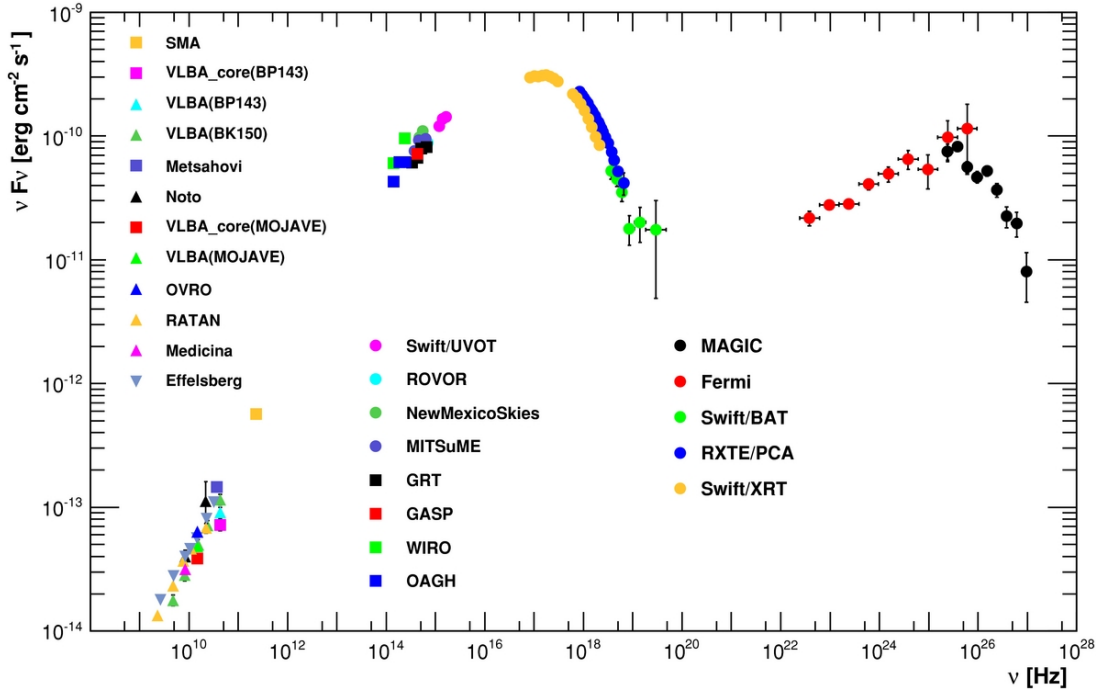
Figure 2.6 *The Spectral Energy Distribution of Mrk 421* The SED of Mrk 421 as measured during a multi-wavelength campaign of multiple experiments between January 19, 2009, and June 1, 2009. Measurements were taken in the range of radio- to VHE γ-ray wavelengths. The two bumps in the SED are characteristic for active galactic nuclei and many other classes of astrophysical sources. The low-energy peak is attributed to synchrotron emission from relativistic electrons in ambient magnetic fields. The high-energy peak in blazars is well described by inverse-Compton scattering of photons to high energies. Figure from Abdo et al. (2011b).

energy emission in blazars is usually well described by the leptonic model (Catanese and Weekes 1999; Abdo et al. 2010).

MARKARIAN 501   Mrk 501 is the second closest blazar to Earth with a redshift of $z = 0.034$. As such, it was the second blazar to be detected in TeV γ-rays (Quinn et al. 1996). It has similar properties as Mrk 421. Albert et al. (2007) observed doubling of the TeV γ-ray flux of Mrk 501 within two minutes on two occasions in June and July 2005. Kranich (2001) claimed periodicity both in TeV regime with HEGRA and in X-ray with data from the RXTE satellite, with a periodic modulation every 23 days. The examined light curve was measured in 1997 and spanned 115 days. Nishikawa and The Utah Seven Telescope Array collaboration (1999) reproduced the same results using the same epoch and data from RXTE but TeV data from the Utah Seven Telescope Array group. Rieger and Mannheim (2003) linked the 23-day period to a possible binary black hole in Mrk 501.

MONITORING THE NON-THERMAL UNIVERSE

Following the discovery of *cosmic rays* (CRs) by Hess (1912) and the first measurement of extended air showers induced by the interaction of these particles with the atmosphere by Auger et al. (1939), another 50 years passed until the Whipple collaboration published the first unambiguous detection of a VHE γ-ray source (Weekes et al. 1989). It was not for a lack of determination, as the scientific value of γ-rays is apparent. While charged CRs are subject to deflection by intra- and extra-galactic magnetic fields, obscuring their point of origin, γ-rays are unaffected and can be traced back to the source. However, the detection of γ-rays poses a technical challenge which took decades to approach effectively and is still not completely overcome.

The VHE γ-ray ratio to CRs is nowadays believed to be about 1×10^{-4} for particles reaching Earth from the galactic plane and 1×10^{-5} for particles with extragalactic origin (de Naurois and Mazin 2015). Their flux is of the order of 1 photon per square meter per year. In addition, γ-rays are absorbed by Earth's atmosphere. Direct detection of these cosmic messengers is therefore not feasible, as it would take a satellite years to reliably detect a source in the VHE regime. Indirect detection via the extended air showers using the Earth's atmosphere as detector solves this problem by giving the telescopes a large collection area, but gives rise to new challenges. The Cherenkov light flash emitted by the air shower[1] lasts for only nano-seconds and is hidden in a see of night-sky background photons. Furthermore, the fraction of γ-ray induced air showers to hadronic air showers is representative of the ratio of γ-rays to CRs. A reliable separation between electromagnetic and hadron showers is required. The key technique to solve both problems was pointed out by Hillas (1985), who outlined a method to differentiate the Cherenkov light flashes induced by electromagnetic and hadronic showers using images of the showers. The technical requirements are sophisticated cameras, able to capture resolved images of the Cherenkov light flashes.

In the almost 30 years following the first detection of the Crab Nebula in VHE γ-rays by the Whipple observatory, technological advancement and dedicated efforts have given rise to a multitude of *Imaging Air Cherenkov Telescopes* (IACTs), each generation larger and more sensitive than the previous, while the technological and physical challenges remain the same. This chapter focuses on a pioneering effort in Cherenkov astronomy, the First G-APD Cherenkov Telescope. The telescope set-up and operation are outlined, followed by an overview of source monitoring efforts in the VHE regime and a short overview of other γ-ray observatories.

---

1 A more detailed look at the development of electromagnetic air showers is following in Chapter 4.

Figure 3.1 *The First G-APD Cherenkov Telescope* FACT is located at the Observatorio del Roque de los Muchachos on the Canary Island of La Palma. The mirror dish has a diameter of 3.8 meters. The camera made of silicon photomultipliers is located in the white cylinder in the top right corner and has a field-of-view of 4.5°. Photo credit: Anderhub et al. (2013)

3.1   THE FIRST G-APD CHERENKOV TELESCOPE

3.1.1   *The Telescope Set-up*

The *First G-APD Cherenkov Telescope* (FACT) is an IACT located on the Canary Island of La Palma, Spain, at the Observatorio del Roque de los Muchachos, 2200 meters above sea level. It is designed to observe VHE γ-rays by measuring Cherenkov light, light emitted by charged particles travelling at superluminal velocities through the Earth's atmosphere. These particles are products of particle showers induced in the atmosphere by high-energy particles.

The telescope's dish has a diameter of 3.8 meters and consists of 30 hexagonal mirrors, see Figure 3.1. These mirrors reflect the incoming Cherenkov light into the telescope's camera. Here, 1 440 pixels with a field-of-view (FoV) of 0.11° each detect the photons and are read out individually. Overall, the camera has a FoV of 4.5°. FACT was built on the mount of the former HEGRA CT3 telescope.

The camera of FACT is unique in the world of IACTs for the reason that it uses *silicon photomultipliers* (SiPMs) to detect the incoming photons. These SiPMS are made up of arrays of *Geiger-mode avalanche photo-diodes* (G-APDs), which is where FACT gets its name from (Anderhub et al. 2013; Biland et al. 2014). FACT is a pathfinder telescope to explore the long-term operation of SiPMs in Cherenkov astronomy. SiPMs have several advantages over the commonly used photomultiplier tubes found in the cameras of other IACTs. They offer a higher photon-detection efficiency and operate under lower bias voltages. An important characteristic is also their robustness: SiPMs

allow for observations during bright nights, including during full Moon,[2] which reduces the amount of gaps in the observation schedule and increases the telescope's up-time. FACT continuously investigates the effect of changing temperature and photon flux on these sensors. Almost six years after FACT's First Light in October 2011, no effects ageing have been observed (Biland et al. 2016).

FACT is operated remotely and to a large degree robotically. The observer operates the telescope and receives system status updates through an online interface.[3] Automatic observation schedules are generated based on the sources position and predicted visibility.

Besides the proof-of-principle for the use of G-APDs in Cherenkov astronomy, the mission statement of FACT is the long-term monitoring of only a handful of sources, to study the temporal evolution and variability of AGN. As of September 2017, 91% of the total observation time of 9238 h were targeted at five sources only: Mrk 501, Mrk 421, the Crab Nebula, 1ES 2344+514, and 1ES 1959+650.[4] This dedication to continuous monitoring is rare in the community of IACTs, which mainly pursues other science goals like the survey of TeV sources, the constraint of dark matter theories and theories on the evolution of the Universe, and the follow-up on neutrino and gravitational wave events.[5] These goals require a larger sample of sources than can be conciliated with long-term monitoring.

3.1.2 *The Night Sky over FACT*

FACT aims to study the VHE γ-ray emission from blazars. These sources are introduced in Chapter 2, and will now be set in context to FACT by looking at the telescope's FoV. Studying the relation between FACT's local coordinate system and the coordinates of the extragalactic sources reveals observational effects and constraints which later leave their imprints in the collected data and have to be accounted for.

Figure 3.2 shows the sky in equatorial coordinates using the equal-area Mollweide projection. The coordinates of the seven sources that FACT observers most are shown, in addition to the coordinates of the blazar PKS 2155-304. The black line represents the FoV of the FACT telescope on the night of its First Light, October 11, 2011, at 5 am. Sources inside the FoV of the telescope can be observed at this moment, sources on the outside are hidden behind the Earth. The sources inside the FoV are marked with orange circles, the sources outside with blue crosses. As the Earth turns, the FoV moves towards larger right ascension, moving sources into and out of the FoV.

Sources with declinations larger than 62° are always visible[6] from FACT's point of view at a latitude of 28°45'41.9" N, while objects with declinations smaller than -62° never cross FACT's FoV (Karttunen et al. 2007).

The dashed, black line marks the declination which corresponds to the zenith above FACT. Objects close to this line will culminate at large altitudes, i.e. small zenith angles. This is advantageous for observations of γ-ray showers as there is less atmo-

---

2 γ-ray showers can even be observed while the full Moon is in the FoV, see Knoetig et al. (2013).

3 https://www.fact-project.org/smartfact/

4 https://www.fact-project.org/dch/obs_time.php

5 FACT follows up on exceptional events as well, however, the neighbouring MAGIC telescope with its higher sensitivity is better suited for this task.

6 The source is *circumpolar*, meaning that it never sets below the horizon at this latitude.
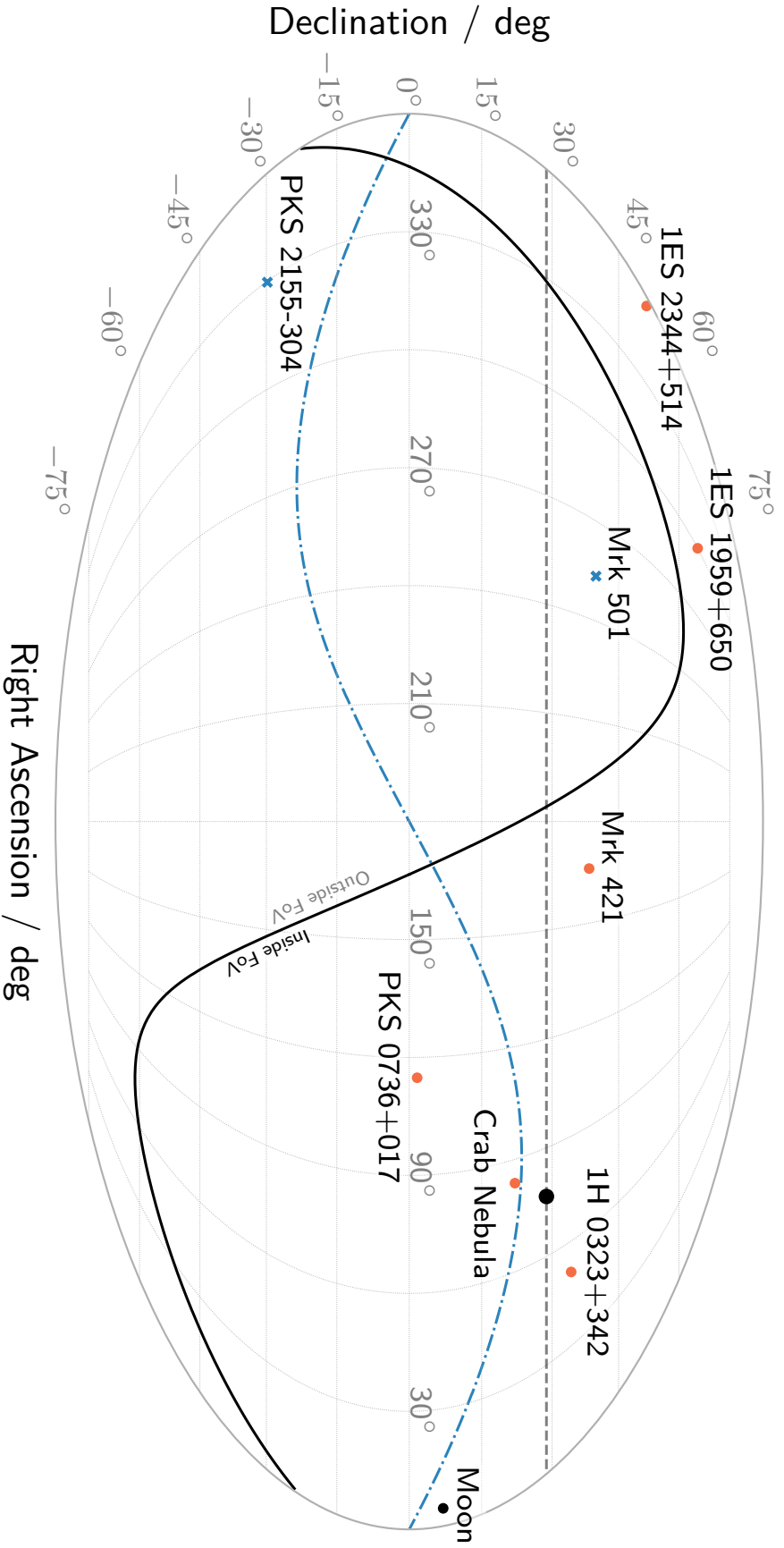
Figure 3.2 *The Night Sky over FACT* Shown is the sky in equatorial coordinates using the equal-area Mollweide projection, with the FACT field-of-view (FoV) represented by the solid black line. The locations of eight TeV sources are indicated by either orange dots, if the source is in the FoV, or by blue crosses, if the source is outside the FoV. The dash-dotted, blue line represents the ecliptic. The position of the Moon is marked by the black circle. It stays within 5° distance to the ecliptic and affect the observations of sources close to the ecliptic, like the Crab Nebula. The dashed, black line indicates the movement of the source over FACT, shown as large dot on this line. Sources close to the line in declination will have their upper culminations at low zenith angles, which is advantageous for the measurement of γ-ray induced air showers. Shown here is the FoV of FACT on the night of its First Light October 11, 2011, at 5am.

sphere between the telescope and the shower maximum to absorb the Cherenkov light. It immediately becomes apparent in Figure 3.2 that FACT is in a good location to study the two brightest blazars in the night sky: Mrk 501 and Mrk 421. γ-ray rates measured from these sources at upper culmination will hardly be affected by absorption in the Earth's atmosphere, assuming no clouds are in the line of sight. On the other hand, the observed rates from sources towards the celestial poles like 1ES 1959+650 and PKS 2155-304 will always be significantly diminished, even under perfect atmospheric conditions. PKS 2155-304 is therefore rarely observed by FACT, although it exhibits strong variability on short time scales, as mentioned in Chapter 2. A detailed study on the dependency of the γ-ray rate on the zenith angle of the source is following in Chapter 4. The black point on the the dashed, black line marks the current position of the zenith above FACT.

Shown as dash-dotted, blue line in Figure 3.2 is the ecliptic plane. The objects of the Solar System revolve around the Sun in this plane. Most significantly for FACT and telescopes in general, the Moon's orbital plane is inclined with respect to the ecliptic by only 5°. The Moon's position is marked in Figure 3.2 by a black circle. Sources close to the ecliptic are therefore frequently close in angular distance or behind the Moon, rendering their observations impossible. Observations of the Crab Nebula at a declination of 22° are most affected by the lunar sidereal period.[7] When the Moon is not in the FoV, the Crab Nebula is a prime target for observation and calibration of the telescope due to its upper culmination within 7° zenith angle.

Earth's rotation causes the FoV to shift towards larger right ascension with time. After one sidereal day, it has shifted by 360° and the same stars are visible as before. However, as the sidereal day is 4 minutes shorter than the solar day, the FoV will move approximately 1° towards larger right ascension each night. Therefore, as the Earth revolves around the Sun, different sources move into and out of the FoV over the year. The sky in summer looks different than the sky in winter. Figure 3.2 can be used to estimate these breaks in observation for the different sources. The Crab Nebula at a declination of 22° will be blocked by the Sun for about 40% of the year, roughly the time it takes for the FoV to travel by 150° in right ascension. Mrk 501 and Mrk 421 are close to each other in declination, they are not visible to FACT for about a third of the year. However, the uniform spread of the sources in right ascension ensures that FACT has a target of observation for all nights. After one sidereal year,[8] the FoV has moved back to its original position.

3.2 LONG-TERM MONITORING OF TEV SOURCES

The targets of FACT's observational efforts, the blazars, are highly variable on a variety of time-scales (e.g. H.E.S.S. Collaboration 2016). Continuous observations of these sources is a requirement to gain insights into their core regions, the massive black holes and its interaction with the jets. For example, the evolution of the spectral

---

7 The sidereal month is the time that it takes the Moon to revolve once around Earth, which is 27.3 days.

8 A sidereal year is the orbital period of the Earth around the Sun with respect to the fixed background stars. With 365.25 days, it takes about 20 minutes longer than the more commonly known tropical year.

energy distribution over time can constrain model parameters of the emission processes occurring in the sources.

In the regime of TeV energies, FACT is joined by the *High Altitude Water Cherenkov* (HAWC) observatory in its monitoring efforts (Mostafa 2013). Since March 2015, HAWC has been observing the TeV γ-ray sky, located at 4 100 m above sea level in the state of Puebla, Mexico. Instead of the air Cherenkov technique applied by FACT, HAWC is relying on the water Cherenkov technique, collecting the Cherenkov light of relativistic particles as they pass through one of 300 tanks of water. As this method does not require good atmospheric conditions and a dark background sky, HAWC can observe two thirds of the sky within 24 h and reaches a duty cycle of 95%. Not visible are the regions outside $-64°$ to $64°$ declination. First monitoring results using the data acquired over the past 1.5 years can be found in Lauer (2016). Due to its shift in longitude relative to FACT by $\sim 79°$ W, HAWC can observe sources for about 5.3 h after they have moved out of FACT's FoV, increasing the coverage of one source by both telescopes up to about 12 h.[9] This is a useful extension of the observation windows, and though the different energy sensitivities and resolutions make comparison of the measured γ-ray rates challenging, first joint results have been published in Dorner and Lauer (2017). In general, good agreement between the observed nightly fluxes of Mrk 501 and Mrk 421 are found between the two instruments. Large discrepancies can be associated to periods of high short-term variability in the sources.

Additional support for FACT and HAWC in their long-term monitoring efforts is planned: The *Monitoring At TeV Energies* (M@TE) telescope, to be built in San Pedro Matír, Mexico, is a duplicate of the FACT telescope with improved camera hardware. Two more telescope mounts of the former HEGRA experiment are available. More details are given in Chapter 6 and in Alfaro et al. (2017).

3.3 OBSERVING THE (VERY) HIGH-ENERGY γ-RAY SKY

This section gives a brief overview of four γ-ray observatories which, like FACT, regularly observe blazars and are referenced in this thesis.

WHIPPLE OBSERVATORY   The Whipple 10 m γ-ray telescope at the Fred-Lawrence-Whipple-Observatory in Southern Arizona, USA, was in operation from 1968 to 2013. It was the pioneer telescope in VHE γ-rays, with the first detection of a TeV γ-ray source (Crab Nebula, Weekes et al. (1989)) and a γ-ray blazar (Mrk 421, Punch et al. (1992)). Whipple detected γ-rays between 300 GeV to 10 TeV. The primary science goal was to detect sources in the VHE regime, which later switched towards monitoring effort in the early 2000's. The 14-year light curve of Mrk 421 recorded by Whipple from 1995 to 2009 is shown in Figure 3.3.

FERMI LAT   The Large Area Telescope (LAT) is a satellite-borne γ-ray observatory aboard the Fermi Gamma-ray Space Telescope. It is a pair conversion telescope susceptible to photons in the high-energy regime, from 20 MeV to around 300 GeV. Launched

---

9 Due to the influence of atmospheric disturbances when observing sources at large zenith angles, the maximum observation time of a source from one single site is about 6 h, assuming it culminates in the zenith.

in 2008, its orbit around Earth takes 96 minutes and, combined with the field-of-view of 2.4 steradians, allows for a complete survey of the sky within two orbits (Atwood et al. 2009). This ability to rapidly observe distinct sources make the Fermi LAT a frequent participator in multi-wavelength observations, where a source is simultaneously observed in different wavelength regimes (e.g. Ahnen et al. 2017). Correlations between the observed variability in different wavebands help constrain the emission regions as well as model parameters of the spectral energy distributions, as they support the leptonic model of photon production.

H.E.S.S.   The High Energy Stereoscopic System (H.E.S.S.) is operated in the Khomas Highland in Namibia since 2004. It is a system of five telescopes, allowing for an increased angular resolution of the origin of the γ-rays and an increased sensitivity due to the increased collection area. Measurements are taken of γ-rays with energies between 30 GeV and 100 TeV (Hofmann 2000). The H.E.S.S. collaboration was the first to observe periodic modulation of VHE γ-ray emission from an X-Ray binary system (LS 5039, Aharonian et al. 2006) and VHE γ-ray emission from a stellar cluster containing massive stars close to the end of their life cycle, so called Wolf-Rayet stars (HESS J1023-575, Aharonian et al. 2007b).

MAGIC   The Major Atmospheric Gamma-Ray Imaging Cherenkov (MAGIC) telescope system consists of two IACTs located on La Palma, Canary Islands, next to the FACT telescope. The energy range spans from 60 GeV to about 20 TeV, at a resolution of about 1% Crab units (Tridon et al. 2010). In 2008, MAGIC was the first to observe pulsed γ-ray emission a neutron star, the Crab Pulsar, with energies above 25 GeV (Aliu et al. 2008), as mentioned in Chapter 2.
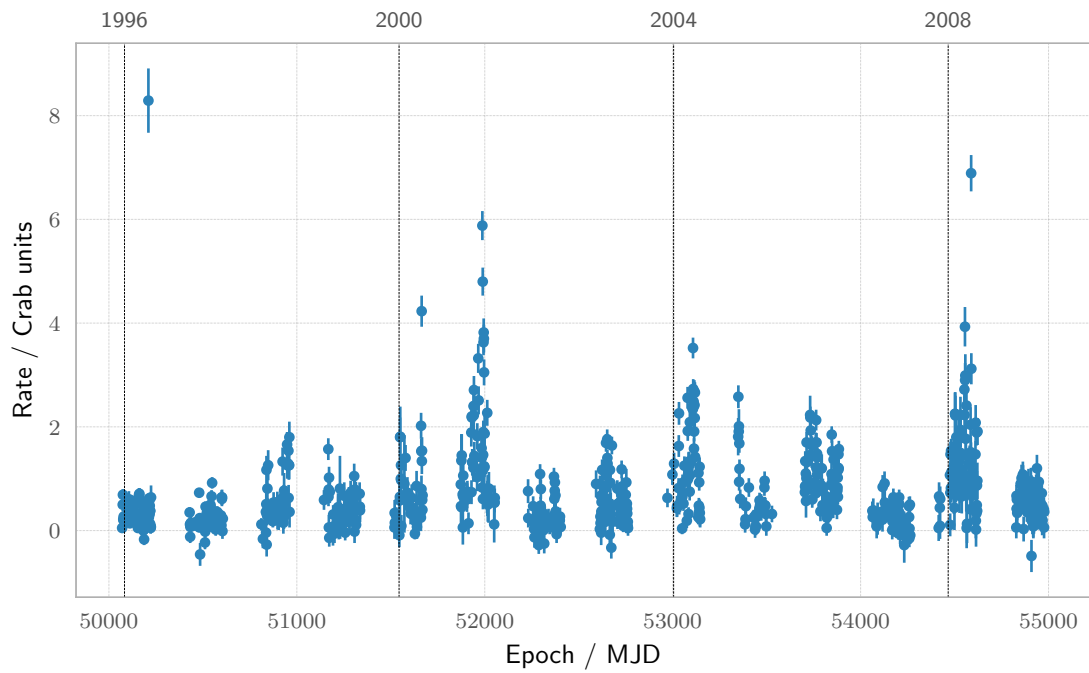
Figure 3.3 *14-year light curve of Mrk 421 recorded by the Whipple Observatory* The TeV γ-ray flux in Crab Units of Mrk 421 as recorded by the Whipple observatory between December 1995 and June 2009. Quiescent and active states are visible, including large flares around 2001 and 2008. Data from https://veritas.sao.arizona.edu/veritas-science/veritas-results-mainmenu-72/371-mrk421-14yrs.

DATA PIPELINE

The atmosphere is opaque to HE and VHE γ-rays. While in the HE regime, satellites can be deployed to overcome this obstacle, the rate of VHE γ-rays is too small to allow for statistically significant detection of sources in a certain timeframe. Instead, the atmosphere is used as detector volume, by detecting the products of the interaction between γ-rays and the atmosphere. Thereby, the γ-rays are detected indirectly.

The indirect detection by means of the Cherenkov radiation requires models of the interaction between the photon and the atmosphere and the resulting EM cascade. Furthermore, the principle parameters like energy and arrival direction of the TeV γ-ray need to be extracted from the Cherenkov light cone, while rejecting a large number of hadronic background showers with a ratio of about 10 000:1 compared to EM showers.

This chapter describes the processing of the raw data acquired by the FACT telescope and its conversion into the finished data products. The discussion is started with a toy-model description of the EM cascades induced be γ-rays and CR electrons in the atmosphere. The detection of the produced Cherenkov light by IACTs is covered. A heuristic model of the zenith angle dependence of the raw data both for EM and hadronic showers is derived and applied to the CR and γ-ray rates. The threshold dependence and the application of correction factors finally lead to the nightly γ-ray rates used in the analysis in Chapter 5.

4.1 DEVELOPMENT OF ELECTROMAGNETIC CASCADES

EM cascades are initiated by electrons or photons entering the atmosphere and interacting with the ambient particles. The interaction processes are bremsstrahlung, ionization or excitation for electrons and pair production, Compton scattering, and absorption for photons. For primary particles in the VHE regime, the cascades are dominated by bremsstrahlung and pair production processes until the EM shower particles have reached the critical energy E_C where the contribution of the remaining processes to the energy loss is equal to the contribution of bremsstrahlung and pair production. For electrons in air, $E_C \approx 86\,\text{MeV}$.

The energy losses over the atmospheric depth X ([X]: g cm^{-2}) can be described by

$$-\frac{\mathrm{d}E}{\mathrm{d}X} \approx \alpha(E) + \frac{E}{X_e}, \tag{4.1}$$

where α describes the loss due to ionization or excitation and X_e is the radiation length after which the energy E_0 of the primary particles is reduced by a factor of $1/e$. For electrons in air, $X_e \approx 28.9\text{g/cm}^2$, while for photons, QED calculations yield $X_p = 7/9 X_e$ (Firpo 2006; Spurio 2014).

Overall, the precise development of EM showers is a complex, stochastic processes due to the numerous interaction mechanisms, in part energy-dependent, and the atmo-

spheric conditions which depend on e.g. the height above ground and the temperature. Nevertheless, a few principle relations can be derived using a simple toy-model developed by Heitler (1954). In this model, the excitation and ionization energy losses of electrons are neglected, $\alpha = 0$, and the radiation lengths of photons and electrons is approximated as equal, $X_e = X_p$. Equation 4.1 then has the simple solution

$$E(X) = E_0 \exp(-\frac{X}{X_e}). \tag{4.2}$$

After a distance $d = \ln 2 X_e$, the particles have lost half of their energy, electrons via bremsstrahlung, photons via pair production, producing secondary electrons and photons which themselves initiate EM cascades. Both mechanism increase the number of particles in the EM shower by two. The Heitler model therefore describes the shower as a binary tree, where each step of a distance of $\ln 2 X_e$ increases the number of particles by a factor of two while halving the energy per particle. After n steps, the number of particles in the shower is 2^n, while the energy per particle is given by $E_0/2^n$.

The break condition for the shower is reached when the energy per particle is E_C and other interaction processes become dominating. At this point, the *shower maximum* after $n_{\max}$ steps, the number of particles in the shower is

$$N_{\max} = 2^{n_{\max}} \approx \frac{E_0}{E_C}, \tag{4.3}$$

and the shower has reached a depth of

$$X_{\max} = X_0 + X_e \ln \left(\frac{E_0}{E_C} \right), \tag{4.4}$$

where X_0 is the atmospheric depth of the first interaction between primary particle and atmosphere (Heitler 1954). For a primary energy of $1\,\mathrm{TeV}$, $N_{\max} \approx 1 \times 10^7$.

Extensive air showers (EAS) include EM and hadronic showers. Hadronic showers differ from EM showers due to their hadronic components, which initiate EM sub-showers as the neutral and charged pions decay. The large number of collision processes gives the hadronic shower a wider lateral distribution, which is used by IACTs to differentiate between hadronic and EM showers.

4.2   DETECTION PRINCIPLE OF IACTS

The charged constituents of EM cascades travelling through the atmosphere with velocities larger than the speed of light in air emit Cherenkov light. For a particle with a velocity v, the Cherenkov condition is thus given by

$$\beta = v/c \overset{!}{>} 1/n, \tag{4.5}$$

where c is the speed of light and n the refractive index of the atmosphere. The Cherenkov light is emitted in a cone with the opening angle θ_C,

$$\cos \theta_C = \frac{1}{\beta n}. \tag{4.6}$$

The number N_C of emitted Cherenkov photons is proportional to the energy E_0 of the primary particle. IACTs measure the shape and size of the Cherenkov light cone

in order to indirectly infer on the properties of the primary particle. The atmosphere serves as detector volume, converting the energy of γ-rays into UV Cherenkov photons among other forms of energies. The Cherenkov light is collected by the telescope's mirror dish and imaged onto the focal point, where a high-speed camera records the image of the shower. Using the offset of the shower image from the camera centre and a set of parameters introduced by Hillas (1985), energy and arrival direction of the primary particle are extracted from the image. Figure 4.1 illustrates an EM cascade detected by the FACT telescope and the image of the shower recorded in the camera.
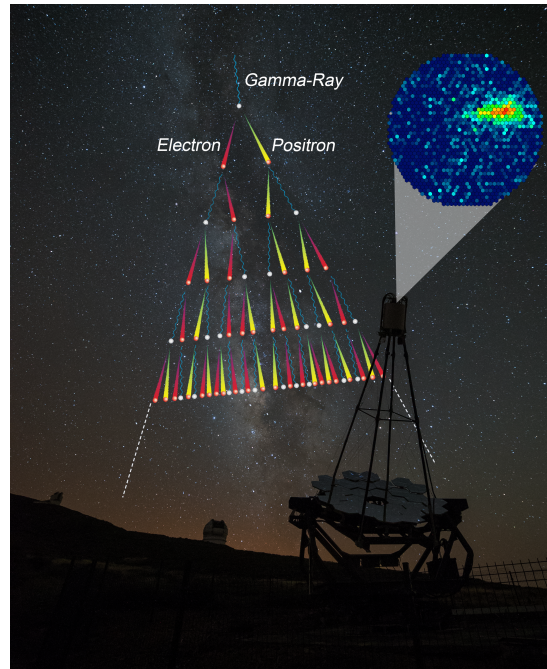

Figure 4.1 *Composite Image of EM Cascade recorded by FACT* The EM shower is initiated by a γ-ray and consists of pair production and bremsstrahlung processes. The displayed shower is modelled with the Heitler model. The Cherenkov light is focused by the mirrors onto the FACT camera in the focal plane of the dish. The inset shows an exemplary image of an EM shower. Credit: EM Cascade: `http://www.lanl.gov/discover/publications/1663/issues-archive/december2008.pdf`, FACT: Matthias Bergmann, Camera Inset: Bretz et al. (2013)

The Cherenkov light flashes last a few nanoseconds, therefore the integration time of the camera and the read-out electronics need to be of the same order. A further challenge is the large background of Cherenkov light induced by hadronic showers. Restrictive cuts on the shape parameter of the showers are required to ensure that only EM showers are counted towards the signal. After these selection cuts, EM showers initiated by electrons are the main source of background in the measurements. γ-ray and electron-induced EM showers cannot be differentiated using shower size parameters, therefore this background has to be quantified in a different manner. The FoV of IACTs is around 4.5° (Spurio 2014), much larger than the angular dimension of the observed sources. This allows for the simultaneous recording of on- and off-source measurements, i.e. signal and background, by pointing the centre of the FoV a few sub-degrees off of the source position. The background events are extracted from the

points in the sky that are symmetrically displaced with respect to the source position in the camera and the camera centre. This method is superior to taking single on- and off-measurements as the latter method decreases the data taking time by a factor of two. (Berge et al. 2007)

4.2.1 *Measurements with FACT*

For a single observation run of typically 5 minutes, the FACT telescope records the number N_{sig} of signal events coming from the source, as well as the number N_{bg} of background events from 5 off-source positions which are symmetrically displaced to the on-source position in FACT's camera layout. The number N_{exc} of excess events is then defined in analogy to Li and Ma (1983),

$$N_{\mathrm{exc}} = N_{\mathrm{sig}} - \alpha N_{\mathrm{bg}}, \tag{4.7}$$

where the factor $\alpha = 5$ accounts for the 5 simultaneous off-source measurements in comparison to the one on-source measurement. The measurement uncertainty on the excess events is then given by the Poisson standard deviation

$$\sigma^2(N_{\mathrm{exc}}) = \sigma^2(N_{\mathrm{sig}}) + \sigma^2(\alpha N_{\mathrm{bg}})$$
$$\implies \sigma(N_{\mathrm{exc}}) = \sqrt{N_{\mathrm{sig}} + \alpha^2 N_{\mathrm{bg}}} \tag{4.8}$$

The number of excess events from a source is measured over time, therefore the provided measurement quantities are the excess event rates

$$R_{\mathrm{exc}} = \frac{N_{\mathrm{exc}}}{T_{\mathrm{obs}}}$$
$$\sigma(R_{\mathrm{exc}}) = \frac{\sigma(N_{\mathrm{exc}})}{T_{\mathrm{obs}}} \tag{4.9}$$

Note that this quantity can be negative, if more background than signal events were detected, i.e. the source was not visible to the telescope.

4.3 OBSERVATIONS AT LARGE ZENITH ANGLE

The excess event rates measured by FACT are affected by numerous influences, e.g. by bad weather conditions such as clouds, by strong background light due to the Moon, or by the zenith angle of the source in the sky.

These influences lead to distorted measurements, altering the results of the observations. The goal of this following analysis is therefore to detect and quantify the influences of bad weather and the zenith angle of the source in the data, and to determine a correction factor to account for the changes in the excess event rates. A heuristic model of the zenith angle dependence of detected hadronic and EM showers is derived. Parts of this analysis have been published in Mahlke et al. (2017).

4.3.1 *Model of Zenith Angle Dependence*

In order to quantify the zenith angle dependence of the γ-ray rate, a simple model is constructed, using basic relations from the development of EAS in an isothermal atmosphere and the Heitler model. The differential rate of γ-rays detected by the telescope is given by

$$\frac{\mathrm{d}R(E)}{\mathrm{d}E} = \Phi(E) \cdot A_\gamma^{coll}(E), \tag{4.10}$$

where $\Phi(E)$ is the differential γ-ray flux of the source and $A_\gamma^{coll}(E)$ the energy-dependent effective collection area of the telescope. The latter includes the trigger efficiency, energy threshold, light pool area of the Cherenkov radiation, etc., and is usually retrieved by Monte Carlo simulations (Firpo 2006).

The light-pool area A is the base area of the Cherenkov light cone perpendicular to the telescope axis. It is assumed to only depend on the height h_{max} of the shower maximum. However, h_{max}, measured in meters from the height of the telescope above sea level, introduces both the zenith angle- as well as the energy dependence into the calculation of A: $h_{\mathrm{max}} = h_{\mathrm{max}}(E, \theta)$:

$$A(E, \theta) = \pi h_{\mathrm{max}}^2(E, \theta) \cdot \tan^2(\theta_C). \tag{4.11}$$

θ_C is the opening angle of the Cherenkov light cone, which depends on the refractive index of the atmosphere, and θ is the zenith angle. For an isothermal atmosphere, θ_C depends on the density only. It is assumed that the height h_{max} only varies slightly between the showers, therefore the density and θ_C can be regarded as constant. It is set to $\theta_C = 1.4°$. The height h_{max} is related to the atmospheric depth X_{max} of the shower maximum, measured in $\mathrm{g\,cm^{-2}}$, via the barometric formula

$$\frac{X_{\mathrm{max}}(E, \theta)}{X_0} = \exp\left(-\frac{h_{\mathrm{max}}(E, \theta)}{h_0} \right), \tag{4.12}$$

where h_0 is the scale height of the atmosphere and X_0 the atmospheric slant depth at vertical incidence of the shower (vertical column density of atmosphere). The scale height is constant, except for a geometrical dependence on the zenith angle θ:

$$h_0 = h_0(\theta) = \frac{kT}{mg} \cdot \frac{1}{\cos\theta}. \tag{4.13}$$

X_0 is used to set the height of primary interaction in terms of the atmospheric column density to $1035\,\mathrm{g\,cm^{-2}}$, its energy dependence is neglected.[1]

The atmospheric depth X_{max} of the shower maximum introduces the dependence of the primary particle's energy into the model. Following the energy splitting approximation for electromagnetic cascades as derived in Heitler (1954), it is given by

$$X_{\mathrm{max}} = \frac{\ln(E_0/E_C)}{\ln 2} \cdot X_e. \tag{4.14}$$

Here, E_0 is the energy of the primary particle, E_C is the critical electron energy where energy losses due ionization and bremsstrahlung are equal, and X_e is the radiation

---

1 Note that X_0 in Equation 4.4 is defined as the atmospheric depth that the incident particle has passed through at the point of first interaction, while in this model, X_0 is the atmospheric depth between the point of the first interaction and the ground at vertical incidence.

length of electrons in air. $E_C \approx 86\,\text{MeV}$ and $X_e \approx 28.9\,\text{g/cm}^2$. As hadronic showers are dominated by their electromagnetic components, it is assumed that Equation 4.14 is valid in first approximation for cosmic ray showers.

The dependence of the slant depth $X(\theta)$ on the zenith angle is given a free parameter in this model. While the first-order geometrical dependence is accounted for with a $1/\cos\theta$-term, $X(\theta)$ also contains higher-order corrections (e.g. due to the curvature of Earth). It was found that adding another free fit parameter a

$$X(\theta) = \frac{X_0}{cos^a\theta} \tag{4.15}$$

results in a good description of the data.

The scaling of the slant depth is therefore a function of the zenith angle. The energy threshold of the telescope is known to be zenith angle dependent: The farther the shower maximum is away from the telescope, the lower the photon density is on the ground: $E_{thresh} \propto 1/\cos^2\theta$. The dependence of the energy threshold is combined with the dependence of the slant depth $X(\theta)$ on the zenith angle, in the form of

$$E_{thresh} \propto \left(\frac{X(\theta)}{X_0}\right)^b \cdot \exp\left(c \cdot \frac{X(\theta)}{X_0}\right), \tag{4.16}$$

following Firpo (2006). A free parameter b is introduced as it allows for a better fit of the data. The second, exponential term in the equation is introduced to account for an increase of the energy threshold due to increased attenuation of the Cherenkov light by the atmosphere. b and c are the second and third free fit parameters of the model. The final fit function is then given by

$$R(\theta) = \int_{E_{thresh}(\theta)}^{\infty} \Phi(E) \cdot A(E,\theta)\mathrm{d}E = \int_{E_{thresh}(\theta)}^{\infty} \Phi(E) \cdot \pi h_{\max}^2(E,\theta) \cdot \tan^2(\theta_C)\mathrm{d}E. \tag{4.17}$$

Equation 4.17 allows for a good fit of the measured rates for both CR and excess γ-rays with the free parameters a, b, and c.

4.3.2 *Application to Rate of Cosmic Rays*

The derived zenith angle dependence in Equation 4.17 is now applied to the rate of CR measured by FACT. Assuming the CR flux is homogeneous from all directions on Earth, correcting for the zenith angle dependence in the measured CR rates can help identify observation runs where the γ-ray rate was decreased due to bad weather, which lead to the attenuation of the Cherenkov light and therefore a decrease in the observed rate. The CR rate is acquired from the background measurements by setting an artificial software trigger threshold, allowing for the recovery of hadronic showers above a certain energy from the background data.

Figure 4.2 shows the rate of CR in Hz detected by FACT as function of the zenith angle of the pointing direction of the telescope for single observation runs in the FACT database. The colormap was normalized for bins of 4°-width in order to represent the accumulation of runs near certain rates in dependence of the zenith angle. It can be seen that the rate is around 3 Hz for small zenith angles, and drops off for larger angles. In addition, the effect of bad weather during observations is visible, decreasing
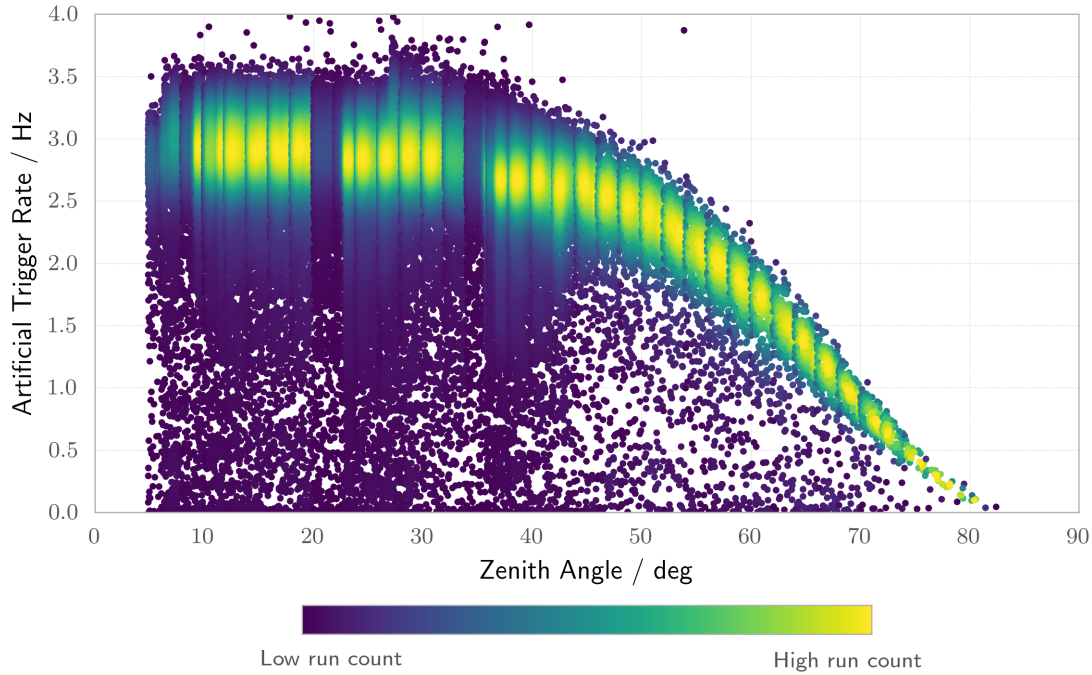
Figure 4.2 *Artificial Cosmic Ray Rate detected by FACT* The rate of cosmic rays as detected by FACT with an artificial trigger threshold applied is shown against the zenith angle of the observed patch in the sky. The colormap was normalized for bins of 4°-width in order to better illustrate the most observed CR rates in each bin. A clear drop-off of the CR rates towards larger zenith angles is observable, as well as decreased rates at lower zenith angles due to bad weather during observations. The vertical blue bars around 25° and 38° zenith angle are caused by sources culminating at these zenith angles, which introduces a bias into the number of rates at these zenith angles.

the observed rates of some measurement runs in all zenith angle bins. For this sample, observation runs with durations of at least 4 minutes from all sources were considered. The vertical blue bars around 25° and 38° zenith angle are caused by sources culminating at these zenith angles. FACT aims to observe sources at culmination, which is why there is a bias for runs taken at these angles.

In order to fit Equation 4.17 to the CR rate, the expected CR rate during good atmospheric conditions for each zenith angle bin of 4°-width is required. Therefore, the kernel density estimator (KDE) of the distribution of rates in each zenith angle bin is calculated (Parzen 1962). The distribution of rates in each bin typically looks like a Gaussian peak with a tail towards lower rates due to the observation runs during bad weather. The maximum value of the KDE represents the expectation value of the rates distribution and is therefore used as expected CR rate for at the corresponding zenith angle. The full width at half maximum of the peak in the KDE defines the uncertainty of this expectation value, see Figure 4.3.

The zenith angle dependence of the CR rate is now fit using Equation 4.17, assuming that the energy spectral index of CR protons follows a power-law $E^{-\beta}$ with spectral index $\beta = 2.7$ in Equation 4.10 (Aharonian et al. 2011). Figure 4.4 shows the resulting fit function in blue and the expectation values for the rates in each zenith angle bin in orange. The fit parameters are given in Table 4.1.
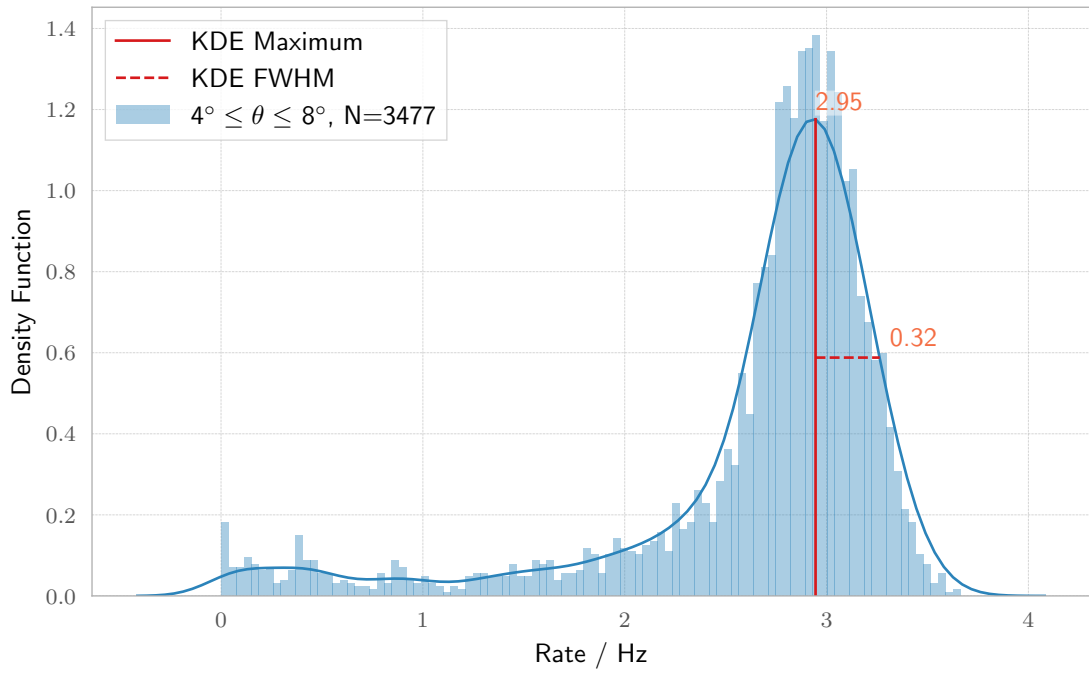
Figure 4.3 *Kernel Density Estimation of Cosmic Ray Rate in Zenith Angle Bin* The histogram shows the projection of the CR rates in the zenith angle bin $4° \geq \theta \geq 8°$ in Figure 4.2 onto the y-axis. The black lines depicts the KDE. The maximum of the KDE (red line) and the full width at half maximum (dashed, red line) are used as expectation value and standard deviation of the CR rate in this zenith angle bin. N gives the number of observation runs in this bin.
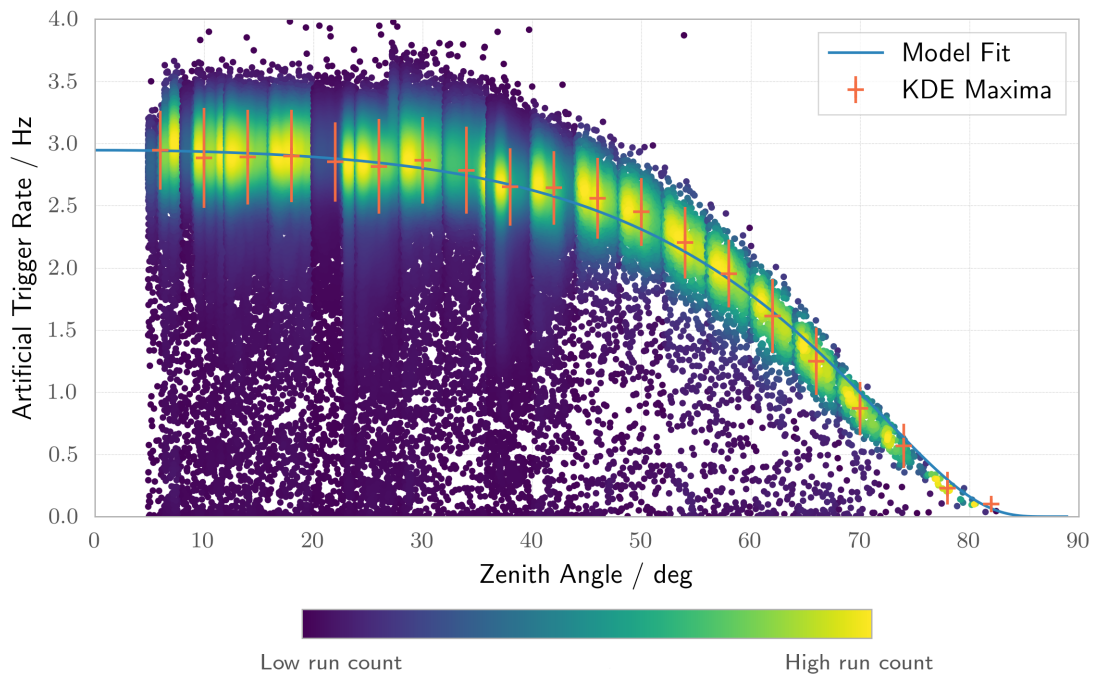

Figure 4.4 *Model Function Fit to CR Rate against Zenith Angle* Like Figure 4.2, but with the derived expectation values and uncertainties for each zenith angle bin superimposed in orange and the model fit function given in Equation 4.17 shown in blue. The fit parameters are given in Table 4.1.
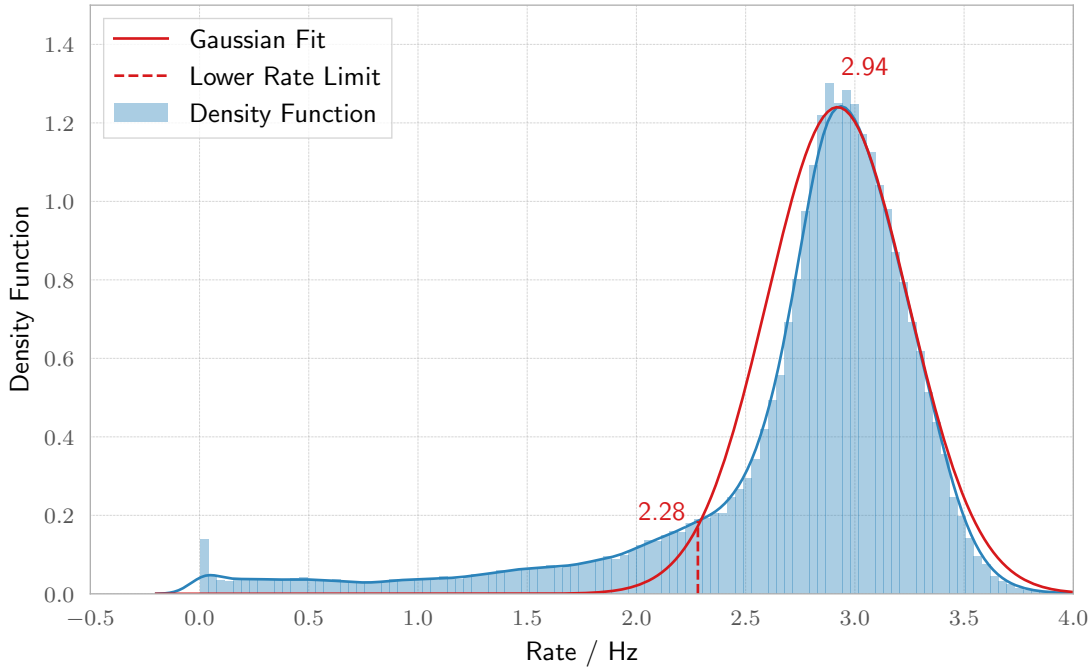
Figure 4.5 *Definition of a Bad-Weather Limit* The projection of the zenith angle-corrected cosmic ray rates is displayed by the blue histogram. The blue line depicts the KDE, whose maximum is fit with a Gaussian function (red line). The point where the Gaussian is equal to the KDE is defined as bad-weather limit, which is at 2.28 Hz.

Using the model function $c(\theta)$, the measured CR rate is corrected for the zenith angle dependence according to

$$R_{\mathrm{CR}}^{\mathrm{corr}} = c(\theta) \cdot R_{\mathrm{CR}}$$
$$\sigma(R_{\mathrm{CR}}^{\mathrm{corr}}) = c(\theta) \cdot \sigma(R_{\mathrm{CR}}) \tag{4.18}$$

The KDE of all corrected CR rates exhibits a peak around 3 Hz, with a drop-off towards lower rates, see Figure 4.5. Assuming there were no bad weather runs, the shape of the peak should follow a Gaussian distribution around the true CR rate. Therefore, the peak is fit with a Gaussian using a maximum likelihood estimation, returning a mean CR rate of (2.94 ± 0.01) Hz. The rate at which the Gaussian fit drops below the KDE is defined as bad-weather limit. Below this rate, there are more observation runs than would be expected. In the following analyses, observation runs showing CR rates smaller than the bad-weather limit of 2.28 Hz after correcting for the zenith angle dependence are filtered out.

The corrected CR rates over the zenith angle is shown in Figure 4.6. Both Figure 4.4 and Figure 4.6 show that the model function overestimates the zenith angle-induced decrease of the observed rates at zenith angles between 45° and 55°, while underestimating towards 65° to 75°. Still, the zenith angle correction of the artificial CR rate is successful and can be used to identify bad-weather runs.
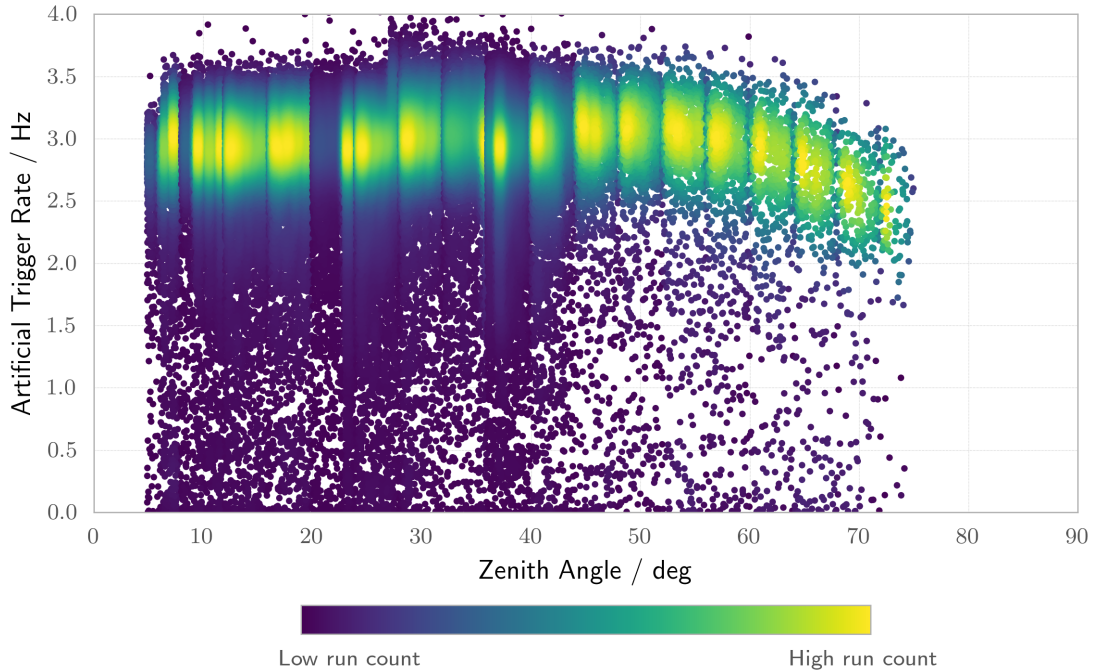
Figure 4.6 *Corrected Artificial Cosmic Rays Rate* Like Figure 4.2, but with the zenith angle correction applied according to Equation 4.18.

4.3.3 *Application to Rate of γ-rays*

Having defined the bad-weather limit using the rate of CRs, the zenith angle dependence of the γ-ray rates measured by FACT is corrected for. The working hypothesis is that the Crab Nebula emits a steady flux of γ-rates, therefore plotting the rate against the zenith angle should only reflect this dependence. Figure 4.7 shows the γ-ray rate of observation runs with observation times larger than 4 minutes of the Crab Nebula binned in zenith angle bins of 4° width. The bad-weather runs were removed using the just derived limit. The fit model function in Equation 4.17 is shown by the dashed, red line. The energy spectrum of the Crab Nebula follows a power-shape with $\beta = 2.47 \pm 0.01$ (Aleksić et al. 2015). The fit parameters are provided in Table 4.1. The γ-ray flux stays almost constant up to 25° zenith angle, therefore applying the correction function will hardly affect the run rates in this range. For zenith angles larger than 60°, the correction function increases the observed excess events by a factor of 10. As the model function tends to zero, the correction tends towards infinity. Observation runs at zenith angles larger than 60° are therefore excluded from the remaining analyses. This includes less than 1% of the data for the Crab Nebula and the Markarians.

A comparison of the raw data and the zenith angle and bad-weather corrected γ-ray data of the Crab Nebula is shown in Figure 4.8. It is apparent that the nights with bad weather (rates close to zero in the upper plot) have been successfully removed. One can also observe that the zenith angle correction over-corrects some runs in earlier observation epochs, e.g. between 56 900 and 57 000 MJD. These observations were taken at large zenith angles, where the correction function has a large influence. In
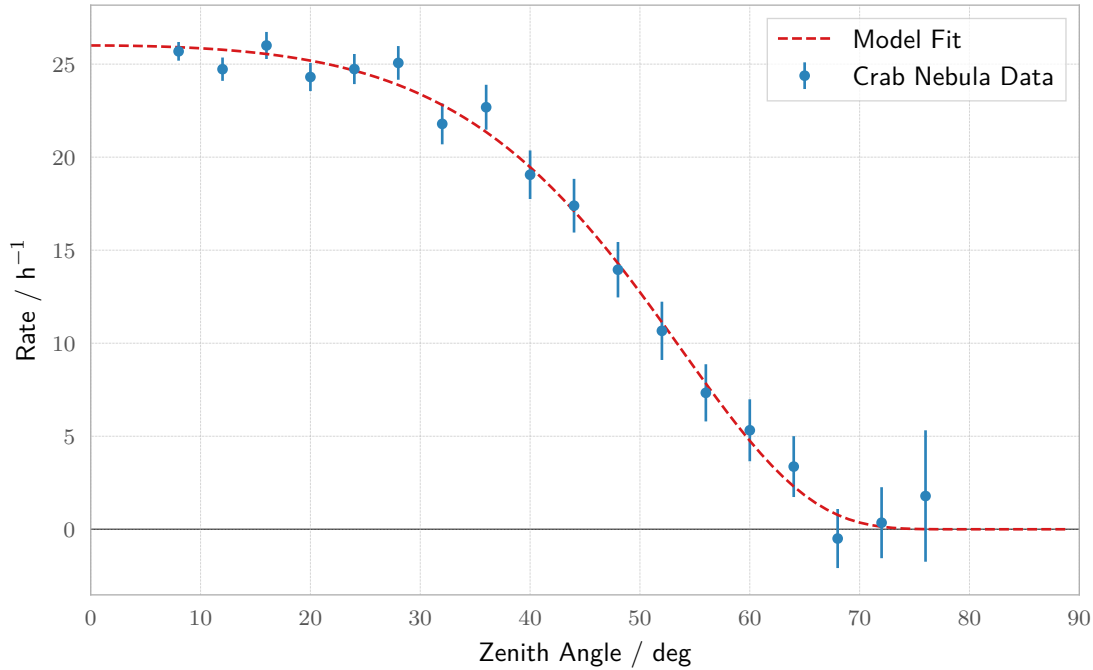
Figure 4.7 *Zenith Angle Dependence of Excess γ-rays from Crab Nebula* The blue markers show the binned run rates of the Crab Nebula. Bad-weather runs were removed with the bad-weather limit derived above. The dashed, red line represents the model fit function given in Equation 4.17. The fit parameters are given in Table 4.1.

Table 4.1 *Zenith Angle Model Function Fits* Fit parameters of Equation 4.17 to rate of cosmic rays and γ-rays over zenith angle using a least-squares approach.

	a	b	c
Artificial Cosmic Ray Rate	1.75 ± 0.05	0.33 ± 0.03	1.35 ± 0.05
Crab Nebula γ-ray Rate	0.61 ± 0.02	1.83 ± 0.05	1.15 ± 0.04

the past two years, noticeably fewer observations were taken at large zenith angles, therefore the correction is only marginal.

4.4 THRESHOLD DEPENDENCE

Besides the zenith angle dependence of the γ-ray rate, a dependence on the event trigger threshold is also expected because of the increasing night-sky background impeding the detection of signal events. In order to correct for this dependence, the Crab Nebula observation runs with observation times larger than 4 minutes and zenith angles below $30°$ are binned in threshold bins of $50\,\mathrm{DAC}$ counts, see Figure 4.9. Bad-weather runs were excluded using the bad-weather limit as derived above.
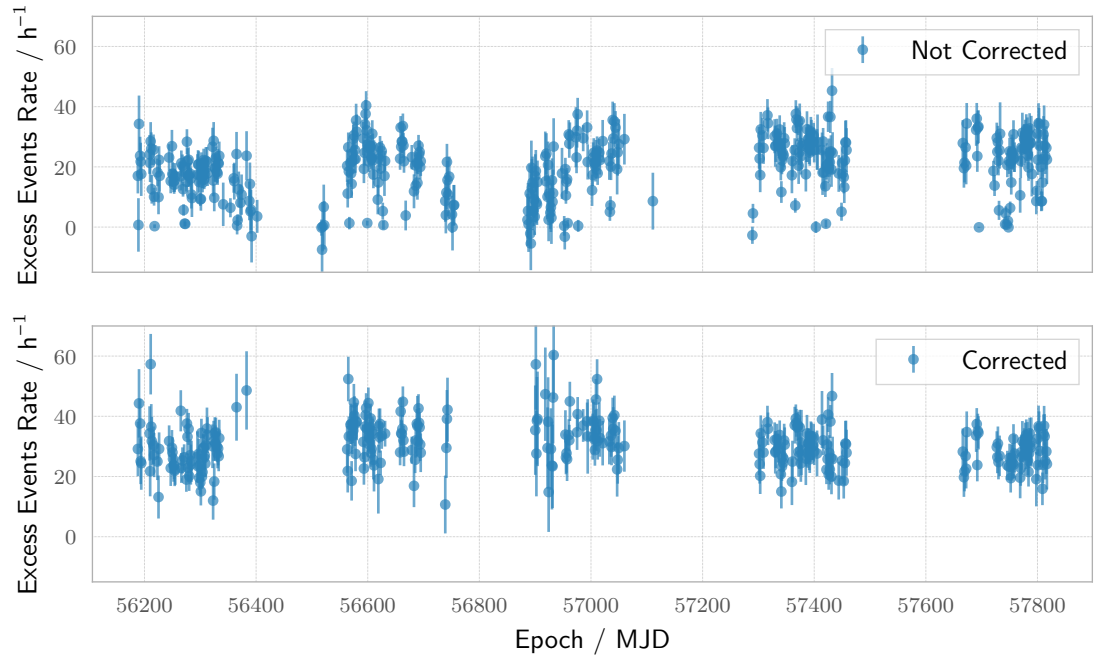
Figure 4.8 *Corrected γ-ray Rate of Crab Nebula* (Top) The nightly excess events rate of the Crab Nebula as recorded by FACT, using the raw data. (Bottom) The nightly excess events rate with the bad-weather observation runs removed and the zenith angle correction applied.
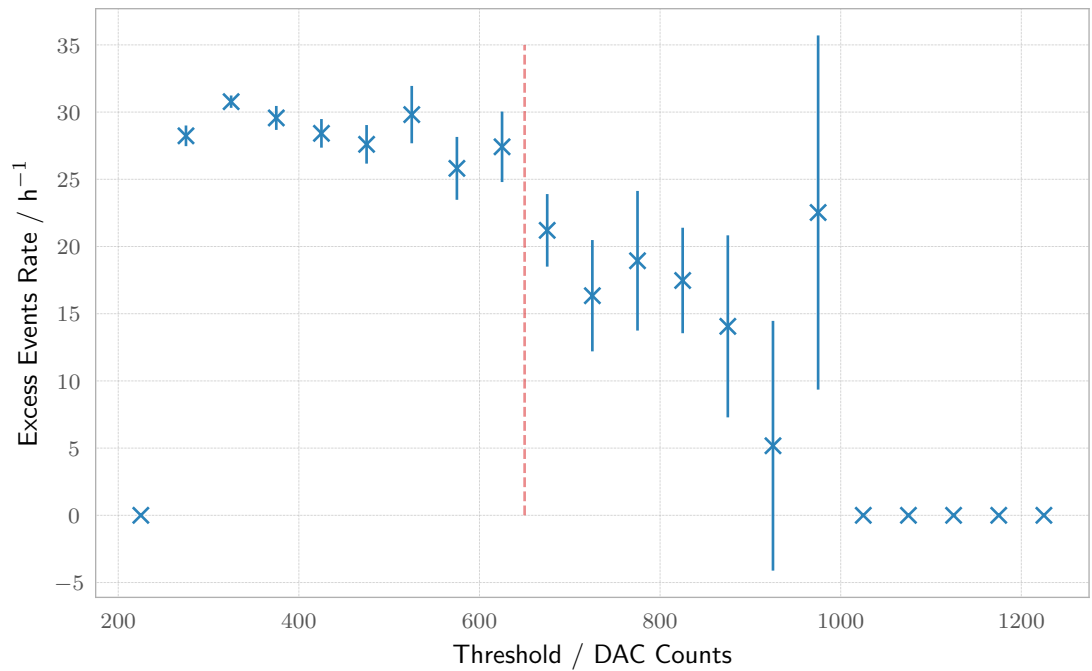
Figure 4.9 *Threshold-Dependence of Excess Events Rate of Crab Nebula* The binned Crab Nebula excess events rate versus the threshold in DAC counts are shown by the blue markers. Bad-weather runs are excluded, as well as observation runs at zenith angles larger than 30° to ensure that only the threshold-dependence affects the data. A jump in the rate around 650 DAC counts threshold is observable. A threshold-cut is therefore introduced into the data processing, illustrated by the dashed orange line at 650 DAC counts.

Figure 4.9 shows that the rates stay approximately constant for thresholds below 625 DAC counts, followed by a considerable drop around 650 DAC counts. Excluding observation runs with thresholds larger than 650 DAC counts reject 5% of the observation runs for the Crab Nebula (Mrk 501: 8%, Mrk 421: 8%). It is therefore decided that a cut at 650 DAC counts is preferred over a correction with a model function regarding the time constraints of this work.

4.5 FINAL DATA PROCESSING PIPELINE

This section summarizes the steps described above and outlines the pipeline from raw data to finished data product. Note that the raw data already underwent selecting and cleaning algorithms, therefore it is expected that the signal events only contain EM shower-induced events.

For each source, all observation run raw data is retrieved from the FACT database. This includes among other data the number of signal events, the number of background events, the observation time, the minimum, mean, and maximum threshold and zenith angle during the run, and the cosmic ray rate recorded using an artificial software trigger threshold.

As first steps, observation runs are rejected if any of these conditions is true:

- $T_{\mathrm{Obs}} \leq 240\,\mathrm{s}$

- $\mathrm{TH}_{\mathrm{mean}} \geq 650\,\mathrm{DAC}$ counts

- $\theta_{\mathrm{mean}} \geq 60°$

Next, bad-weather runs are identified using the artificial cosmic ray rate and the bad-weather limit defined above. The zenith angle correction function is then applied to the observed excess event rates of the remaining runs according to

$$
\begin{aligned}
R_{exc}^{corr} &= c(\theta) \cdot R_{exc} \\
\sigma(R_{exc}^{corr}) &= c(\theta) \cdot \sigma(R_{exc}).
\end{aligned}
\tag{4.19}
$$

A single measurement of a source is an integration of the photon rate over 5 minutes. To group these observation runs together into longer time intervals T, e.g. nightly rates and errors, the following equations are used

$$
\begin{aligned}
R_{exc}^{T} &= \frac{\sum_i N_{exc}}{\sum_i T_{obs}} \\
\sigma(R_{exc}^{T}) &= \frac{\sqrt{(\sum_i N_{sig})^2 + (\sum_i \alpha^2 N_{bg})^2}}{\sum_i T_{obs}},
\end{aligned}
\tag{4.20}
$$

where the index i includes all events that were recorded during the observation time T.

Besides the corrections and cuts described above, a further filter is applied. After calculating the nightly rates, it is found that nights with negative rates are also nights with short observation times. Assuming that the observation time was simply not long

enough to detect the source, all nights with $T_{\mathrm{Obs}} \leq 1\,\mathrm{h}$ are removed from the sample light curves.

In the following analyses, all FACT data measured before September 26, 2017 is included. The data pipeline, including the model of the zenith angle dependence, is implemented in the `peripylib` python package available on the GitHub repository of the thesis. For further information, refer to Appendix B.

PROBING THE PERIODICITY OF AGN WITH FACT

The variability of AGN from radio to γ-rays and over various time scales is both remarkable and puzzling. Characterizing the variability at different wavelengths and identifying emission zones is the key to understanding these sources, as outlined in Chapter 2.

The same chapter also lists some proposed mechanism in AGN which could result in a period signal component in their light curves. The detection of a periodicity in an AGN in the VHE regime could yield insights on the physical nature of the central engine, the black hole, and the radio jet. Models suggest characteristic time scales of this periodicity between minutes and years, which require both frequent and long-term observations of the candidate sources to uncover.

Periodicity in AGN has been claimed before, often in multi-wavelength studies combining the VHE data with other bands. Kranich (2001) claimed a 23-periodicity in Mrk 501 using data from the X-ray satellite RXTE and VHE γ-ray rates observed with the HEGRA experiment. Ackermann et al. (2015) combined high-energy γ-ray data with radio and optical properties to detect a modulation with a period of 2.18 ± 0.08 years in the blazar PG 1553+113. However, these claims are usually accompanied by small statistical significances, allowing no conclusive statement. The difficulty in this task lies in the stochastic nature of AGN. The analysis of time-series of a stochastic process can be misleading due to the intrinsic variability of the source, as will be outlined in this chapter.

The search for periodicities is further complicated due to the fact that astronomy and astrophysics are observational sciences. The objects of interest cannot be found on Earth or recreated in a laboratory. Hence, the time intervals for taking data are not always in the power of the observer, and are generally dictated by atmospheric conditions, the source position, telescope availability, or even that the spacecraft has to pause observation to establish data uplink and downlink. A set of unevenly sampled time-series is the result. The Fourier analysis of unevenly sampled data is commonly achieved with the Lomb-Scargle periodogram, which requires a detailed treatment of factors like the observation times in order to yield statistically reliable results.

The following analysis starts with a fundamental, theoretical look at the problem of time-series analysis of stochastic processes. The influence of the uneven sampling and the use of the Lomb-Scargle periodogram are illustrated with examples. Finally, the FACT time-series of the blazars Mrk 501 and Mrk 421 are characterised and searched for periodic components. The chapter concludes with an interpretation of the results.

5.1 CHARACTERISATION OF PHYSICAL PROCESSES

Time-series analysis is used to examine the temporal variability in light curves. This naturally leads to an analysis in Fourier space. The numerous possible processes occurring in AGN leave different footprints in the observed data, both in time- and frequency domain. The basis of the interpretation of the data are the mathematical models of the physical processes in the observed source. An intuitive first distinction of different model types are deterministic and non-deterministic (random) processes. At first glance, astrophysical sources appear non-deterministic, i.e. a reliable prediction of the future flux is not possible. This behaviour is inherent to the sources as the observed light curve is the sum of the numerous processes occurring within. It is the goal of time-series analysis to disentangle deterministic and stochastic pieces in this complex puzzle and to connect their parameters to the underlying physical mechanisms.

5.1.1 *Deterministic Processes*

The temporal evolution of data observed from deterministic processed can be predicted by mathematical expressions up to a certain accuracy. This data is usually acquired from classical systems. The revolution of the Moon around Earth and the revolution of Earth around the Sun can both be predicted in great detail using mathematical models of gravity. The relative positions in these gravitational systems are examples of *periodic deterministic variations*, with the periods being the sidereal year and the sidereal month. Other deterministic processes can show *multiple periodic variations*, such as the light curve of the ultra-cool dwarf star TRAPPIST-1, host star of a planetary system with seven terrestrial planets (Gillon et al. 2017), or *modulated periodic variations*, where frequency, amplitude, or phase of the periodicity vary over time. *Non-periodic deterministic processes* include transient states like the flaring phenomena observed in AGN or supernova explosions.

Deterministic processes can be expressed by a mathematical function $f(t)$. The definition of the complex Fourier transform $\mathcal{F}(\nu)$ is therefore straight-forward,

$$\mathcal{F}(\nu) = \int\limits_{-\infty}^{\infty} f(t) \mathrm{e}^{i2\pi\nu t} \mathrm{d}t, \tag{5.1}$$

following the notation from Deeming (1975). As $\mathcal{F}(\nu)$ is complex, it is more commonly examined as $\mathcal{P}(\nu) = |\mathcal{F}_D(\nu)|^2$. $\mathcal{P}(\nu)$ is referred to as the *power spectrum* of $f(t)$, or *power spectral density* (PSD). It describes the contribution of variations with frequency ν to the variance of $f(t)$. The definition in Equation 5.1 requires the integration of a continuous function over an infinite time interval. The practical situation of finite, discrete data sampled at times t_j demands the definition of a finite, discrete Fourier transform (DFT),

$$F_D(\nu) = \sum_{j=1}^{N} f(t_j) \exp(i2\pi\nu t_j). \tag{5.2}$$

This general definition of the Fourier transform does not restrict the temporal spacing of the data points, allowing for the arbitrary spacing that is common in astronomy and astrophysics. The squared absolute of the discrete Fourier transform $P(\nu) = A \cdot |F_D(\nu)|^2$

is the *periodogram.* The factor A is a normalisation factor and can be adapted to change the properties of the resulting periodogram. The periodogram is an estimate of the PSD just as the discrete Fourier transform is an estimate of the continuous Fourier transform[1] (Scargle 1982).

The left plot in Figure 5.1 shows a periodic process $f(t)$ and data $y(t)$ sampled from this process in time domain. The right plot shows the PSD (grey) and the periodogram (blue) calculated from the data $y(t)$ of the periodic process. The PSD is only non-zero at the frequency ν_0 of the process. The periodogram exhibits non-zero powers also at other frequencies.

The Fourier transform of a deterministic process is deterministic as well. Taking the data $y(t)$ with the same sampling at any other time will produce the same periodogram.
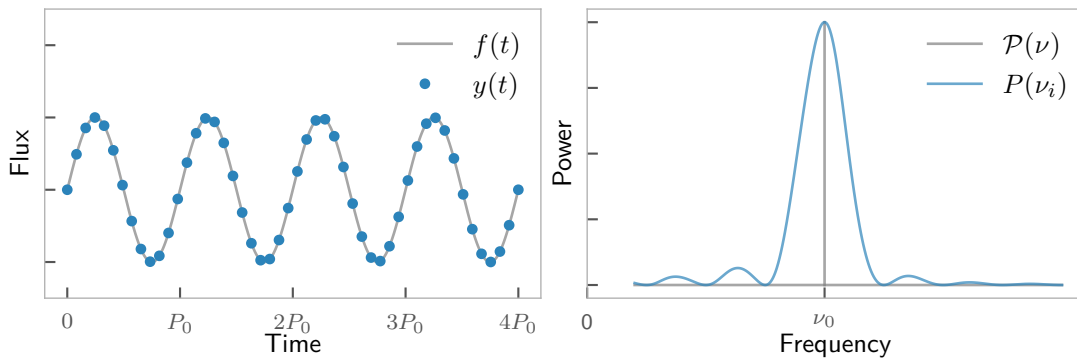

Figure 5.1 *Periodic Process in Time- and Frequency-Domain* The left plots depicts a periodic process $f(t)$ in grey and data $y(t)$ sampled from this process in blue. The PSD and the periodogram of the function and the data are shown on the right-hand side.

5.1.2 *Non-Deterministic Processes*

Non-deterministic behaviour is observed quantum-mechanical sources and in noise sources.[2] The indeterminism of these systems arises through the inherent probabilistic nature of quantum mechanics or through complexity. An example for the latter would be a many-particle system such as a gas. Deterministic data for each particle in the gas cannot be derived due to the complexity of the system, only statistical statements for the ensemble of particles can be made. Non-deterministic processes are therefore also referred to as *stochastic processes.*

The temporal evolution of non-deterministic behaviour caused be the complexity of the systems cannot be described with deterministic functions. Instead, it is described with probability statements, such as the probability distribution $\mathrm{Prob}(f(t))$ of the function $f(t)$ and its moments, the mean and the variance (Deeming 1975). Furthermore, astrophysical sources must show characteristic time scales or frequencies. A noise

---

1 The distinction between the true PSD of the source and its estimator, the periodogram, is important. Throughout this chapter, the function $f(t)$ describes the infinite, continuous signal that is emitted by the source, while $y(t)$ describes the discrete, finite data that is measured. Likewise, the true PSD of the source is denoted with a $\mathcal{P}(\nu)$, while the periodogram is marked with a $P(\nu)$. The continuous, infinite Fourier transform is given by $\mathcal{F}(\nu)$ as opposed to the discrete, finite Fourier transform $F(\nu)$.

2 The term *noise* here refers to the measured signal due to its intrinsic randomness, not to the measurement noise.

source without such a characteristic scale would emit *white noise*, exhibiting the same amplitude of variability on all time scales. This is physically not possible, as it would require instantaneous changes in the source to show variability at the smallest time scales, and an infinite memory of the process to show changes at the largest time scales. The characteristic time scales mean that the value of $f(t)$ is correlated with the value of $f(t - \tau)$. Multiple physical processes inside the source give rise to the variability on different time scales and influence each other to different degrees. Therefore, the amplitudes in the power spectrum may be correlated over a small or wide band of frequencies.

To infer on the population properties of the stochastic process, it is assumed that the statistical moments of the data sample are independent of the time t, i.e. that the joint probability distribution of the stochastic processes is constant over time. The source is regarded as stationary over the observation period. The correlation coefficient between $f(t)$ and $f(t - \tau)$ will then only depend on τ and is expressed in the *autocorrelation function $r(\tau)$*. The dependence of the noise process on the time is contained in $r(\tau)$, and its Fourier transform is the power spectrum of the noise process,

$$\mathcal{P}(\nu) = \int\limits_{-\infty}^{\infty} r(\tau) e^{i2\pi\nu t} dt. \tag{5.3}$$

Each measured time-series of a stochastic source is only one realisation of an ensemble of random time-series that result from the same inherent processes. Changes in the mean or variance of a data over the observation time therefore do not necessarily mean that the source has changed (Vaughan et al. 2003). The upper plot in Figure 5.2 illustrates this point. Depicted is the random light curve of a simulated source with an underlying PSD $\mathcal{P}(\nu) = \nu^{-2}$. The simulation is performed using the stingray python package[3], which applies the method introduced by Timmer and König (1995). The light curve shows times of larger and lower fluxes, as well as active and quiescent phases. This behaviour is possible for a stochastic process and does not imply that the underlying process changes.

Similarly to the fluxes in time-domain, the periodogram in frequency-domain is non-deterministic as well. Each periodogram is only one realisation of an ensemble of possible periodograms describing the same underlying PSD. As the real and imaginary parts of the DFT of a stochastic process are normally distributed, the distribution of the periodogram power at a frequency ν_i follows a χ^2 distribution with two degrees of freedom Priestley (1981); Vaughan et al. (2003),

$$P(\nu_i) = \mathcal{P}(\nu)\chi_2^2/2. \tag{5.4}$$

The mean of the χ_2^2 distribution is two and the variance is four. Therefore, the expectation value of the periodogram at any frequency ν_i is equal to the value of the true PSD at ν_i, while the standard deviation is 100%,

$$P(\nu_i) = \mathcal{P}(\nu) \pm \mathcal{P}(\nu). \tag{5.5}$$

Making inferences on the source's properties by looking at a single periodogram can lead to false conclusions, as the periodogram peaks are susceptible to large fluctuations.

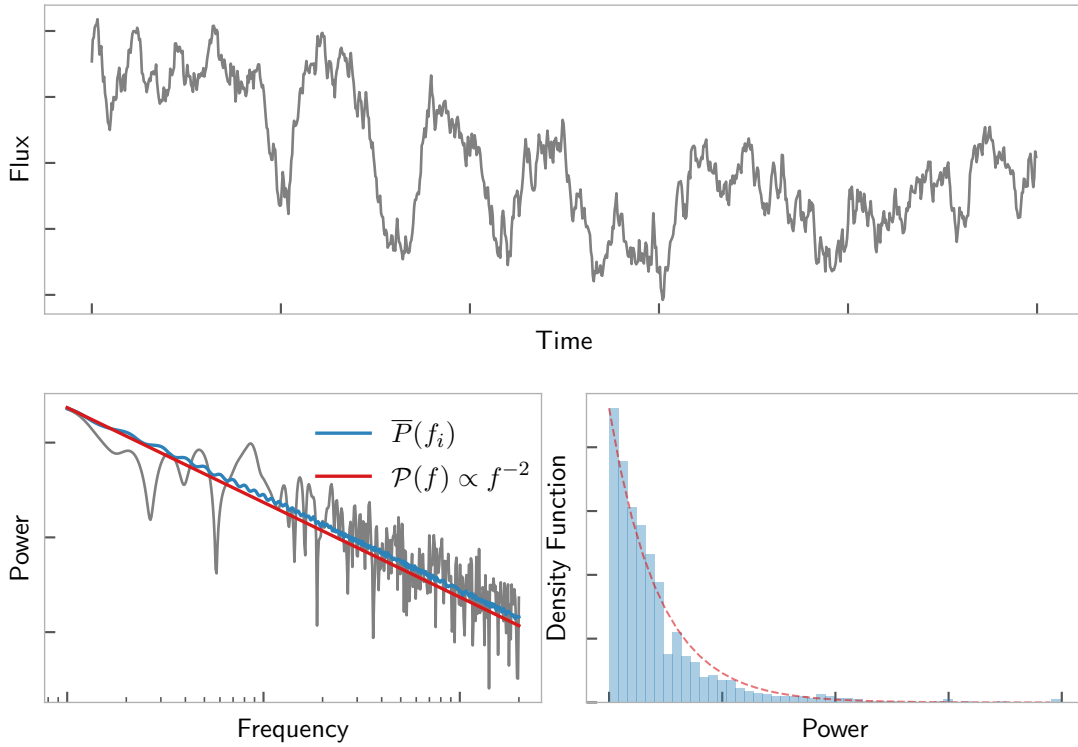3 https://github.com/StingraySoftware/stingray

Figure 5.2 *Statistics of Light Curves* The upper plot shows a random light curve which was simulated using an underlying random-walk PSD, $\mathcal{P}(\nu) = \nu^{-2}$. The bottom left plot shows the periodogram $P(\nu_i)$ in grey. The powers scatter in a wide range around the true PSD shown in red, following a χ_2^2 distribution. Simulating 1 000 light curves and calculating the mean periodogram powers gives the blue curve. The bottom right plot shows the distribution of the LSP powers $P(\nu_i)$ for a certain frequency ν_i of the 1 000 generated light curves. The dashed, red line shows the χ_2^2 distribution.

The bottom left plot of Figure 5.2 shows the periodogram of the evenly sampled, random light curve in the upper plot as grey line. Visible is a large scatter of the periodogram powers around the underlying PSD shown in red. Strong peaks are visible in the periodogram even though the underlying process is not periodic. This shows that the periodogram of any single light curve is not suited to infer on the source's properties. The blue curve shows the averaged periodograms of 1 000 simulated light curves, with the same underlying PSD. The average periodogram is a consistent estimator of the PSD, meaning that it converges towards the true PSD as the number of averaged periodograms increases. This behaviour can be observed in the blue line, which shows only little scatter around the true PSD. The bottom right plot shows the distribution of the periodogram powers $P(\nu_i)$ for a certain frequency ν_i of the 1 000 generated light curves. The dashed, red line shows the χ_2^2 distribution, which describes the shape of the histogram well.

5.1.3 *Astrophysical Sources*

In astrophysical sources like AGN, neutron stars, or X-ray binaries, the distribution of powers in the periodogram generally follows a power-law shape (Press 1978; Wijnands and van der Klis 1999; Uttley et al. 2002; Huppenkothen et al. 2013),

$$P(\nu) = A \cdot \nu^{-\alpha} + c. \tag{5.6}$$

This $1/\nu^{\alpha}$-type of noise is referred to as *red noise* and is observed in many physical processes, including outside of astrophysics. Electrical devices often exhibit *flicker noise*, where $\alpha = 1$. Another example is random-walk noise where $\alpha = 2$, see Figure 5.2 (Press 1978; Vaughan et al. 2003).

For AGN in particular, the slope of the spectra is well established for many sources from the optical to the high-energy range (e.g. Ruan et al. 2012; Sambruna 2006). In the VHE regime, the H.E.S.S. experiment has measured the slope of the periodogram PKS 2155-304 over 9 years and determined it to be in the range of flicker noise, $\alpha = 1.1$ (H.E.S.S. Collaboration 2016). Characterizing the variability of quiescent and flaring states separately, it was found that the power-law becomes harder during active phases with $\alpha \sim 2$, indicating that it is induced by a separate physical process. In addition, both the quiescent- and flaring-state flux distributions could be well described by log-normal distributions, which again is interpreted as evidence of different underlying phenomena occurring simultaneously (H.E.S.S. Collaboration et al. 2010).

The shape of the periodogram therefore classifies these astrophysical sources as stochastic. However, the observed sum of all processes inherent to the sources might contain deterministic, periodic components. The superposition of periodic process and a noise process produces a *quasi-periodic process* (QPO). Instead of delta peaks, which the Fourier transform of a periodic process produces, the Fourier transform of QPO show broader, possibly asymmetric peaks, which are variable in height due to the underlying modulating stochastic process. An example of a QPO in an astrophysical source is following in the next section.

5.2 THE LOMB-SCARGLE PERIODOGRAM

5.2.1 *Mathematical Framework*

This section addresses the practical calculation of the periodogram and introduces methods to deal with unevenly sampled data, the common case in astronomy and astrophysics.

Suppose there is a set of N data points sampled at arbitrary times t_j, $\{y(t_j), j = 1, 2, \ldots, N\}$, $y(t_j) = y_j$. The DFT of these measurements as given in Equation 5.2 is the basis of the periodogram,

$$
\begin{aligned}
P_f(\nu) &= \frac{1}{N}|F_D(\nu)|^2 \\
&= \frac{1}{N}\left|\sum_{j=1}^{N} y_j \mathrm{e}^{i2\pi\nu t_j}\right|^2 \\
&= \frac{1}{N}\left[\left(\sum_j y_j \cos(2\pi\nu t_j)\right)^2 + \left(\sum_j y_j \sin(2\pi\nu t_j)\right)^2\right]
\end{aligned}
\tag{5.7}
$$

This is the definition of the *classical periodogram*, which goes back to Schuster (1898). Assuming the data points y_j have an underlying periodic variation at the frequency ν_0, the periodogram will yield a large value when evaluated at ν_0, as the factors $y(t_j)$ and $\exp(-i\nu t_j)$ are in phase, and smaller values when evaluated at $\nu \neq \nu_0$, see Figure 5.1. However, the definition of the periodogram above using the DFT has disadvantages in the case of unevenly sampled data, as the sine and cosine functions form an orthogonal set of basis functions only for even sampling. Therefore, while the periodogram powers $P(\nu)$ for evenly sampled data follow a simple exponential distribution, the powers in the uneven sampling case are correlated and the statistical behaviour is much more complicated. Scargle (1982) therefore proposed a new definition of the periodogram,

$$
P_f(\nu) = \frac{1}{2}\left\{\frac{\left[\sum_j y_j \cos[2\pi\nu(t_j-\tau)]\right]^2}{\sum_j \cos^2[2\pi\nu(t_j-\tau)]} + \frac{\left[\sum_j y_j \sin[2\pi\nu(t_j-\tau)]\right]^2}{\sum_j \sin^2[2\pi\nu(t_j-\tau)]}\right\},
\tag{5.8}
$$

where the factor τ is used to orthogonalize the sine and cosine functions and is given by

$$
\tan(2\omega\tau) = \frac{\sum_{i=1}^{N} \sin 2\omega t_i}{\sum_{i=1}^{N} \cos 2\omega t_i}.
\tag{5.9}
$$

This is known as the *Lomb-Scargle periodogram* (LSP). For the case of even sampling, the definition reduces to the classical periodogram given in Equation 5.7. It provides the same statistical behaviour in the power distribution for unevenly sampled data as the classical periodogram exhibits for evenly sampled data, given in Equation 5.4. **One important caveat, however, is that the statistical behaviour can only be analytically calculated assuming white, uncorrelated noise on the observations.** For red-noise processes, the powers at different frequencies in the LSP are correlated. The description of this correlation is non-trivial and requires extensive Monte-Carlo simulations to quantify.

A remarkable property of the LSP is that it is equivalent to the approach of least-squares spectral analysis (LSSA). For the set of N data points described above with uncertainties σ_j, the LSSA approach defines a model function,

$$
y(t_j) + \sigma_j = a \cos[\omega(t_j-\tau)] + b \sin[\omega(t_j-\tau)]
\tag{5.10}
$$

where $\omega = 2\pi\nu$ is the angular frequency and τ is again given by Equation 5.9 (Lomb 1976). The χ^2 statistic at each frequency ν is

$$\chi^2 = \sum_{j=1}^{N} \frac{[f(t_j) - y(t_j)]^2}{\sigma_j^2}. \tag{5.11}$$

The best fit model function is then found by minimising the χ^2 statistic at each frequency, which will be denoted as $\chi_{min}^2(\nu)$. The normalised power spectrum $P_{LS}(\omega)$ can then be written as

$$P_{LS}(\omega) = \frac{\chi_0^2 - \chi_{min}^2(\nu)}{\chi_0^2} \tag{5.12}$$

where χ_0^2 is the squared difference of the null hypothesis, i.e. that the data is sampled from a constant signal with noise (Zechmeister and Kürster 2009). The power $P_{LS}(\omega)$ in the LS periodogram therefore essentially expresses how much better a sinusoid with given angular frequency ω explains the data than a constant signal with a added noise. It is equivalent to a brute-force least-squares fitting approach. The equivalence of both methods, the periodogram analysis and the LSSA, is shown e.g. in Scargle (1982, Appendix C). The LSP was further improved by Zechmeister and Kürster (2009) into the Generalised Lomb-Scargle (GLS) periodogram, allowing for model functions with means unequal to zero.

The grid of frequencies the LSP is evaluated on is chosen based on the timestamps of the measurements. The minimum frequency is equal to the inverse of the total observation time T_{Obs}. The maximum frequency is chosen using the Nyquist frequency for irregular sampling as derived by Eyer and Bartholdi (1999). The derivation assumes that the data is sampled on a theoretical grid of even spacing, but that some data is missing. The spacing of the theoretical grid is the minimum time-step p between two measurements. Eyer and Bartholdi (1999) then show that the maximum frequency for the periodogram evaluation is given by

$$\nu_{Ny} = \frac{1}{2p}. \tag{5.13}$$

To ensure that that the smaller frequencies are sampled as densely as the larger frequencies, the grid is computed in log-space,

$$\nu \in \{10^{\log \nu_{\min}}, 10^{\log \nu_{\min+1}}, \dots, 10^{\log \nu_{\max}}\}, \tag{5.14}$$

where $\{\nu_{\min}, \nu_{\min+1}, \dots, \nu_{\max}\}$ are evenly spaced.

The number of evaluated frequencies should be equal to the number of independent frequencies in the periodogram. However, due to the uneven sampling, the number of independent frequencies is not readily available. Choosing too many frequencies will increase the statistical penalty of the Look-elsewhere effect (Vaughan 2005), while choosing too few frequencies can lead to entire peaks being missed in the periodogram. As an estimate, the number of independent frequencies is assumed to be equal to the number of data points.

For a more thorough introduction to the LSP, the reader is directed to Lomb (1976); Scargle (1982); Zechmeister and Kürster (2009). For a guide on the practical application of the periodogram and its caveats, see VanderPlas (2017).

5.2.2 *The Spectral Window*

The periodogram is an estimator of the true power spectrum of the source and therefore subject to biases. The transition from the theoretical, ideal world, where a source is observed continuously and for an infinite amount of time, to the real world, where measurements are finite and discrete, leaves its imprints on the periodogram and may lead to misinterpretation of the results if the effects are not considered correctly.

The step from the theoretically infinite source function $f(t)$ to the finite data sample $y(t)$ can be thought of as a multiplication of $f(t)$ with a rectangular function. This function is 1 if t is between the start and the stop of the observation and 0 otherwise. Similarly, the transition from the continuous $f(t)$ to the discrete $y(t)$ is equivalent to multiplying $f(t)$ with a function which is 1 if data was taken at time t and 0 otherwise, which is referred to as a Dirac comb. This is the definition of the *window function* $w(t)$, which for data sampled at times t_j in the time-domain is given by

$$w(t) = \begin{cases} 1 & t \in t_j \\ 0 & t \notin t_j \end{cases}$$

According to the convolution theorem, a multiplication in time-domain equals a convolution in frequency-domain (Arens et al. 2015),

$$y(t) = f(t) \cdot w(t) \Leftrightarrow F(\nu) = \mathcal{F}(\nu) * \mathcal{W}(\nu), \tag{5.15}$$

were $\mathcal{W}$ is the Fourier transform of the window function, the *spectral window*, and $*$ the convolution operator. Equation 5.15 states that multiplying the source function $f(t)$ with the window function $w(t)$ to get the measurement data $y(t)$ is equivalent to convolving the source PSD with the spectral window. The Fourier transform of a rectangular function is a sinc function. The convolution of the source PSD with a sinc function will broaden the peaks and create sidelobes, artificial peaks adjacent to actual peaks in the periodogram. The relation between the broadening and the width of the rectangular function is inverse: The longer the observation period is, the less the peaks are broadened by the sinc function. The influence of the finite observation window on the periodogram is referred to as *windowing.*

In addition to the broadening of peaks, the finite observation time also causes *spectral leakage*: For red-noise processes, variability is strongest on large time scales. Any observed light curve will contain variations on time scales larger than the observation times. In the periodogram, power is transferred from the long-term variability to large frequencies. This *red-noise* leakage causes the periodogram to exhibit a flatter spectral index. The amount of distortion due to red-noise leakage depends on the PSD of the process and the observation length (Papadakis and Lawrence 1993).

The convolution of a Dirac comb with a spacing of T between the peaks is a Dirac comb function with a spacing of $1/T$. The convolution of the PSD with the Dirac comb will therefore create *alias peaks* in the periodogram. For evenly sampled data, these aliases have an even spacing and can be identified easily. For unevenly sampled data, the convolution of the underlying PSD with the Dirac comb results in a mess of artificial peaks which are difficult to tell apart from real peaks. The appearance

of spurious peaks in the periodogram due to the discrete sampling is referred to as *aliasing* (Deeming 1975).

The windowing effect can be observed in the periodogram shown in Figure 5.1. The peak of the periodogram resembles a sinc function. Further illustrative examples can be found in VanderPlas (2017).

However, while the FACT data samples are unevenly-spaced, the gaps in the data are structured. Enforced observational patterns like the monthly stop of observations during full Moon leave their imprints in time- as well as in Fourier domain. This is illustrated in Figure 5.3, which shows the spectral window of the FACT Crab Nebula observations, i.e. the periodogram of the window function. The strongest peak in the periodogram has a period of 372 days, close to one sidereal year. Every sidereal year, the Crab Nebula is in the same position in the sky as seen from Earth. Therefore, observational breaks related to the source visibility repeat every year, which is observable in the periodogram. The sidelobes of this strong peak are clearly visible and are caused by the windowing effect.

The second and third strongest peaks in Figure 5.3 are the sidereal and synodic month. The synodic month is characterised by the time between two full Moons, about every 29.5 days. Observations rest when the Moon is too bright[4], therefore this repeating break is imprinted in the frequency-domain. The sidereal moon period is the time it takes the Moon to revolve once around Earth, which is 27.3 days. Figure 3.2 shows that the Crab Nebula is close to the ecliptic plane. As the Moon revolves around Earth, it will come close (in angular separation) to the Crab Nebula every 27.3 days and the source is blocked by the Moon. Note that the lunar periods show much sharper peaks in the periodogram than the sidereal period as the lunar periods were observed 48 times, while the observations cover only about 4 sidereal years.

The strong features in the spectral window will lead to strong aliasing in the periodogram of the FACT data. The position of these aliased can be calculated assuming that the frequency of a true peak in the periodogram is known. In practice, the large intrinsic scatter of the periodogram powers can lead to erroneous conclusions. Monte Carlo simulations of light curves using the same uneven sampling are a safer approach here.

Furthermore, the convolution with the spectral window affects the spectral index α of the periodogram. Figure 5.4 shows the convolution (blue) of the spectral window of the FACT Mrk 501 observations (grey) with a power-law PSD with $\alpha = 1.5$ (dashed, red line). It can be seen that the convolution shows lower variability at smaller frequencies. Again, to quantify this effect for different underlying noise processes, extensive Monte Carlo simulations have to be applied.

The spectral windows of the observations of Mrk 501 and Mrk 421 are in Appendix A, Figure A.1 and Figure A.2. The same peaks are observable, while the sidereal lunar period is less pronounced due to the larger declinations of the Markarians in comparison to the Crab Nebula.

---

4 The FACT telescope could in principle observe sources during full Moon and has already done so, see Knoetig et al. (2013). However, for security reasons, the remote operations have to stop when the crew of the neighbouring MAGIC telescope is not on site. Therefore, as MAGIC does not observe during full Moon, neither does FACT.
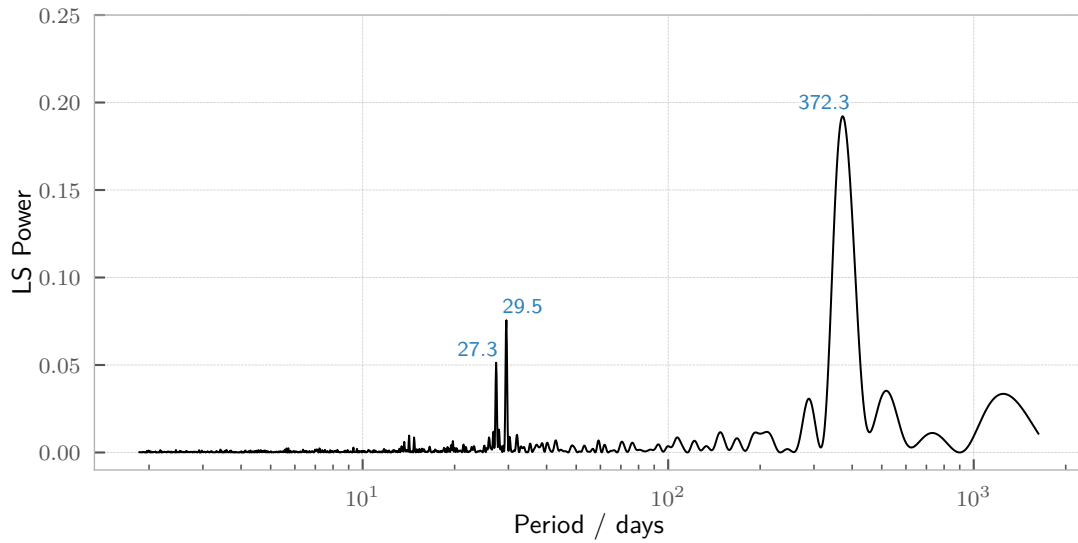
Figure 5.3 *Spectral Window of FACT Crab Nebula Observations* The periodogram of the window function of the Crab Nebula observations reveals repeating patterns in the observations. The strongest peak at 372 days is related to the sidereal year. The two smaller peaks at 27.3 and 29.5 days are the sidereal and synodic lunar periods.
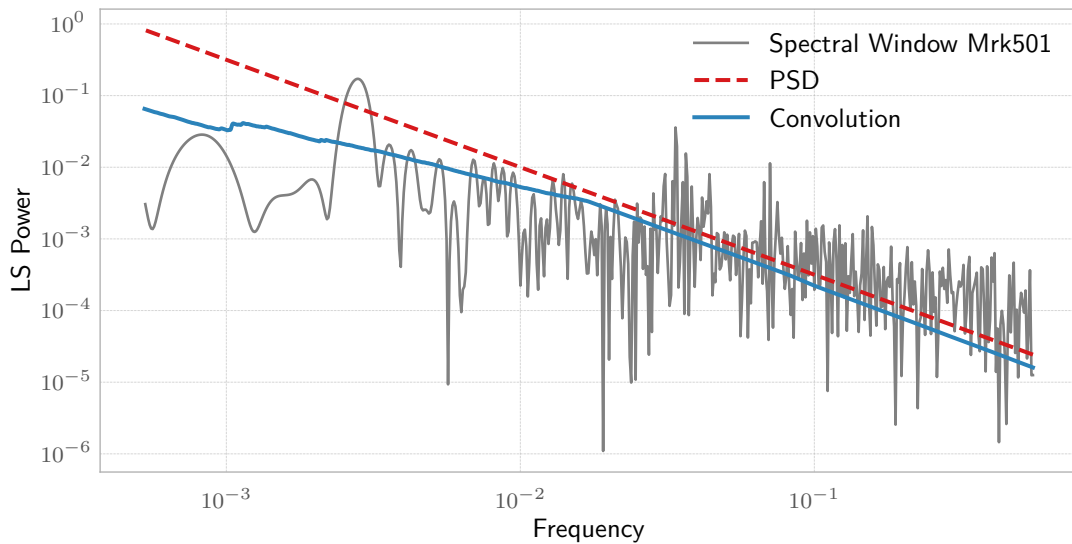

Figure 5.4 *Convolution of Spectral Window of FACT Mrk 501 Observations with Power-Law PSD* The convolution of the underlying noise process PSD (dashed, red line) with the spectral window of the Mrk 501 observations (grey) decreases the variability at small frequencies in the periodogram (blue).

5.2.3   *Example of Time-Series Analysis with the LSP: Sunspots*

The application of the periodogram and its equivalence to the LSSA approach are now illustrated with an example. The upper plot in Figure 5.5 shows the number of sunspots visible in the Sun's photosphere. The number of these spots has been recorded for centuries and is known to periodically vary about every 11 years (Schwabe 1844). It is therefore a prime dataset for the application of the LSP.

In Figure 5.5, the upper plot shows the monthly number of sunspots for the past 200 years. The data is gathered by the Royal Observatory of Belgium[5]. While the data from the 19th and early 20th century contains gaps, more recent observations have been recorded thoroughly. To simulate uneven sampling, 90% of the available data is removed at random. The remaining data is plotted and fit with the model function given in Equation 5.10, shown as dashed, red line. The bottom plot shows the LSP of the sunspot data. The `astroML python` package is used to calculate the LSP, see Ivezić et al. (2014). A prominent peak is visible at a period of 10.9 years. Shown as dashed, red line is the period obtained with the LSSA approach, which is equal to the period of the maximum peak in the periodogram.
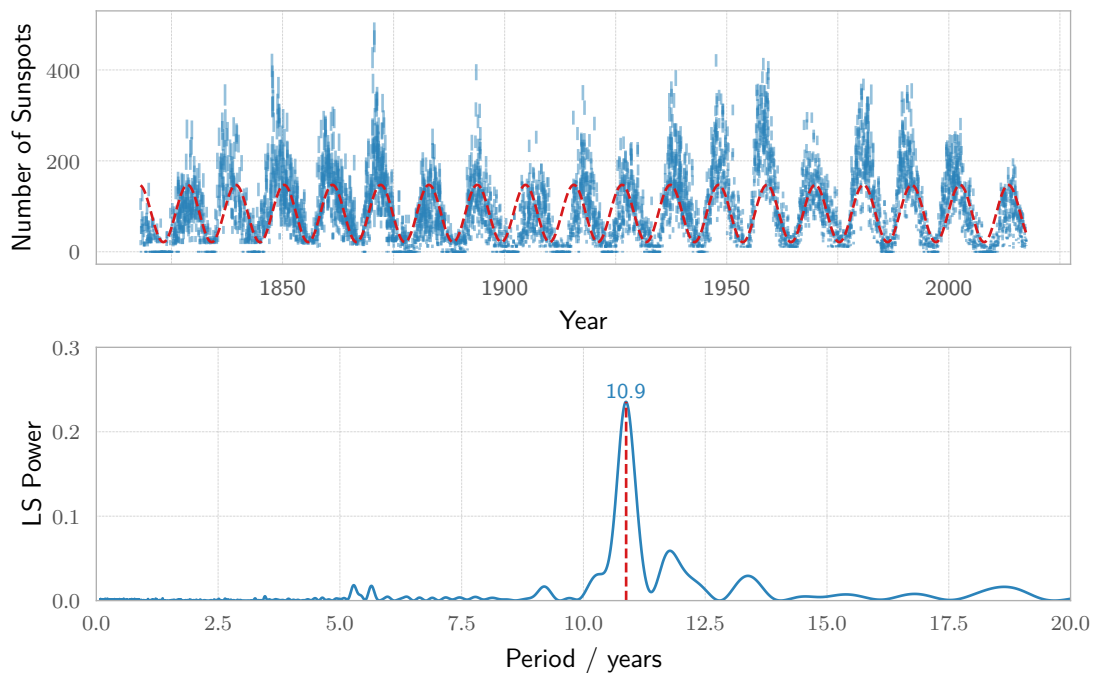

Figure 5.5 *Lomb-Scargle Analysis of Sunspot Number* Shown in the upper plot are 10% of the monthly number of sunspots recorded over the past 200 years. The dashed, red line shows the fit of the sinusoid model function given in Equation 5.10. The bottom plot shows the Lomb-Scargle periodogram of the data in blue and the period of the best fit function as dashed, red line. The monthly sunspot data can be found at http://www.sidc.be/silso/datafiles.

Both the time-series and the periodogram in Figure 5.5 show that the number of sunspots varies with a period of about 11 years. However, it is also visible that this period is not stable: The sine fit and the data in the upper plot do not depict good

---

5   The used dataset is the monthly number of sunspots found at http://www.sidc.be/silso/datafiles.

phase coherence. In addition, the peak in the periodogram is broadened. Both are signs that the solar activity is a QPO. For the solar activity, it can be shown that periodic process is distorted by a flicker noise process (Priestley 1981; Frick et al. 1997).

5.3 THE VARIABILITY OF MRK 501 AND MRK 421

With the theory well established, the focus now turns to the FACT measurements of the blazars Mrk 501 and Mrk 421. Before investigating the periodicity of both sources, the more general variability is characterised both in time- and in frequency-domain.

5.3.1 Time Domain

Figure 5.6 depicts the FACT nightly light curves of Mrk 501 and Mrk 421 from March 2012 to September 2017. The upper plot shows the light curves after applying the corrections and cuts described in Chapter 4. The largest gaps in both light curves are caused by the annual visibility patterns of both sources (see Figure 3.2). Both sources show active and quiescent states. The bottom plot shows the mean flux level $\bar{R}$ for bins of 10 days against the excess variance σ_{XS}^2,

$$\bar{R} = \frac{1}{N} \sum_{i=1}^{N} R_i$$

$$\sigma_{XS}^2 = S^2 - \bar{\sigma}_R^2 \tag{5.16}$$

where N is the number of nightly rates in the 10-day bin, S^2 the rate variance and $\bar{\sigma}_R^2$ the mean squared rate error of each time bin,

$$S^2 = \frac{1}{N-1} \sum_{i=1}^{N} (R_i - \bar{R})^2$$

$$\bar{\sigma}_R^2 = \frac{1}{N} \sum_{i=1}^{N} \sigma_{R,i}^2 \tag{5.17}$$

Subtracting the mean squared error $\bar{\sigma}_R^2$ from the variance ensures that the plotted excess variance is due to the intrinsic variability of the light curve, not the Poisson measurement uncertainties (Vaughan et al. 2003). To ensure that the binned values are comparable, only bins with more than 7 nights of observations are shown. A positive correlation between the mean flux and the variance is observable. Indeed, the linear relation between the mean flux level and the root mean square of flux variations in AGN has been observed both in X-ray energies (e.g. Uttley and McHardy 2001) and in TeV energies (H.E.S.S. Collaboration 2016).

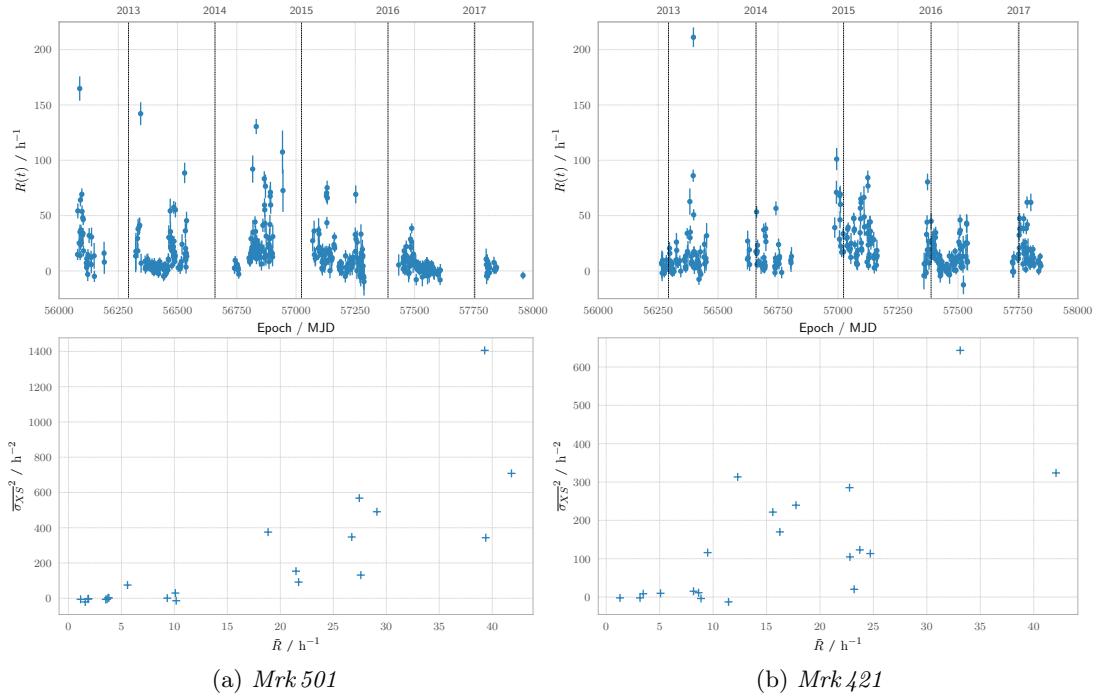(a) *Mrk 501*   (b) *Mrk 421*

Figure 5.6 *FACT Light Curves of Markarians* The 5-year light curves of Mrk 501 and Mrk 421 observed with FACT. The upper plot shows the nightly rates with the corrections and cuts applied as mentioned in Chapter 4. The dotted, black lines mark January 1 of the given year. The bottom plot shows the mean rate in bins of 10 days against the excess variance of the rates in the time bins. A positive correlation between the variance and the mean flux visible.

5.3.2 *Frequency Domain*

To investigate the shape of the power spectra, the Lomb-Scargle periodograms of Mrk 501 and Mrk 421 are fit with the power-law function given in Equation 5.6. The best fit power-law is shown in red. The fit parameters are acquired with a maximum likelihood approach and given in Table 5.1. Both LSPs have spectral indices $\alpha < 1$, with $\alpha = 0.72 \pm 0.04$ for Mrk 501 and $\alpha = 0.51 \pm 0.03$ for Mrk 421. Both periodograms exhibit the strong peaks around 30 days and in the range of 100 to 300 days.

The LSPs of the light curves using the run-wise binning could reveal periodicity on smaller time scales, assuming the periodic process is stable over 5 years. The LSPs and the power-law fits are shown in Figure 5.8, the parameters are given in Table 5.1. The periodograms of both sources are well described with the power-laws with $\alpha \approx 0.7$ over several decades of frequencies. The range between 1 and 10 days shows strong aliasing of the 1 day peak, which is caused by the diurnal observation pattern. This range is therefore excluded from the fit. Again, Mrk 501 shows a marginally harder spectrum than Mrk 421.

The spectral indices of the Markarians both for nightly and for run-wise binning are noticeably smaller than the spectral indices measured in X-ray, HE- and in VHE γ-rays for other blazars, $\alpha \sim 1 - 2$. While this is a possible result, it does warrant a closer look.

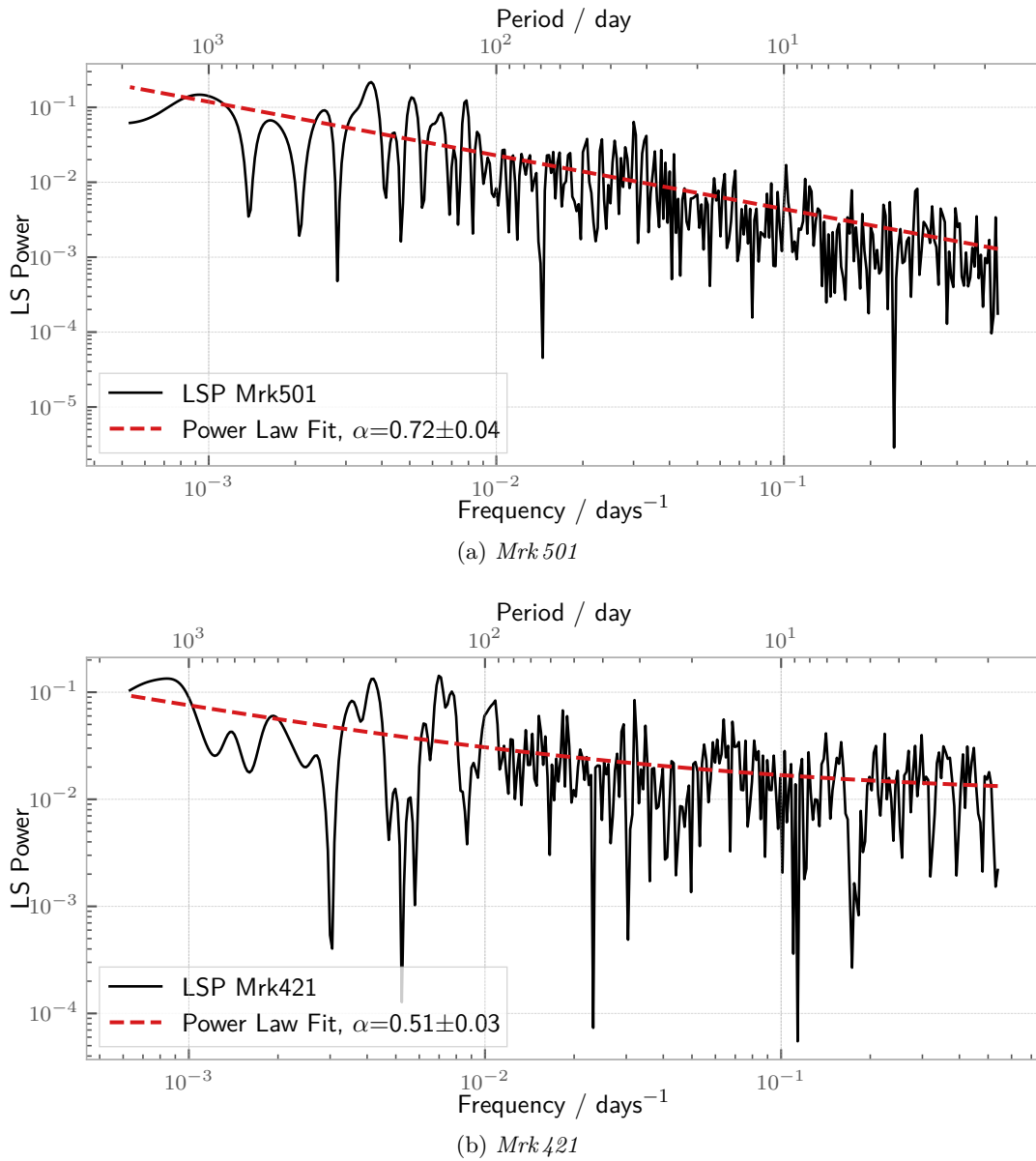(a) *Mrk 501*

(b) *Mrk 421*

Figure 5.7 *LSPs of Nightly-Binned Markarians Data* On top, the Lomb-Scargle periodogram of the FACT Mrk 501 data is shown in black, using nightly binning. The dashed, red line shows a power-law fit. The bottom plot shows the same result for Mrk 421. Both LSPs show strong peaks around 30 days and in the range between 100 and 300 days.

(a) *Mrk 501*

(b) *Mrk 421*
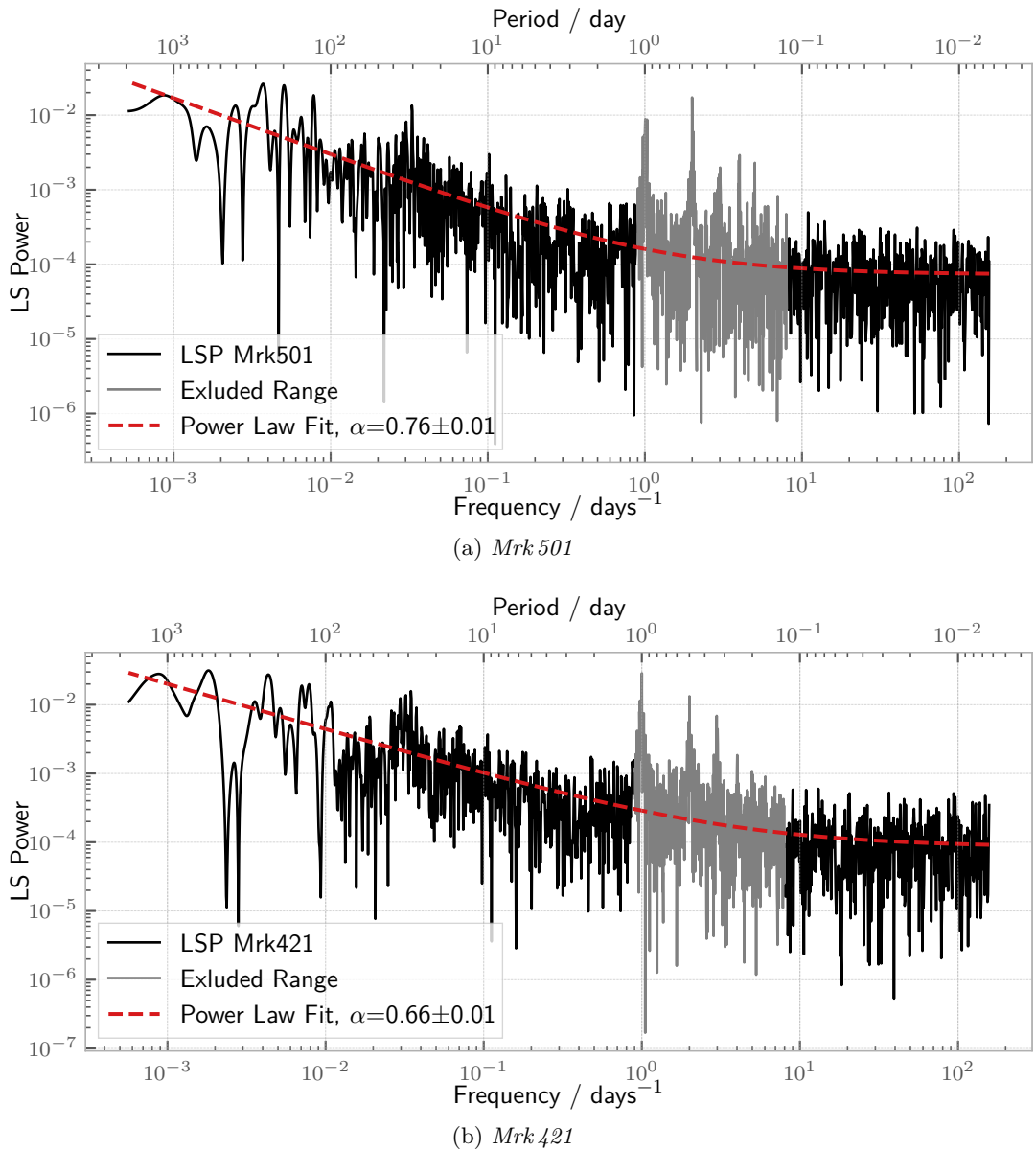
Figure 5.8 *LSPs of Markarians Run Data* On top, the Lomb-Scargle periodogram of the FACT Mrk 501 data is shown in black, where the periodogram was calculated using the single run rates. Therefore, the periodogram was evaluated up to two more orders of magnitudes in frequency than in Figure 5.7. The dashed, red line shows a power-law function fit. The grey-shaded frequencies are excluded from the fit due to strong aliasing of the 1-day frequency peak. The bottom plot shows the same result for Mrk 421.

Table 5.1 *Power-Law Fit Parameters:* The parameters of the power-law model function given in Equation 5.6 for the fits of the nightly-binned and run data periodograms of the Markarians shown in Figure 5.7 and Figure 5.8.

	Mrk 501		Mrk 421	
	Nightly	Run	Nightly	Run
$A/1 \times 10^{-4}$	8 ± 0.4	0.9 ± 0.04	18 ± 1	2 ± 0.1
α	0.72 ± 0.04	0.76 ± 0.01	0.51 ± 0.03	0.66 ± 0.01
$c/1 \times 10^{-4}$	$0.009 \pm 3 \times 10^{-4}$	0.8 ± 0.04	107 ± 5	0.8 ± 0.04

A significant factor of this result is the uneven sampling. As shown in Figure 5.4, convolving the PSD of a noise process with the FACT spectral window bends the spectrum, effectively decreasing the spectral indices of the periodograms. In order to quantify this effect, a simulation study is performed. Using the Timmer and König (1995) method, light curves are simulated with an underlying power-law PSD. The spectral index of the PSD is increased from 0.5 to 1.5 in steps of 0.05. For each step, 1 000 light curves are generated. For each light curve, the LSP is calculated once with even time-steps between the light curve data points and once with the FACT sampling of the nightly-binned data. The mean periodograms of the 1 000 light curves are then fit with a power-law function. Figure 5.9 compares the spectral index used to simulate the light curves with the spectral indices from the fits of the evenly sampled and unevenly sampled periodograms, using the timestamps of the Mrk 421 observations. The same graph for the Mrk 501 observations can be found in Appendix A, Figure A.3.

Figure 5.9 shows that the periodograms of the simulated light curves with even sampling closely follow the shape of the underlying PSD, the red points are close to the $x = y$-line. Using the FACT timestamps (i.e. convolving the PSD with the spectral window) significantly decreases the spectral index, which is depicted by the blue points. A power-law spectral index of 0.5 in the simulated FACT periodogram required a spectral index around 0.8 of the underlying PSD. While the FACT periodograms of Mrk 501 and Mrk 421 do not necessarily have simple power-law shapes and might be better described with more sophisticated models, this study is a strong hint that the actual spectral indices of the Markarians are closer to 1 than the LS periodogram represents. The range of $0.5 \geq \alpha 0.76$ of spectral indices fitted in the FACT data corresponds to underlying spectral indices of $0.8 \geq \alpha 1.2$ in the simulated light curves.
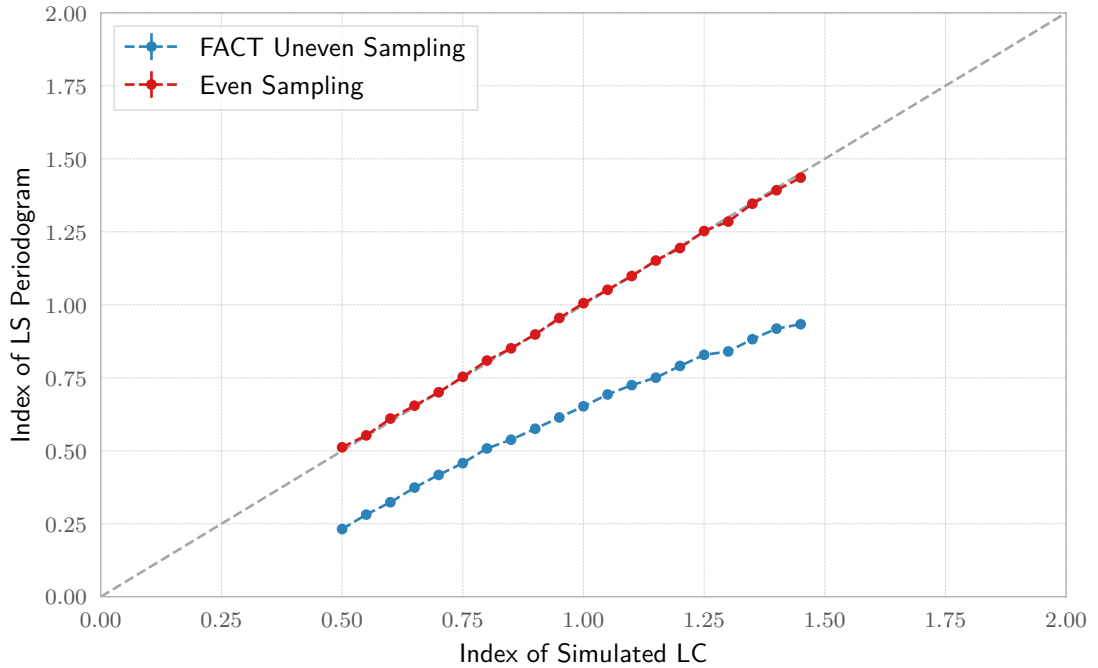
Figure 5.9 *Comparison of Simulated Spectral Index and Spectral Index of LSP* Simulations are
performed to investigate the effect of the uneven sampling on the retrieved spectral
index of the LSP. Using spectral indices in the range of 0.5 to 1.5, 1 000 light curves
are simulated assuming underlying power-law PSDs. The spectral indices of the
mean periodograms using the even sampling (red) and the Mrk 421 sampling of
FACT (blue) for the light curves are compared. The errors on the spectral indices
are smaller than the markers. It is apparent that applying the uneven sampling
decreases the spectral index of the periodogram.

5.4   SEARCH FOR PERIODICITY

The LSPs of the nightly binned light curves of the Markarians shown in Figure 5.7
exhibit a variety of peaks, as is expected for a periodogram. To investigate if any
peak is significantly larger than a stochastic process would explain for, the confidence
limits of the LS powers for each trial frequency have to be calculated. Unlike for the
classical periodogram, however, Equation 5.4 cannot be used in this case, as the χ_2^2
distribution of LS powers only holds for white noise processes in the case of uneven
sampling. Instead, to assess the significance of peaks in the LSPs, a set of artificial light
curves is simulated. The light curves represent the null hypothesis: The processes in the
Markarians are stochastic and have no underlying periodic component. By generating
light curves with the same uneven sampling pattern as the FACT observations, the
influence of the red noise processes and the spectral window on the LSP is characterized.
The significance of peaks in the periodogram will then be investigated by looking at
the distribution of the LS powers of the simulated light curves at each frequency.

The method to simulate artificial light curves with a given spectral index is described
in Timmer and König (1995). Random light curves are simulated by generating a
Fourier transform where both the phase and the amplitudes of the Fourier components
are drawn from Gaussian distributions. However, the resulting light curves exhibit a

Gaussian distribution of fluxes. As mentioned in Chapter 2, the flux distribution of light curves from AGN are better described by log-normal distributions. Emmanoulopoulos et al. (2013) therefore combined the method by Timmer and König (1995) with an amplitude adjustment algorithm proposed by Schreiber and Schmitz (1996) to a method capable of generating artificial light curves providing both the fitted PSD and PDF of the original light curve.

The power-law fit functions shown in Figure 5.7 and the fluxes of the FACT sample light curves are passed to the simulation algorithm. The distribution of the fluxes is fit with mixed distribution of a gamma distribution $\Gamma(\kappa, \theta)$ and a log-normal distribution $\ln \mathcal{N}(\mu, \sigma^2)$, both with different weights,

$$f_{\mathrm{mix}}(x; \gamma) = w_\Gamma \frac{\theta^{-\kappa} \mathrm{e}^{-x/\theta} x^{\kappa-1}}{\Gamma(\kappa)} + w_{\ln \mathcal{N}} \frac{\mathrm{e}^{-(\ln x - \mu)^2/(2\sigma^2)}}{\sqrt{2\pi} x \sigma}, \tag{5.18}$$

following the notation of Emmanoulopoulos et al. (2013). Here, $\gamma = \{\kappa, \theta, \mu, \sigma, w_\Gamma\}$ are the shape and scale parameters of the gamma distribution, the mean and variance of the logarithm of the flux and the weight of the gamma distribution respectively. Furthermore, $w_{\ln \mathcal{N}} = 1 - w_\Gamma$. Figure 5.10 shows the fits of this mixture distribution to the flux distribution of the FACT light curves of Mrk 501 and Mrk 421. The fit parameters acquired with a log-likelihood approach are given in Table A.1. A `python` implementation of the simulation routine is provided by Connolly (2016)[6].
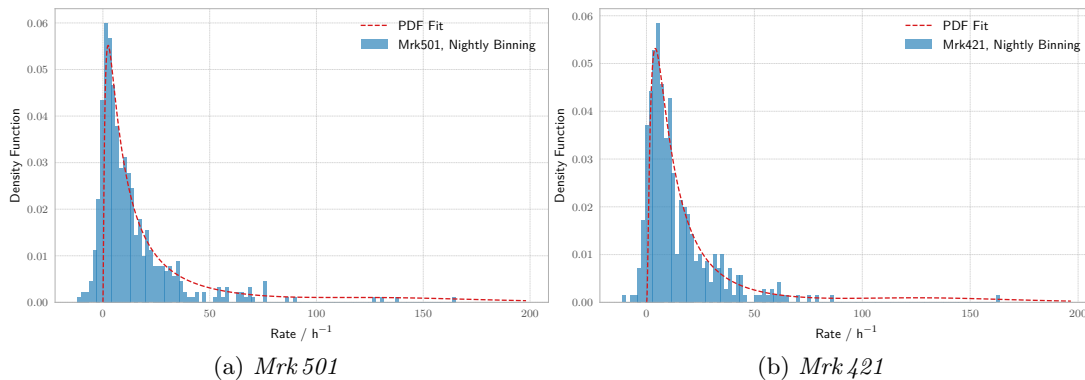

(a) *Mrk 501*   (b) *Mrk 421*

Figure 5.10 *Distribution of Rates of FACT Light Curves and Fitted Mixed Distribution* The blue histograms show the distribution of rates of the FACT light curves of the Markarians. The red lines show the best fits of the mixture distribution given in Equation 5.18.

For both nightly binned light curves of Mrk 501 and Mrk 421, 10 000 light curves are simulated each. In a first step, the generated light curves are 1 000 times longer than the FACT light curves to simulate the red noise leakage. A random interval of 1 500 evenly spaced data points is then cut out from the extended light curves. Low-frequency components will affect the generated light curve in the same way as the red-noise leakage in the actual data. The 1 500 remaining data points cover the whole observation range of about 5 years for both sources. The uneven sampling is then achieved by effectively multiplying with the window function of each sample light curve: For each timestamp of the FACT observations, the data point closest in time

---

6 https://github.com/samconnolly/DELightcurveSimulation

of the generated light curve is kept. The rest of the light curve is discarded. This
leaves exactly as many data points in the surrogate light curve as in the FACT light
curve. However, the simulated data points are still on an evenly-spaced grid. Therefore,
the timestamps of the generated light curves are replaced by the FACT timestamps.
In this process,the simulated fluxes are shifted by up to 0.25 days. This error has
to be introduced as simulating a denser grid of fluxes would be too computationally
expensive. Finally, each data point is given a random Poisson error, which is drawn
from the Poisson errors of each FACT sample light curve and the LSP is calculated.
Figure 5.11 shows a random light curve generated for the samples of Mrk 501 and
Mrk 421 each.

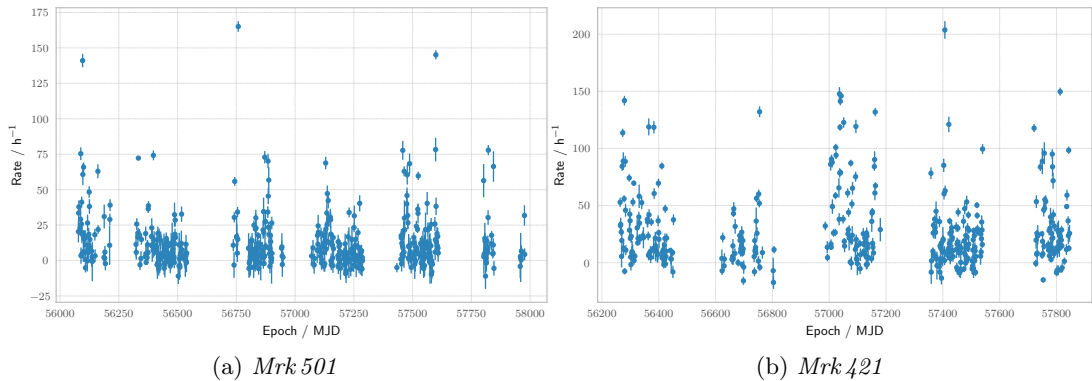

(a) *Mrk 501*   (b) *Mrk 421*

Figure 5.11 *Simulated Light Curves* Two random light curves simulated using the fitted PSD
and PDF of the FACT light curves.

Figure 5.12 shows a comparison between the power-law fits of the FACT peri-
odograms which was used to simulate the light curves and the averaged periodogram of
all 10 000 surrogates. It is apparent that the mean simulated periodograms are flatter
than the power-law fits. This is a caveat in the simulation: The simulated light curves
approximate the power-law periodogram in the even sampling case. Applying the FACT
observation pattern to the simulated light curves effectively introduces the windowing
and aliasing effects of the uneven sampling for a second time into the periodogram
of the simulated light curves, as discussed above for the simulation of the spectral
indices in Figure 5.9 and also shown in Figure 5.4. The difference between the mean
simulated periodogram and the power-law fit will have to be regarded when evaluating
the periodogram, as they can lead to over- or underestimation of significances.

Using the percentiles of the distribution of the LS powers for each frequency bin
in the LSPs of the surrogate light curves, the confidence limits of the periodogram
peaks are calculated. Even though the average simulated periodograms overestimate
the variability at large frequencies and underestimate it at small frequencies, the sig-
nificances are still calculated from the unevenly sampled surrogate light curves as the
distribution of the LS powers reflects the distribution for the FACT periodograms. Fig-
ure 5.13 depicts the FACT LSP, the averaged simulated LSP, and the 99% and 99.9%
tail probabilities for each trial frequency in the periodograms of both sources.

In both periodograms, the most prominent peaks around 100 and 300 days are
within the 99% confidence limit. However, the shown tail probabilities are single-trial
probabilities, meaning that the statistical penalty by the Look-elsewhere effect has not

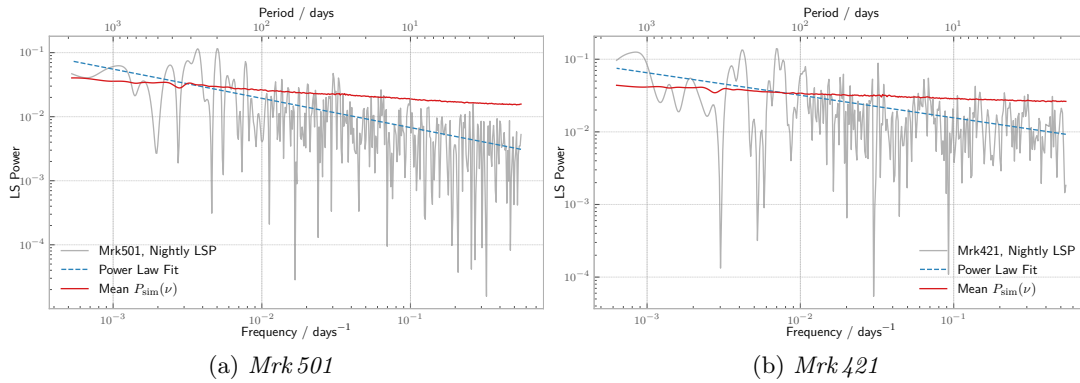(a) *Mrk 501*   (b) *Mrk 421*

Figure 5.12 *Comparison of Power-Law Fit of LSP and mean, simulated Periodogram* The LSPs of the FACT data are shown in grey with the corresponding power-law fits shown in blue. These power-laws are passed to the simulation algorithm, which then simulates *evenly* spaced light curves following this PSD. However, applying the FACT sampling to the simulated light curves flattens the spectrum, shown by the average of the 10 000 simulated periodograms (red line).

been applied yet. In order to account for the number of trial frequencies, the quantile corresponding to $X\%$ confidence would be given by the $(100 - X)/N_{\mathrm{ind}}$ quantile, where N_{ind} is the number of independent frequencies in the periodogram which is assumed to be equal to the number of data points. The required number of simulations would therefore increase by a factor of about 500 to 5×10^6, which is outside the time frame of this project but can be achieved in future work.

As accounting for the number of trial frequencies would increase the 99% significance limit, the prominent peaks in both periodograms cannot be ruled significant. Furthermore, the long-term variability components around 1 000 days for both sources will give rise to alias peaks in the region of 200 to 300 days in the periodogram, due to the strong peak at one sidereal year in the respective spectral windows. This can be observed in the tail probabilities shown in Figure 5.13 as dashed, orange lines. Especially the 99.9% limits have bumps in this region, showing that these frequencies have larger outliers than the neighbouring frequencies.

At larger frequencies, there are no significant peaks observable, even accounting for the fact that the averaged periodogram overestimates the fitted periodogram power in this regime, refer to Figure 5.12. The periodograms are compatible with the null hypothesis of a stochastic signal without underlying periodicity.
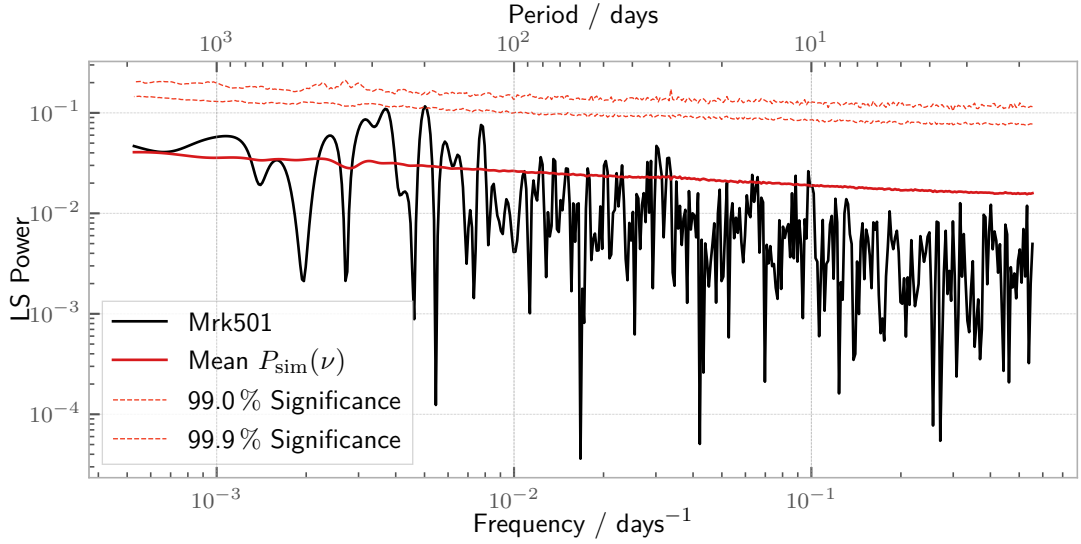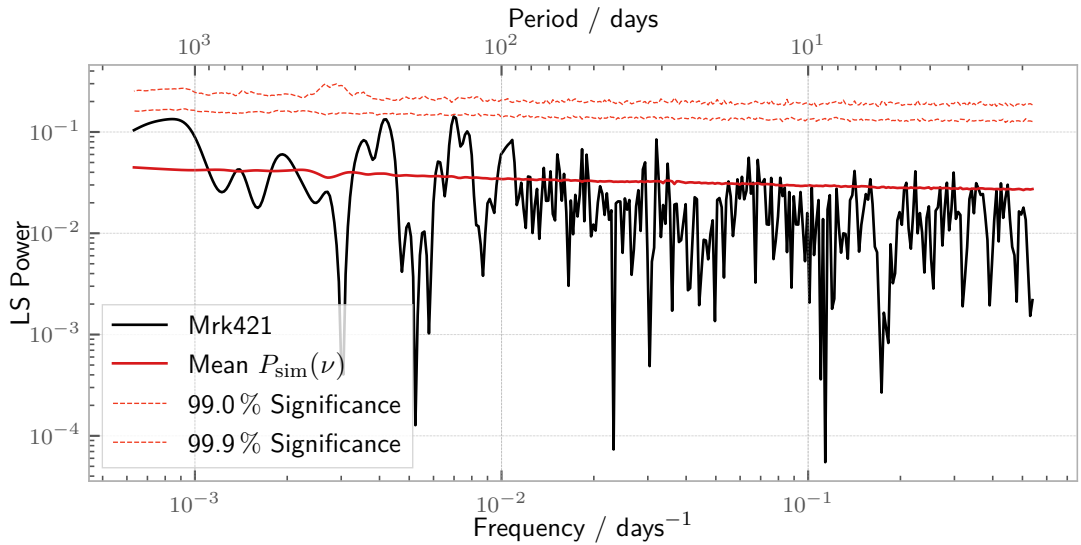
(a) *Mrk 501*

(b) *Mrk 421*

Figure 5.13 *Significance of LSP Peaks of Markarians* The FACT LSP of the Mrk 501 (top) and
Mrk 421 (bottom) is shown in black. The red line is the averaged periodogram of
the 10 000 surrogate light curves. The dashed, orange lines show the 99% and 99.9%
significance lines using single-trial probabilities. Both periodograms are consistent
with stochastic processes without underlying periodicity.

5.5 CONCLUSION

The LSPs of Mrk 501 and Mrk 421 have flat spectra, with spectral indices in the range
of $\alpha \sim 0.5 - 0.7$. These numbers are affected by the uneven sampling pattern, in a way
that they can be given as lower limits of the actual spectral index of the PSD. In order
to derive a more precise estimate, simulation studies can be performed, comparing the
periodograms of evenly- and unevenly sampled light curves. These simulations suggest

that the underlying PSDs are flicker noise processes with $\alpha \approx 1$, in agreement with observations of blazars by other experiments.

The LSPs of the Markarians' data are consistent with stochastic processes without underlying periodicity. Both periodograms hint more towards long-term periodicity with periods between 100 an 300 days than short-term periodicity, but no conclusive statement can be made on whether or not the sources are periodic. For the periodogram of Mrk 501, there is no trace of a 23-day periodicity as has been claimed previously, refer to Chapter 2. A binary black hole scenario is therefore not supported by the FACT observations.

CONCLUSION AND OUTLOOK

6.1 CONCLUSION

Active galactic nuclei are cosmic laboratories for high-energy physical phenomena. Their spectral energy densities and variability on short and large time-scales underline the complexity of the inherent processes. While theories predict periodic modulations of the VHE γ-ray emission, e.g. for binary black hole scenarios, observations lack the statistical significance to claim discoveries. The stochastic nature of the intrinsic source mechanisms requires high confidence limits.

Long-term, frequent, and multi-wavelength observation campaigns of blazars are the key to gain insights into the interplay of the black holes, radio jets, and accretion disks. The First G-APD Cherenkov Telescope is dedicated to the long-term monitoring of the brightest blazars in the night sky. The use of silicon photomultipliers allows for observations even during a bright night-sky background. The location on La Palma offers observations of Mrk 501, Mrk 421, and the Crab Nebula under low zenith angles, ensuring that the observed Cherenkov light is only minimally affected by absorption in the atmosphere.

The observed γ-ray rates show a large dependence on the zenith angle. Using basic assumptions from the Heitler model, this dependency can be expressed in a heuristic model function with three parameters. The application of this model to the proton rate measured by FACT is used to identify bad-weather observation runs, which are then excluded from the analysis. In addition, fitting the excess γ-ray rate in dependence of the zenith angle of the Crab Nebula allows for the correction of the zenith angle dependence in the data of the Markarians.

In order to characterise the variability of Mrk 501 and Mrk 421, a Lomb-Scargle periodogram analysis is performed. Periodograms of stochastic processes are subject to large scattering in their powers. Furthermore, the spectral window of the uneven sampling affects both the peak heights and the overall shape of the periodogram. The LSPs of Mrk 501 and Mrk 421 correspond to flicker noise processes (spectral index $\alpha \approx 1$) after accounting for the uneven sampling. As the statistical behaviour of the Lomb-Scargle periodogram can only be derived analytically for white-noise processes, Monte Carlo simulations are required to quantify the significance of peaks in the periodogram. For both Mrk 501 and Mrk 421, no hint for a periodicity on time-scales of days to years has been found in the 5-year light curves acquired with FACT.

6.1.1 *Caveats and Pitfalls of the LSP Analysis*

The Lomb-Scargle periodogram provides the mathematical framework for spectral analysis of unevenly sampled data required in many fields, such as astronomy and astrophysics. In the case of periodic variable stars, it has been applied with great success (Kim et al. 2014). The simple statistical behaviour of the powers in case of white-noise

processes and the equivalence of the least-square spectral analysis approach make it a method which is easy to implement and apply.

However, the underlying white-noise assumption is a large restriction. Especially complex source like AGN show red-noise behaviour, which has to be accounted for in the periodogram by means of simulations. Sophisticated simulations require a model function of the inherent processes. This increases the required workload and understanding of the sources significantly.

Even in the case of white-noise, the correlation of the powers at different frequencies is complicated due to the uneven sampling. The spectral window has to be studied in detail in order to identify alias peaks in the periodogram.

The periodic process has to be stable over range of observations in order to give rise to a significant peak. This is another big restriction on the nature of the physical processes that can be detected with the Lomb-Scargle periodogram. Dividing the light curves into yearly, monthly, weekly components is a mean to identify periodicity on shorter time scales and changes in the source. However, the inherent non-determinism of the processes has to be kept in mind.

6.2 OUTLOOK

6.2.1 *Improvements of Data Pipeline*

Future improvements of this data selection pipeline could aim at the approximations made by the Heitler model, which was used to derive the zenith angle model function. Greisen (1960) derived a parametrization of CR showers which yields more accurate results than the Heitler model. Furthermore, the approximation of an isothermal atmosphere has a large impact on the model function and could be more accurately treated by e.g. including the dependency of the refractive index n on the height / density of the atmosphere.

A more detailed treatment of the threshold dependence of the excess events rate could further improve data quality.

6.2.2 *Future Work using the LSP*

In order to take full advantage of the rich data set that the FACT observations provide, they can be split up into single years and months and searched for periodicity on smaller time scales. Intrinsic changes of the sources over the observed periods could be revealed. However, this analysis requires a thorough treatment of the changes in the telescope system over the years. Any change in the system can reflect in the data and lead to false conclusions. Nevertheless, it is an analysis which promises interesting results.

In addition, the analysis can be extended to other sources that FACT observes regularly, such as 1ES 1959+650, 1ES 2344+51.4, and 1H0323+342. A combination with (publicly available) data from other IACTs or multi-wavelength analysis with optical or X-ray instruments can also yield highly interesting results and constraints on model parameters.

Furthermore, simulation studies to investigate the effect of the spectral window on the periodogram can be performed. By quantifying this effect, the spectral index of

the PSD of the sources can be recovered. This requires a model of the source PSD, which is then used to simulate evenly spaced light curves. After applying the FACT window function, the similarity between the simulated periodogram and the FACT periodogram has to be quantified by a distance metric.

An essential condition for these analyses is the improvement of the simulation algorithm. Using the algorithm by Emmanoulopoulos et al. (2013), the fitted PSDs and PDFs of the sample light curves can be reproduced with the surrogate data sets. However, the application of the FACT window function on the simulated light curves changes the slope of the mean simulated periodogram. Whether this second application of the uneven sampling is avoidable using the Emmanoulopoulos et al. (2013) method will have to be investigated. Following an improvement of the simulations, a next requirement is the computation of a large ($\geq 10^6$) sample of artificial light curves.

6.2.3 *Towards continuous Coverage - M@TE Project*

As outlined in Chapter 2, variability on short time scales implies that the emission region is small. For AGN, short-term variability is generated in the jet or at the interface of the black hole and the accretion disk. To observe these central regions, continuous monitoring is essential. The M@TE[1] project is a FACT-like telescope planned to be built in San Pedro Matír, Mexico. Like FACT, it will be built using a former HEGRA telescope mount. The design close to FACT's will save development time and effort. The camera is planned to contain the next generation silicon photomultipliers (Dorner et al. 2016; Alfaro et al. 2017).

The location in San Pedro Matír is about 6 hours off-set from FACT on La Palma in longitude. Figure 6.1 shows the combined field-of-view of both telescopes in right ascension and declination using the same Mollweide projection as in Figure 3.2. In principle, sources like Mrk 501 and Mrk 421 will always be visible from either the FACT or the M@TE site. In practice, limits on the zenith angle give a maximum of six hour observation time for one source from one site per night. The FACT and M@TE telescopes can therefore combine the continuous coverage to 12 hours a day. The coordinates of the zeniths of the telescopes are indicated by the dashed lines. As the telescopes are within 4 degrees of latitude, sources will culminate at similar zenith angles, making the measured rates comparable.

---

1 Monitoring at TeV energies
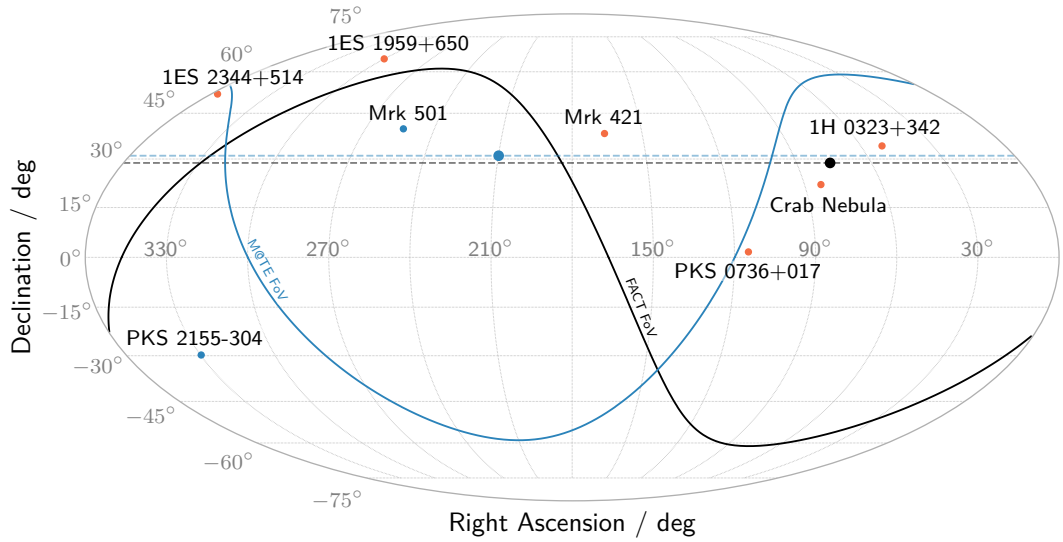
Figure 6.1 *The joint Sky Coverage of FACT and M@TE* The night sky is shown using the equal-area Mollweide projection. The black line marks the FACT field-of-view, the blue line is the prospected field-of-view of the M@TE telescope. The telescopes sites are within 4 degrees of latitude, which means that their zeniths cover similar declinations (black and blue dashed lines respectively). The orange circles mark sources that FACT observes frequently.

The combined light curves from FACT and M@TE promise great insights into the inner workings of blazars.
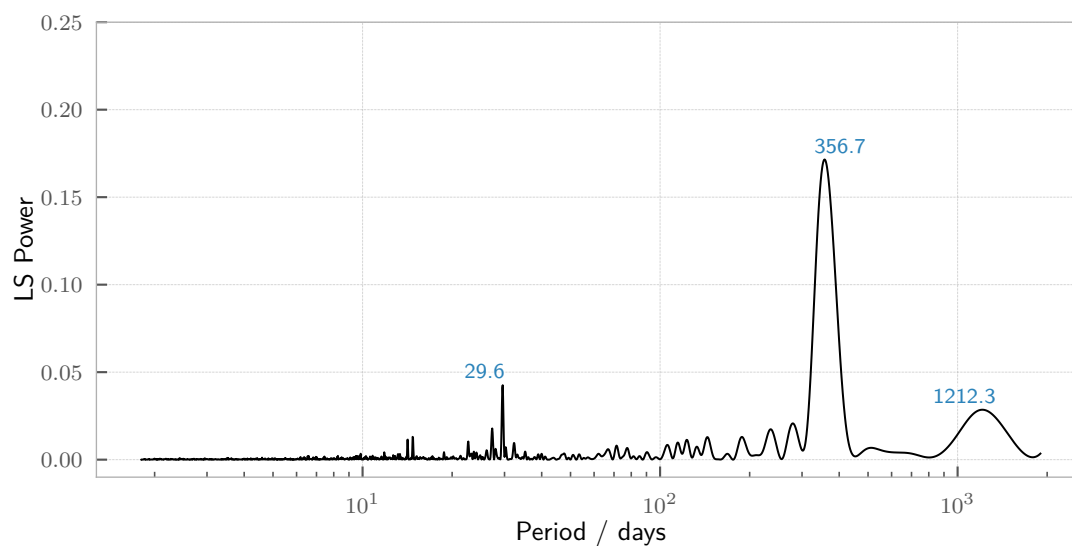
Figure A.1 *Spectral Window of FACT Mrk 501 Observations.*
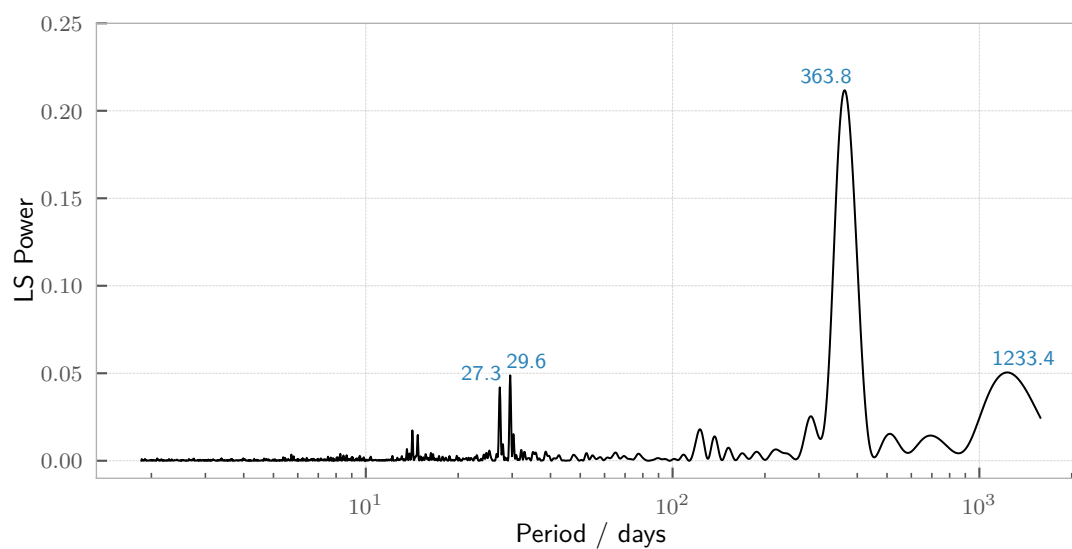
Figure A.2 *Spectral Window of FACT Mrk 421 Observations.*

A

ADDITIONAL FIGURES

65
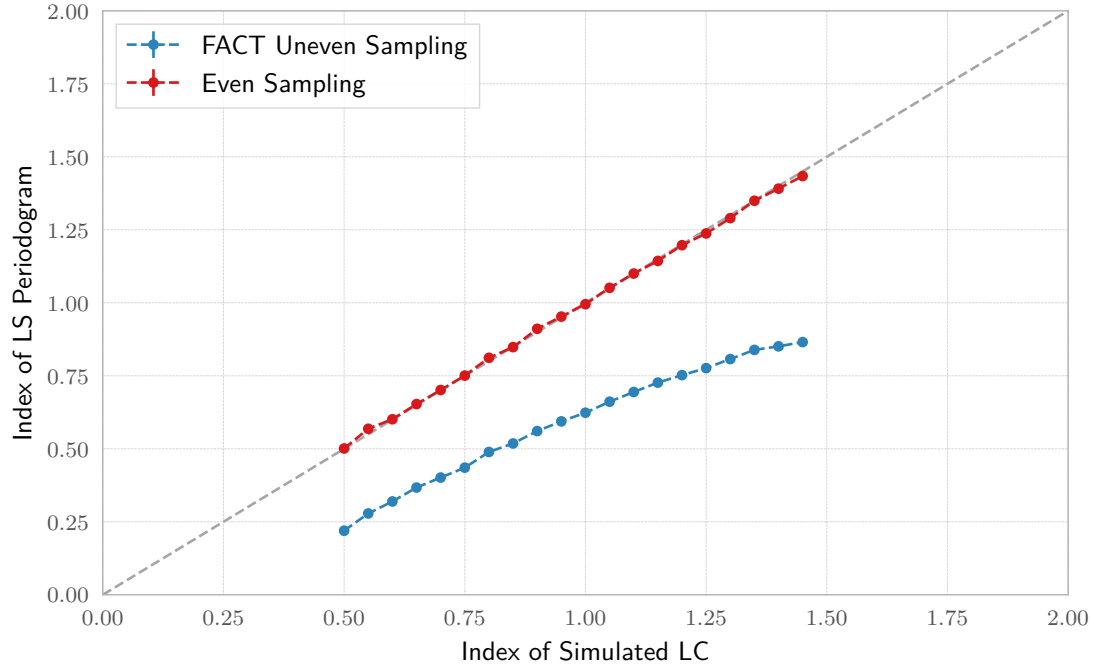
Figure A.3 *Comparison of simulated spectral index and spectral index of LSP* Mrk501

Table A.1 *PDF Fit Parameters:* Parameters of the FACT nightly light curves PDF fits with function Equation 5.18.

	Mrk 501	Mrk 421
κ	15.3	15.1
θ	9.63	9.3
w_Γ	0.09	0.11
$\exp(\ln\mu)$	1.25	1.0
$\ln\sigma$	11.88	11.5
$w_{\ln\mathcal{N}}$	0.91	0.89

B

REPRODUCIBLE RESEARCH

The required `python` packages and the versions used:

python	3.6.2	astropy	2.0.2	scipy	0.19.1
pandas	0.20.3	numpy	1.13.1	peewee	2.10.1
matplotlib	2.0.2	stingray	0.1.dev	pyfact	0.12.1
astroML	0.3	astroML_addons	0.2.2	seaborn	0.8.1
ephem	3.7.6.0				

The `DELCgen` module by Connolly (2016) for the simulation of the light curves can be acquired from https://github.com/samconnolly/DELightcurveSimulation. Note that the code is written in `python` 2 and will have to be ported to `python` 3. Furthermore, the `EmmanLC()` method has to be adapted to allow for variable output data length when passing a light curve to the simulation method.

Table B.1 lists the `python` scripts used to create the figures for the different chapters. The codes require scripts from the `peripylib/` directory, which can be added to the `python` path using

```
export PYTHONPATH="$PYTHONPATH:path/to/peripylib"
```

In principle, all code can be run using

```
python path/to/script.py
```

However, some scripts require access to the FACT database, which is granted if the current FACT password is set as the `FACT_PASSWORD` shell environment variable.

The `peripylib` package provided in the repository provides the data pipeline described in Chapter 4. The `query_fact` module contains the `query_fact()`-method which is meant as the only required interface for the following analyses. The method returns both the nightly-binned and the run data of the requested source, after applying the cuts and corrections outlined in Chapter 4.

All figures are created using the `peripylib/figures.py` script for a uniform look. This dependency can be removed by simply replacing the lines creating and saving the figures with the corresponding `matplotlib` commands.

Table B.1 *Overview of archived code* The code to reproduce the analysis of this thesis can be found at `https://git.rwth-aachen.de/tbretz/fact/tree/master/mahlke2017`. The directory column list the subdirectories starting at `mahlke2017/`. A check mark in the FACT PW column means that the code will require the `FACT_PASSWORD` shell environment variable to contain the current FACT password. The figures column states the figures of this thesis created with this code.

Directory	Filename	FACT PW	Figures
`Chapter2/`	`tev_sky.py`		2.1
`Chapter2/`	`pks_flux_hess.py`		2.5
`Chapter3/`	`fact_fov.py`		3.2
`Chapter3/`	`whipple_mrk421.py`		3.3
`Chapter4/`	`cr_rates.py`	✓	4.2, 4.3, 4.4, 4.5, 4.6
`Chapter4/`	`gamma_rates.py`	✓	4.7
`Chapter4/`	`th_corr.py`	✓	4.9
`Chapter5/`	`psd_examples.py`		5.1
`Chapter5/`	`peri_scat.py`		5.2
`Chapter5/`	`spectral_windows.py`	✓	5.3, 5.4, A.1, A.2
`Chapter5/`	`sunspots.py`		5.5
`Chapter5/`	`fact_lcs.py`	✓	5.6
`Chapter5/`	`ls_significance.py`	✓	5.7, 5.8, 5.10, 5.11, 5.12, 5.12, 5.13
`Chapter5/`	`spec_sim.py`	✓	5.9, A.3
`Chapter6/`	`fact_mate_fov.py`		6.1

Abdo, A. A., Ackermann, M., Agudo, I., Ajello, M., Aller, H. D., Aller, M. F., Angelakis, E., Arkharov, A. A., Axelsson, M., Bach, U., and et al. (2010). The Spectral Energy Distribution of Fermi Bright Blazars. *The Astrophysical Journal*, 716:30–70.

Abdo, A. A., Ackermann, M., Ajello, M., Allafort, A., Baldini, L., Ballet, J., Barbiellini, G., Bastieri, D., Bechtol, K., Bellazzini, R., Berenji, B., Blandford, R. D., Bloom, E. D., Bonamente, E., Borgland, A. W., Bouvier, A., Brandt, T. J., Bregeon, J., Brez, A., Brigida, M., Bruel, P., Buehler, R., Buson, S., Caliandro, G. A., Cameron, R. A., Cannon, A., Caraveo, P. A., Casandjian, J. M., Çelik, Ö., Charles, E., Chekhtman, A., Cheung, C. C., Chiang, J., Ciprini, S., Claus, R., Cohen-Tanugi, J., Costamante, L., Cutini, S., D'Ammando, F., Dermer, C. D., de Angelis, A., de Luca, A., de Palma, F., Digel, S. W., do Couto e Silva, E., Drell, P. S., Drlica-Wagner, A., Dubois, R., Dumora, D., Favuzzi, C., Fegan, S. J., Ferrara, E. C., Focke, W. B., Fortin, P., Frailis, M., Fukazawa, Y., Funk, S., Fusco, P., Gargano, F., Gasparrini, D., Gehrels, N., Germani, S., Giglietto, N., Giordano, F., Giroletti, M., Glanzman, T., Godfrey, G., Grenier, I. A., Grondin, M.-H., Grove, J. E., Guiriec, S., Hadasch, D., Hanabata, Y., Harding, A. K., Hayashi, K., Hayashida, M., Hays, E., Horan, D., Itoh, R., Jóhannesson, G., Johnson, A. S., Johnson, T. J., Khangulyan, D., Kamae, T., Katagiri, H., Kataoka, J., Kerr, M., Knödlseder, J., Kuss, M., Lande, J., Latronico, L., Lee, S.-H., Lemoine-Goumard, M., Longo, F., Loparco, F., Lubrano, P., Madejski, G. M., Makeev, A., Marelli, M., Mazziotta, M. N., McEnery, J. E., Michelson, P. F., Mitthumsiri, W., Mizuno, T., Moiseev, A. A., Monte, C., Monzani, M. E., Morselli, A., Moskalenko, I. V., Murgia, S., Nakamori, T., Naumann-Godo, M., Nolan, P. L., Norris, J. P., Nuss, E., Ohsugi, T., Okumura, A., Omodei, N., Ormes, J. F., Ozaki, M., Paneque, D., Parent, D., Pelassa, V., Pepe, M., Pesce-Rollins, M., Pierbattista, M., Piron, F., Porter, T. A., Rainò, S., Rando, R., Ray, P. S., Razzano, M., Reimer, A., Reimer, O., Reposeur, T., Ritz, S., Romani, R. W., Sadrozinski, H. F.-W., Sanchez, D., Parkinson, P. M. S., Scargle, J. D., Schalk, T. L., Sgrò, C., Siskind, E. J., Smith, P. D., Spandre, G., Spinelli, P., Strickman, M. S., Suson, D. J., Takahashi, H., Takahashi, T., Tanaka, T., Thayer, J. B., Thompson, D. J., Tibaldo, L., Torres, D. F., Tosti, G., Tramacere, A., Troja, E., Uchiyama, Y., Vandenbroucke, J., Vasileiou, V., Vianello, G., Vitale, V., Wang, P., Wood, K. S., Yang, Z., and Ziegler, M. (2011a). Gamma-Ray Flares from the Crab Nebula. *Science*, 331:739.

Abdo, A. A., Ackermann, M., Ajello, M., Baldini, L., Ballet, J., Barbiellini, G., Bastieri, D., Bechtol, K., Bellazzini, R., Berenji, B., and et al. (2011b). Fermi Large Area Telescope Observations of Markarian 421: The Missing Piece of its Spectral Energy Distribution. *The Astrophysical Journal*, 736:131.

Acciari, V. A., Arlen, T., Aune, T., Benbow, W., Bird, R., Bouvier, A., Bradbury, S. M., Buckley, J. H., Bugaev, V., de la Calle Perez, I., Carter-Lewis, D. A., Cesarini, A., Ciupik, L., Collins-Hughes, E., Connolly, M. P., Cui, W., Duke, C., Dumm, J., Falcone, A., Federici, S., Fegan, D. J., Fegan, S. J., Finley, J. P., Finnegan, G.,

Fortson, L., Gaidos, J., Galante, N., Gall, D., Gibbs, K., Gillanders, G. H., Griffin, S., Grube, J., Gyuk, G., Hanna, D., Horan, D., Humensky, T. B., Kaaret, P., Kertzman, M., Khassen, Y., Kieda, D., Krawczynski, H., Krennrich, F., Lang, M. J., McEnery, J. E., Madhavan, A. S., Moriarty, P., Nelson, T., O'Faoláin de Bhróithe, A., Ong, R. A., Orr, M., Otte, A. N., Perkins, J. S., Petry, D., Pichel, A., Pohl, M., Quinn, J., Ragan, K., Reynolds, T., Roache, E., Rovero, A., Schroedter, M., Sembroski, G. H., Smith, A., Telezhinsky, I., Theiling, M., Toner, J., Tyler, J., Varlotta, A., Vivier, M., Wakely, S. P., Ward, J. E., Weekes, T. C., Weinstein, A., Welsing, R., Williams, D. A., and Wissel, S. (2014). Observation of Markarian 421 in TeV gamma rays over a 14-year time span. *Astroparticle Physics*, 54:1–10.

Ackermann, M., Ajello, M., Albert, A., Atwood, W. B., Baldini, L., Ballet, J., Barbiellini, G., Bastieri, D., Becerra González, J., Bellazzini, R., Bissaldi, E., Blandford, R. D., Bloom, E. D., Bonino, R., Bottacini, E., Bregeon, J., Bruel, P., Buehler, R., Buson, S., Caliandro, G. A., Cameron, R. A., Caputo, R., Caragiulo, M., Caraveo, P. A., Cavazzuti, E., Cecchi, C., Chekhtman, A., Chiang, J., Chiaro, G., Ciprini, S., Cohen-Tanugi, J., Conrad, J., Cutini, S., D'Ammando, F., De Angelis, A., de Palma, F., Desiante, R., Di Venere, L., Domínguez, A., Drell, P. S., Favuzzi, C., Fegan, S. J., Ferrara, E. C., Focke, W. B., Fuhrmann, L., Fukazawa, Y., Fusco, P., Gargano, F., Gasparrini, D., Giglietto, N., Giommi, P., Giordano, F., Giroletti, M., Godfrey, G., Green, D., Grenier, I. A., Grove, J. E., Guiriec, S., Harding, A. K., Hays, E., Hewitt, J. W., Hill, A. B., Horan, D., Jogler, T., Jóhannesson, G., Johnson, A. S., Kamae, T., Kuss, M., Larsson, S., Latronico, L., Li, J., Li, L., Longo, F., Loparco, F., Lott, B., Lovellette, M. N., Lubrano, P., Magill, J., Maldera, S., Manfreda, A., Max-Moerbeck, W., Mayer, M., Mazziotta, M. N., McEnery, J. E., Michelson, P. F., Mizuno, T., Monzani, M. E., Morselli, A., Moskalenko, I. V., Murgia, S., Nuss, E., Ohno, M., Ohsugi, T., Ojha, R., Omodei, N., Orlando, E., Ormes, J. F., Paneque, D., Pearson, T. J., Perkins, J. S., Perri, M., Pesce-Rollins, M., Petrosian, V., Piron, F., Pivato, G., Porter, T. A., Rainò, S., Rando, R., Razzano, M., Readhead, A., Reimer, A., Reimer, O., Schulz, A., Sgrò, C., Siskind, E. J., Spada, F., Spandre, G., Spinelli, P., Suson, D. J., Takahashi, H., Thayer, J. B., Thompson, D. J., Tibaldo, L., Torres, D. F., Tosti, G., Troja, E., Uchiyama, Y., Vianello, G., Wood, K. S., Wood, M., Zimmer, S., Berdyugin, A., Corbet, R. H. D., Hovatta, T., Lindfors, E., Nilsson, K., Reinthal, R., Sillanpää, A., Stamerra, A., Takalo, L. O., and Valtonen, M. J. (2015). Multiwavelength Evidence for Quasi-periodic Modulation in the Gamma-Ray Blazar PG 1553+113. *The Astrophysical Journal Letters*, 813(2):L41.

Aharonian, F., Akhperjanian, A. G., Bazer-Bachi, A. R., Behera, B., Beilicke, M., Benbow, W., Berge, D., Bernlöhr, K., Boisson, C., Bolz, O., Borrel, V., Boutelier, T., Braun, I., Brion, E., Brown, A. M., Bühler, R., Büsching, I., Bulik, T., Carrigan, S., Chadwick, P. M., Clapson, A. C., Chounet, L.-M., Coignet, G., Cornils, R., Costamante, L., Degrange, B., Dickinson, H. J., Djannati-Ataï, A., Domainko, W., Drury, L. O., Dubus, G., Dyks, J., Egberts, K., Emmanoulopoulos, D., Espigat, P., Farnier, C., Feinstein, F., Fiasson, A., Förster, A., Fontaine, G., Funk, S., Funk, S., Füßling, M., Gallant, Y. A., Giebels, B., Glicenstein, J. F., Glück, B., Goret, P., Hadjichristidis, C., Hauser, D., Hauser, M., Heinzelmann, G., Henri, G., Hermann, G., Hinton, J. A., Hoffmann, A., Hofmann, W., Holleran, M., Hoppe, S., Horns, D., Jacholkowska,

A., de Jager, O. C., Kendziorra, E., Kerschhaggl, M., Khélifi, B., Komin, N., Kosack, K., Lamanna, G., Latham, I. J., Le Gallou, R., Lemière, A., Lemoine-Goumard, M., Lenain, J.-P., Lohse, T., Martin, J. M., Martineau-Huynh, O., Marcowith, A., Masterson, C., Maurin, G., McComb, T. J. L., Moderski, R., Moulin, E., de Naurois, M., Nedbal, D., Nolan, S. J., Olive, J.-P., Orford, K. J., Osborne, J. L., Ostrowski, M., Panter, M., Pedaletti, G., Pelletier, G., Petrucci, P.-O., Pita, S., Pühlhofer, G., Punch, M., Ranchon, S., Raubenheimer, B. C., Raue, M., Rayner, S. M., Renaud, M., Ripken, J., Rob, L., Rolland, L., Rosier-Lees, S., Rowell, G., Rudak, B., Ruppel, J., Sahakian, V., Santangelo, A., Saugé, L., Schlenker, S., Schlickeiser, R., Schröder, R., Schwanke, U., Schwarzburg, S., Schwemmer, S., Shalchi, A., Sol, H., Spangler, D., Stawarz, Ł., Steenkamp, R., Stegmann, C., Superina, G., Tam, P. H., Tavernet, J.-P., Terrier, R., van Eldik, C., Vasileiadis, G., Venter, C., Vialle, J. P., Vincent, P., Vivier, M., Völk, H. J., Volpe, F., Wagner, S. J., Ward, M., and Zdziarski, A. A. (2007a). An Exceptional Very High Energy Gamma-Ray Flare of PKS 2155-304. *Astrophysical Journal*, 664:L71–L74.

Aharonian, F., Akhperjanian, A. G., Bazer-Bachi, A. R., Beilicke, M., Benbow, W., Berge, D., Bernlöhr, K., Boisson, C., Bolz, O., Borrel, V., Braun, I., Brion, E., Brown, A. M., Bühler, R., Büsching, I., Boutelier, T., Carrigan, S., Chadwick, P. M., Chounet, L.-M., Coignet, G., Cornils, R., Costamante, L., Degrange, B., Dickinson, H. J., Djannati-Ataï, A., Drury, L. O., Dubus, G., Egberts, K., Emmanoulopoulos, D., Espigat, P., Farnier, C., Feinstein, F., Ferrero, E., Fiasson, A., Fontaine, G., Funk, S., Funk, S., Füßling, M., Gallant, Y. A., Giebels, B., Glicenstein, J. F., Glück, B., Goret, P., Hadjichristidis, C., Hauser, D., Hauser, M., Heinzelmann, G., Henri, G., Hermann, G., Hinton, J. A., Hoffmann, A., Hofmann, W., Holleran, M., Hoppe, S., Horns, D., Jacholkowska, A., de Jager, O. C., Kendziorra, E., Kerschhaggl, M., Khélifi, B., Komin, N., Kosack, K., Lamanna, G., Latham, I. J., Le Gallou, R., Lemière, A., Lemoine-Goumard, M., Lohse, T., Martin, J. M., Martineau-Huynh, O., Marcowith, A., Masterson, C., Maurin, G., McComb, T. J. L., Moulin, E., de Naurois, M., Nedbal, D., Nolan, S. J., Noutsos, A., Olive, J.-P., Orford, K. J., Osborne, J. L., Panter, M., Pelletier, G., Petrucci, P.-O., Pita, S., Pühlhofer, G., Punch, M., Ranchon, S., Raubenheimer, B. C., Raue, M., Rayner, S. M., Reimer, A., Reimer, O., Ripken, J., Rob, L., Rolland, L., Rosier-Lees, S., Rowell, G., Sahakian, V., Santangelo, A., Saugé, L., Schlenker, S., Schlickeiser, R., Schröder, R., Schwanke, U., Schwarzburg, S., Schwemmer, S., Shalchi, A., Sol, H., Spangler, D., Spanier, F., Steenkamp, R., Stegmann, C., Superina, G., Tam, P. H., Tavernet, J.-P., Terrier, R., Tluczykont, M., van Eldik, C., Vasileiadis, G., Venter, C., Vialle, J. P., Vincent, P., Völk, H. J., Wagner, S. J., and Ward, M. (2007b). Detection of extended very-high-energy γ-ray emission towards the young stellar cluster Westerlund 2. *Astronomy and Astrophysics*, 467:1075–1080.

Aharonian, F., Akhperjanian, A. G., Bazer-Bachi, A. R., Beilicke, M., Benbow, W., Berge, D., Bernlöhr, K., Boisson, C., Bolz, O., Borrel, V., Braun, I., Brown, A. M., Bühler, R., Büsching, I., Carrigan, S., Chadwick, P. M., Chounet, L.-M., Cornils, R., Costamante, L., Degrange, B., Dickinson, H. J., Djannati-Ataï, A., O'C. Drury, L., Dubus, G., Egberts, K., Emmanoulopoulos, D., Espigat, P., Feinstein, F., Ferrero, E., Fiasson, A., Fontaine, G., Funk, S., Funk, S., Füßling, M., Gallant, Y. A.,

Giebels, B., Glicenstein, J. F., Goret, P., Hadjichristidis, C., Hauser, D., Hauser, M., Heinzelmann, G., Henri, G., Hermann, G., Hinton, J. A., Hoffmann, A., Hofmann, W., Holleran, M., Horns, D., Jacholkowska, A., de Jager, O. C., Kendziorra, E., Khélifi, B., Komin, N., Konopelko, A., Kosack, K., Latham, I. J., Le Gallou, R., Lemière, A., Lemoine-Goumard, M., Lohse, T., Martin, J. M., Martineau-Huynh, O., Marcowith, A., Masterson, C., Maurin, G., McComb, T. J. L., Moulin, E., de Naurois, M., Nedbal, D., Nolan, S. J., Noutsos, A., Orford, K. J., Osborne, J. L., Ouchrif, M., Panter, M., Pelletier, G., Pita, S., Pühlhofer, G., Punch, M., Raubenheimer, B. C., Raue, M., Rayner, S. M., Reimer, A., Reimer, O., Ripken, J., Rob, L., Rolland, L., Rowell, G., Sahakian, V., Santangelo, A., Saugé, L., Schlenker, S., Schlickeiser, R., Schröder, R., Schwanke, U., Schwarzburg, S., Shalchi, A., Sol, H., Spangler, D., Spanier, F., Steenkamp, R., Stegmann, C., Superina, G., Tavernet, J.-P., Terrier, R., Tluczykont, M., van Eldik, C., Vasileiadis, G., Venter, C., Vincent, P., Völk, H. J., Wagner, S. J., and Ward, M. (2006). 3.9 day orbital modulation in the TeV γ-ray flux and spectrum from the X-ray binary LS 5039. *Astronomy and Astrophysics*, 460:743–749.

Aharonian, F., Bykov, A., Parizot, E., Ptuskin, V., and Watson, A. (2011). Cosmic rays in galactic and extragalactic magnetic fields. *arXiv.org*, (1):97–132.

Ahnen, M. L., Ansoldi, S., Antonelli, L. A., Antoranz, P., Babic, A., Banerjee, B., Bangale, P., Barres de Almeida, U., Barrio, J. A., Becerra González, J., Bednarek, W., Bernardini, E., Biasuzzi, B., Biland, A., Blanch, O., Bonnefoy, S., Bonnoli, G., Borracci, F., Bretz, T., Buson, S., Carosi, A., Chatterjee, A., Clavero, R., Colin, P., Colombo, E., Contreras, J. L., Cortina, J., Covino, S., Da Vela, P., Dazzi, F., De Angelis, A., De Lotto, B., de Oña Wilhelmi, E., Di Pierro, F., Domínguez, A., Dominis Prester, D., Dorner, D., Doro, M., Einecke, S., Eisenacher Glawion, D., Elsaesser, D., Fernández-Barral, A., Fidalgo, D., Fonseca, M. V., Font, L., Frantzen, K., Fruck, C., Galindo, D., García López, R. J., Garczarczyk, M., Garrido Terrats, D., Gaug, M., Giammaria, P., Godinović, N., González Muñoz, A., Gora, D., Guberman, D., Hadasch, D., Hahn, A., Hanabata, Y., Hayashida, M., Herrera, J., Hose, J., Hrupec, D., Hughes, G., Idec, W., Kodani, K., Konno, Y., Kubo, H., Kushida, J., La Barbera, A., Lelas, D., Lindfors, E., Lombardi, S., Longo, F., López, M., López-Coto, R., Majumdar, P., Makariev, M., Mallot, K., Maneva, G., Manganaro, M., Mannheim, K., Maraschi, L., Marcote, B., Mariotti, M., Martínez, M., Mazin, D., Menzel, U., Miranda, J. M., Mirzoyan, R., Moralejo, A., Moretti, E., Nakajima, D., Neustroev, V., Niedzwiecki, A., Nievas Rosillo, M., Nilsson, K., Nishijima, K., Noda, K., Nogués, L., Orito, R., Overkemping, A., Paiano, S., Palacio, J., Palatiello, M., Paneque, D., Paoletti, R., Paredes, J. M., Paredes-Fortuny, X., Pedaletti, G., Perri, L., Persic, M., Poutanen, J., Prada Moroni, P. G., Prandini, E., Puljak, I., Rhode, W., Ribó, M., Rico, J., Rodriguez Garcia, J., Saito, T., Satalecka, K., Schultz, C., Schweizer, T., Shore, S. N., Sillanpää, A., Sitarek, J., Snidaric, I., Sobczynska, D., Stamerra, A., Steinbring, T., Strzys, M., Takalo, L., Takami, H., Tavecchio, F., Temnikov, P., Terzić, T., Tescaro, D., Teshima, M., Thaele, J., Torres, D. F., Toyama, T., Treves, A., Verguilov, V., Vovk, I., Ward, J. E., Will, M., Wu, M. H., and Zanin, R. (2016). Long-term multi-wavelength variability and correlation study of Markarian 421 from 2007 to 2009. *Astronomy and Astrophysics*, 593:A91.

Ahnen, M. L., Ansoldi, S., Antonelli, L. A., Arcaro, C., Babić, A., Banerjee, B., Bangale, P., Barres de Almeida, U., Barrio, J. A., Bednarek, W., Bernardini, E., Berti, A., Biasuzzi, B., Biland, A., Blanch, O., Bonnefoy, S., Bonnoli, G., Borracci, F., Bretz, T., Carosi, R., Carosi, A., Chatterjee, A., Colin, P., Colombo, E., Contreras, J. L., Cortina, J., Covino, S., Cumani, P., Da Vela, P., Dazzi, F., De Angelis, A., De Lotto, B., de Oña Wilhelmi, E., Di Pierro, F., Doert, M., Domínguez, A., Dominis Prester, D., Dorner, D., Doro, M., Einecke, S., Eisenacher Glawion, D., Elsaesser, D., Engelkemeier, M., Fallah Ramazani, V., Fernández-Barral, A., Fidalgo, D., Fonseca, M. V., Font, L., Fruck, C., Galindo, D., García López, R. J., Garczarczyk, M., Gaug, M., Giammaria, P., Godinović, N., Gora, D., Guberman, D., Hadasch, D., Hahn, A., Hassan, T., Hayashida, M., Herrera, J., Hose, J., Hrupec, D., Hughes, G., Ishio, K., Konno, Y., Kubo, H., Kushida, J., Kuveždić, D., Lelas, D., Lindfors, E., Lombardi, S., Longo, F., López, M., Majumdar, P., Makariev, M., Maneva, G., Manganaro, M., Mannheim, K., Maraschi, L., Mariotti, M., Martínez, M., Mazin, D., Menzel, U., Mirzoyan, R., Moralejo, A., Moretti, E., Nakajima, D., Neustroev, V., Niedzwiecki, A., Nievas Rosillo, M., Nilsson, K., Nishijima, K., Noda, K., Nogués, L., Paiano, S., Palacio, J., Palatiello, M., Paneque, D., Paoletti, R., Paredes, J. M., Paredes-Fortuny, X., Pedaletti, G., Peresano, M., Perri, L., Persic, M., Poutanen, J., Prada Moroni, P. G., Prandini, E., Puljak, I., Garcia, J. R., Reichardt, I., Rhode, W., Ribó, M., Rico, J., Saito, T., Satalecka, K., Schroeder, S., Schweizer, T., Shore, S. N., Sillanpää, A., Sitarek, J., Šnidarić, I., Sobczynska, D., Stamerra, A., Strzys, M., Surić, T., Takalo, L., Tavecchio, F., Temnikov, P., Terzić, T., Tescaro, D., Teshima, M., Torres, D. F., Torres-Albà, N., Toyama, T., Treves, A., Vanzo, G., Vazquez Acosta, M., Vovk, I., Ward, J. E., Will, M., Wu, M. H., Zarić, D., Desiante, R., Becerra González, J., D'Ammando, F., Larsson, S., Raiteri, C. M., Reinthal, R., Lähteenmäki, A., Järvelä, E., Tornikoski, M., Ramakrishnan, V., Jorstad, S. G., Marscher, A. P., Bala, V., MacDonald, N. R., Kaur, N., Sameer, Baliyan, K., Acosta-Pulido, J. A., Lazaro, C., Martí-nez-Lombilla, C., Grinon-Marin, A. B., Pastor Yabar, A., Protasio, C., Carnerero, M. I., Jermak, H., Steele, I. A., Larionov, V. M., Borman, G. A., and Grishina, T. S. (2017). Multiwavelength observations of a VHE gamma-ray flare from PKS 1510-089 in 2015. *Astronomy and Astrophyiscs*, 603:A29.

Albert, J., Aliu, E., Anderhub, H., Antoranz, P., Armada, A., Baixeras, C., Barrio, J. A., Bartko, H., Bastieri, D., Becker, J. K., Bednarek, W., Berger, K., Bigongiari, C., Biland, A., Bock, R. K., Bordas, P., Bosch-Ramon, V., Bretz, T., Britvitch, I., Camara, M., Carmona, E., Chilingarian, A., Coarasa, J. A., Commichau, S., Contreras, J. L., Cortina, J., Costado, M. T., Curtef, V., Danielyan, V., Dazzi, F., De Angelis, A., Delgado, C., de los Reyes, R., De Lotto, B., Domingo-Santamaría, E., Dorner, D., Doro, M., Errando, M., Fagiolini, M., Ferenc, D., Fernández, E., Firpo, R., Flix, J., Fonseca, M. V., Font, L., Fuchs, M., Galante, N., García-López, R. J., Garczarczyk, M., Gaug, M., Giller, M., Goebel, F., Hakobyan, D., Hayashida, M., Hengstebeck, T., Herrero, A., Höhne, D., Hose, J., Hrupec, D., Hsu, C. C., Jacon, P., Jogler, T., Kosyra, R., Kranich, D., Kritzer, R., Laille, A., Lindfors, E., Lombardi, S., Longo, F., López, J., López, M., Lorenz, E., Majumdar, P., Maneva, G., Mannheim, K., Mansutti, O., Mariotti, M., Martínez, M., Mazin, D., Merck, C., Meucci, M., Meyer, M., Miranda, J. M., Mirzoyan, R., Mizobuchi, S., Moralejo, A., Nieto, D., Nilsson, K., Ninkovic, J., Oña-Wilhelmi, E., Otte, N., Oya, I., Paneque,

D., Panniello, M., Paoletti, R., Paredes, J. M., Pasanen, M., Pascoli, D., Pauss, F., Pegna, R., Persic, M., Peruzzo, L., Piccioli, A., Prandini, E., Puchades, N., Raymers, A., Rhode, W., Ribó, M., Rico, J., Rissi, M., Robert, A., Rügamer, S., Saggion, A., Saito, T., Sánchez, A., Sartori, P., Scalzotto, V., Scapin, V., Schmitt, R., Schweizer, T., Shayduk, M., Shinozaki, K., Shore, S. N., Sidro, N., Sillanpää, A., Sobczynska, D., Stamerra, A., Stark, L. S., Takalo, L., Tavecchio, F., Temnikov, P., Tescaro, D., Teshima, M., Torres, D. F., Turini, N., Vankov, H., Vitale, V., Wagner, R. M., Wibig, T., Wittek, W., Zandanel, F., Zanin, R., and Zapatero, J. (2007). Variable Very High Energy γ-Ray Emission from Markarian 501. *The Astrophysical Journal*, 669:862–883.

Aleksić, Ansoldi, S, Antonelli, L A, Antoranz, P, Babic, A, Bangale, P, Barrio, J A, Becerra González, J, Bednarek, W, Bernardini, E, Biasuzzi, B, Biland, A, Blanch, O, Bonnefoy, S, Bonnoli, G, Borracci, F, Bretz, T, Carmona, E, Carosi, A, Colin, P, Colombo, E, Contreras, J L, Cortina, J, Covino, S, Da Vela, P, Dazzi, F, De Angelis, A, De Caneva, G, De Lotto, B, de Oña Wilhelmi, E, Delgado Mendez, C, Doert, M, Dominis Prester, D, Dorner, D, Doro, M, Einecke, S, Eisenacher, D, Elsaesser, D, Fonseca, M V, Font, L, Frantzen, K, Fruck, C, Galindo, D, García López, R J, Garczarczyk, M, Garrido Terrats, D, Gaug, M, Godinović, N, González Muñoz, A, Gozzini, S R, Hadasch, D, Hanabata, Y, Hayashida, M, Herrera, J, Hildebrand, D, Hose, J, Hrupec, D, Idec, W, Kadenius, V, Kellermann, H, Kodani, K, Konno, Y, Krause, J, Kubo, H, Kushida, J, La Barbera, A, Lelas, D, Lewandowska, N, Lindfors, E, Lombardi, S, López, M, López-Coto, R, López-Oramas, A, Lorenz, E, Lozano, I, Makariev, M, Mallot, K, Maneva, G, Mankuzhiyil, N, Mannheim, K, Maraschi, L, Marcote, B, Mariotti, M, Martínez, M, Mazin, D, Menzel, U, Miranda, J M, Mirzoyan, R, Moralejo, A, Munar-Adrover, P, Nakajima, D, Niedzwiecki, A, Nilsson, K, Nishijima, K, Noda, K, Nowak, N, Orito, R, Overkemping, A, Paiano, S, Palatiello, M, Paneque, D, Paoletti, R, Paredes, J M, Paredes-Fortuny, X, Persic, M, Prada Moroni, P G, Prandini, E, Preziuso, S, Puljak, I, Reinthal, R, Rhode, W, Ribó, M, Rico, J, Rodriguez Garcia, J, Rügamer, S, Saggion, A, Saito, T, Saito, K, Satalecka, K, Scalzotto, V, Scapin, V, Schultz, C, Schweizer, T, Shore, S N, Sillanpää, A, Sitarek, J, Snidaric, I, Sobczynska, D, Spanier, F, Stamatescu, V, Stamerra, A, Steinbring, T, Storz, J, Strzys, M, Takalo, L, Takami, H, Tavecchio, F, Temnikov, P, Terzić, T, Tescaro, D, Teshima, M, Thaele, J, Tibolla, O, Torres, D F, Toyama, T, Treves, A, Uellenbeck, M, Vogler, P, Wagner, R M, Zanin, R, Horns, D, Martín, J, and Meyer, M (2015). Measurement of the Crab Nebula spectrum over three decades in energy with the MAGIC telescopes. *Journal of High Energy Astrophysics*, 5-6:30–38.

Alfaro, R., González, M., Dichiara, S., Iriarte, A., Garfias, F., Bernal, A., Martínez, L., Torres, I., Tovmassian, G., Dorner, D., Bretz, T., Nellen, L., Hiriart, D., and Jimenez, E. (2017). Monitoring at TeV Energies with M@TE. *PoS*, ICRC2017.

Aliu, E., Anderhub, H., Antonelli, L. A., Antoranz, P., Backes, M., Baixeras, C., Barrio, J. A., Bartko, H., Bastieri, D., Becker, J. K., Bednarek, W., Berger, K., Bernardini, E., Bigongiari, C., Biland, A., Bock, R. K., Bonnoli, G., Bordas, P., Bosch-Ramon, V., Bretz, T., Britvitch, I., Camara, M., Carmona, E., Chilingarian, A., Commichau, S., Contreras, J. L., Cortina, J., Costado, M. T., Covino, S., Curtef, V., Dazzi, F.,

De Angelis, A., De Cea del Pozo, E., de los Reyes, R., De Lotto, B., De Maria, M., De Sabata, F., Delgado Mendez, C., Dominguez, A., Dorner, D., Doro, M., Elsässer, D., Errando, M., Fagiolini, M., Ferenc, D., Fernandez, E., Firpo, R., Fonseca, M. V., Font, L., Galante, N., Garcia Lopez, R. J., Garczarczyk, M., Gaug, M., Goebel, F., Hadasch, D., Hayashida, M., Herrero, A., Höhne, D., Hose, J., Hsu, C. C., Huber, S., Jogler, T., Kranich, D., La Barbera, A., Laille, A., Leonardo, E., Lindfors, E., Lombardi, S., Longo, F., Lopez, M., Lorenz, E., Majumdar, P., Maneva, G., Mankuzhiyil, N., Mannheim, K., Maraschi, L., Mariotti, M., Martinez, M., Mazin, D., Meucci, M., Meyer, M., Miranda, J. M., Mirzoyan, R., Moles, M., Moralejo, A., Nieto, D., Nilsson, K., Ninkovic, J., Otte, N., Oya, I., Paoletti, R., Paredes, J. M., Pasanen, M., Pascoli, D., Pauss, F., Pegna, R. G., Perez-Torres, M. A., Persic, M., Peruzzo, L., Piccioli, A., Prada, F., Prandini, E., Puchades, N., Raymers, A., Rhode, W., Ribó, M., Rico, J., Rissi, M., Robert, A., Rügamer, S., Saggion, A., Saito, T. Y., Salvati, M., Sanchez-Conde, M., Sartori, P., Satalecka, K., Scalzotto, V., Scapin, V., Schweizer, T., Shayduk, M., Shinozaki, K., Shore, S. N., Sidro, N., Sierpowska-Bartosik, A., Sillanpää, A., Sobczynska, D., Spanier, F., Stamerra, A., Stark, L. S., Takalo, L., Tavecchio, F., Temnikov, P., Tescaro, D., Teshima, M., Tluczykont, M., Torres, D. F., Turini, N., Vankov, H., Venturini, A., Vitale, V., Wagner, R. M., Wittek, W., Zabalza, V., Zandanel, F., Zanin, R., Zapatero, J., de Jager, O. C., de Ona Wilhelmi, E., and MAGIC Collaboration (2008). Observation of Pulsed γ-Rays Above 25 GeV from the Crab Pulsar with MAGIC. *Science*, 322:1221.

Anderhub, H., Backes, M., Biland, A., Boccone, V., Braun, I., Bretz, T., Buß, J., Cadoux, F., Commichau, V., Djambazov, L., Dorner, D., Einecke, S., Eisenacher, D., Gendotti, A., Grimm, O., von Gunten, H., Haller, C., Hildebrand, D., Horisberger, U., Huber, B., Kim, K. S., Knoetig, M. L., Köhne, J. H., Krähenbühl, T., Krumm, B., Lee, M., Lorenz, E., Lustermann, W., Lyard, E., Mannheim, K., Meharga, M., Meier, K., Montaruli, T., Neise, D., Nessi-Tedaldi, F., Overkemping, A. K., Paravac, A., Pauss, F., Renker, D., Rhode, W., Ribordy, M., Röser, U., Stucki, J. P., Schneider, J., Steinbring, T., Temme, F., Thaele, J., Tobler, S., Viertel, G., Vogler, P., Walter, R., Warda, K., Weitzel, Q., and Zänglein, M. (2013). Design and operation of fact - the first g-apd cherenkov telescope. *Journal of Instrumentation*, 8(06):P06008.

Arens, T., Hettlich, F., Karpfinger, C., Kockelkorn, U., Lichtenegger, K., and Stachel, H. (2015). *Mathematik*. Springer-Verlag.

Atwood, W. B., Abdo, A. A., Ackermann, M., Althouse, W., Anderson, B., Axelsson, M., Baldini, L., Ballet, J., Band, D. L., Barbiellini, G., and et al. (2009). The Large Area Telescope on the Fermi Gamma-Ray Space Telescope Mission. *The Astrophysical Journal*, 697:1071–1102.

Auger, P., Ehrenfest, P., Maze, R., Daudin, J., and Fréon, R. A. (1939). Extensive Cosmic-Ray Showers. *Reviews of Modern Physics*, 11:288–291.

Begelman, M. C., Blandford, R. D., and Rees, M. J. (1980). Massive black hole binaries in active galactic nuclei. *Nature*, 287:307–309.

Bennett, A. S. and Simth, F. G. (1962). The preparation of the revised 3c catalogue of radio sources. *Monthly Notices of the Royal Astronomical Society*, 125(1):75–86.

Berge, D., Funk, S., and Hinton, J. (2007). Background modelling in very-high-energy gamma-ray astronomy. *Astronomy & Astrophysics*, 466(3):1219–1229.

Biland, A., Bretz, T., Buß, J., Commichau, V., Djambazov, L., Dorner, D., Einecke, S., Eisenacher, D., Freiwald, J., Grimm, O., von Gunten, H., Haller, C., Hempfling, C., Hildebrand, D., Hughes, G., Horisberger, U., Knoetig, M. L., Krähenbühl, T., Lustermann, W., Lyard, E., Mannheim, K., Meier, K., Mueller, S., Neise, D., Overkemping, A. K., Paravac, A., Pauss, F., Rhode, W., Röser, U., Stucki, J. P., Steinbring, T., Temme, F., Thaele, J., Vogler, P., Walter, R., and Weitzel, Q. (2014). Calibration and performance of the photon sensor response of fact — the first g-apd cherenkov telescope. *Journal of Instrumentation*, 9(10):P10012.

Biland, A. et al. (2016). FACT - Status and Experience from Three Years Operation of the First SiPM Camera. *PoS*, ICRC2015:1032.

Bretz, T., Anderhub, H., Backes, M., Biland, A., Boccone, V., Braun, I., Buss, J., Cadoux, F., Commichau, V., Djambazov, L., et al. (2013). Fact-the first g-apd cherenkov telescope: Status and results. *arXiv preprint arXiv:1308.1512*.

Catanese, M. and Weekes, T. C. (1999). Very high energy gamma-ray astronomy. *Publications of the Astronomical Society of the Pacific*, 111(764):1193.

Connolly, S. D. (2016). DELightcurveSimulation: Light curve simulation code. Astrophysics Source Code Library.

Coutiño de León, S., Carramiñana, A., Rosa-González, D., and for the HAWC collaboration (2017). Spectral analysis of Markarian 421 and Markarian 501 with HAWC. *ArXiv e-prints*.

Dawson, B. R., Fukushima, M., and Sokolsky, P. (2017). Past, Present and Future of UHECR Observations. *ArXiv e-prints*.

de Naurois, M. and H.E.S.S. Collaboration (2013). The Galactic Sky seen by H.E.S.S. *Advances in Space Research*, 51:258–267.

de Naurois, M. and Mazin, D. (2015). Ground-based detectors in very-high-energy gamma-ray astronomy. *Comptes Rendus Physique*, 16:610–627.

Deeming, T. J. (1975). Fourier analysis with unequally-spaced data. *Astrophysics and Space Science*, 36(1):137–158.

Dorner, D., Bretz, T., González, M., Alfaro, R., and Tovmassian, G. (2016). M@TE - Monitoring at TeV Energies. *ArXiv e-prints*.

Dorner, D. and Lauer, R. (2017). Joint analysis of TeV blazar light curves with FACT and HAWC. *PoS*, ICRC2017.

Edge, D. O., Shakeshaft, J. R., McAdam, W. B., Baldwin, J. E., and Archer, S. (1959). A survey of radio sources at a frequency of 159 Mc/s. *Memoirs of the Royal Astronomical Society*, 68:37–60.

Emmanoulopoulos, D., McHardy, I. M., and Papadakis, I. E. (2013). Generating artificial light curves: revisited and updated. *Monthly Notices of the Royal Astronomical Society*, 433(2):907–927.

Eyer, L. and Bartholdi, P. (1999). Variable stars: Which Nyquist frequency? *Astronomy and Astrophysics, Supplement*, 135:1–3.

Firpo, R. (2006). *Study of MAGIC telescope sensitivity for large zenith angle observations.* PhD thesis.

Frick, P., Galyagin, D., Hoyt, D. V., Nesme-Ribes, E., Schatten, K. H., Sokoloff, D., and Zakharov, V. (1997). Wavelet analysis of solar activity recorded by sunspot groups. *Astronomy and Astrophysics*, 328:670–681.

Gillon, M., Triaud, A. H. M. J., Demory, B.-O., Jehin, E., Agol, E., Deck, K. M., Lederer, S. M., de Wit, J., Burdanov, A., Ingalls, J. G., Bolmont, E., Leconte, J., Raymond, S. N., Selsis, F., Turbet, M., Barkaoui, K., Burgasser, A., Burleigh, M. R., Carey, S. J., Chaushev, A., Copperwheat, C. M., Delrez, L., Fernandes, C. S., Holdsworth, D. L., Kotze, E. J., Van Grootel, V., Almleaky, Y., Benkhaldoun, Z., Magain, P., and Queloz, D. (2017). Seven temperate terrestrial planets around the nearby ultracool dwarf star TRAPPIST-1. *Nature*, 542(7642):456–460.

Green, D. A. and Stephenson, F. R. (2003). Historical Supernovae. In Weiler, K., editor, *Supernovae and Gamma-Ray Bursters*, volume 598 of *Lecture Notes in Physics, Berlin Springer Verlag*, pages 7–19.

Greisen, K. (1960). Cosmic ray showers. *Annual Review of Nuclear Science*, 10(1):63–108.

Heckman, T. M. and Best, P. N. (2014). The Coevolution of Galaxies and Supermassive Black Holes: Insights from Surveys of the Contemporary Universe. *Annual Review of Astronomy and Astrophysics*, 52:589–660.

Heitler, W. (1954). *The quantum theory of radiation.* Courier Corporation.

Hess, V. F. (1912). Uber beobachtungen der durchdringenden strahlung bei sieben freiballonfahrten. *Phys. Zeits.*, 13:1084–1091.

H.E.S.S. Collaboration (2016). Characterizing the gamma-ray long-term variability of pks 2155-304 with hess and fermi-lat. *arXiv preprint arXiv:1610.03311*.

H.E.S.S. Collaboration, Abramowski, A., Acero, F., Aharonian, F., Akhperjanian, A. G., Anton, G., Barres de Almeida, U., Bazer-Bachi, A. R., Becherini, B., Y. B., Benbow, W., Bernlöhr, K., Bochow, A., Boisson, C., Bolmont, J., Borrel, V., Brucker, J., Brun, F., Brun, P., Bühler, R., Bulik, T., Büsching, I., Boutelier, T., Chadwick, P. M., Charbonnier, A., Chaves, R. C. G., Cheesebrough, A., Chounet, L.-M., Clapson, A. C., Coignet, G., Conrad, J., Costamante, L., Dalton, M., Daniel, M. K., Davids, I. D., Degrange, B., Deil, C., Dickinson, H. J., Djannati-Ataï, A., Domainko, W., O'C. Drury, L., Dubois, F., Dubus, G., Dyks, J., Dyrda, M., Egberts, K., Eger, P., Espigat, P., Fallon, L., Farnier, C., Fegan, S., Feinstein, F., Fernandes, M. V., Fiasson, A., Förster, A., Fontaine, G., Füßling, M., Gabici, S., Gallant, Y. A., Gérard, L.,

Gerbig, D., Giebels, B., Glicenstein, J. F., Glück, B., Goret, P., Göring, D., Hampf, D., Hauser, M., Heinz, S., Heinzelmann, G., Henri, G., Hermann, G., Hinton, J. A., Hoffmann, A., Hofmann, W., Hofverberg, P., Holleran, M., Hoppe, S., Horns, D., Jacholkowska, A., de Jager, O. C., Jahn, C., Jung, I., Katarzyński, K., Katz, U., Kaufmann, S., Kerschhaggl, M., Khangulyan, D., Khélifi, B., Keogh, D., Klochkov, D., Kluźniak, W., Kneiske, T., Komin, N., Kosack, K., Kossakowski, R., Lamanna, G., Lenain, J.-P., Lohse, T., Lu, C.-C., Marandon, V., Marcowith, A., Masbou, J., Maurin, D., McComb, T. J. L., Medina, M. C., Méhault, J., Moderski, R., Moulin, E., Naumann-Godo, M., de Naurois, M., Nedbal, D., Nekrassov, D., Nguyen, N., Nicholas, B., Niemiec, J., Nolan, S. J., Ohm, S., Olive, J.-F., de Oña Wilhelmi, E., Opitz, B., Orford, K. J., Ostrowski, M., Panter, M., Paz Arribas, M., Pedaletti, G., Pelletier, G., Petrucci, P.-O., Pita, S., Pühlhofer, G., Punch, M., Quirrenbach, A., Raubenheimer, B. C., Raue, M., Rayner, S. M., Reimer, O., Renaud, M., de los Reyes, R., Rieger, F., Ripken, J., Rob, L., Rosier-Lees, S., Rowell, G., Rudak, B., Rulten, C. B., Ruppel, J., Ryde, F., Sahakian, V., Santangelo, A., Schlickeiser, R., Schöck, F. M., Schönwald, A., Schwanke, U., Schwarzburg, S., Schwemmer, S., Shalchi, A., Sushch, I., Sikora, M., Skilton, J. L., Sol, H., Stawarz, Ł., Steenkamp, R., Stegmann, C., Stinzing, F., Superina, G., Szostek, A., Tam, P. H., Tavernet, J.-P., Terrier, R., Tibolla, O., Tluczykont, M., Valerius, K., van Eldik, C., Vasileiadis, G., Venter, C., Venter, L., Vialle, J. P., Viana, A., Vincent, P., Vivier, M., Völk, H. J., Volpe, F., Vorobiov, S., Wagner, S. J., Ward, M., Zdziarski, A. A., Zech, A., and Zechlin, H. S. (2010). VHE γ-ray emission of PKS 2155-304: spectral and temporal variability. *Astronomy and Astrophysics*, 520:A83.

Hester, J. J. (2008). The Crab Nebula: An Astrophysical Chimera. *Annual Review of Astronomy and Astrophysics*.

Hillas, A. M. (1985). Cerenkov light images of EAS produced by primary gamma. *International Cosmic Ray Conference*, 3.

Hofmann, W. (2000). The high energy stereoscopic system (hess) project. *AIP Conference Proceedings*, 515(1):500–509.

Honma, F., Matsumoto, R., and Kato, S. (1992). Pulsational instability of relativistic accretion disks and its connection to the periodic X-ray time variability of NGC 6814. *Publications of the Astronomical Society of Japan*, 44:529–535.

Horan, D., Acciari, V. A., Bradbury, S. M., Buckley, J. H., Bugaev, V., Byrum, K. L., Cannon, A., Celik, O., Cesarini, A., Chow, Y. C. K., Ciupik, L., Cogan, P., Falcone, A. D., Fegan, S. J., Finley, J. P., Fortin, P., Fortson, L. F., Gall, D., Gillanders, G. H., Grube, J., Gyuk, G., Hanna, D., Hays, E., Kertzman, M., Kildea, J., Konopelko, A., Krawczynski, H., Krennrich, F., Lang, M. J., Lee, K., Moriarty, P., Nagai, T., Niemiec, J., Ong, R. A., Perkins, J. S., Pohl, M., Quinn, J., Reynolds, P. T., Rose, H. J., Sembroski, G. H., Smith, A. W., Steele, D., Swordy, S. P., Toner, J. A., Vassiliev, V. V., Wakely, S. P., Weekes, T. C., White, R. J., Williams, D. A., Wood, M. D., Zitzer, B., Aller, H. D., Aller, M. F., Baker, M., Barnaby, D., Carini, M. T., Charlot, P., Dumm, J. P., Fields, N. E., Hovatta, T., Jordan, B., Kovalev, Y. A., Kovalev, Y. Y., Krimm, H. A., Kurtanidze, O. M., Lähteenmäki, A., LeCampion, J. F., Maune, J., Montaruli, T., Sadun, A. C., Smith, S., Tornikoski, M., Turunen,

M., and Walters, R. (2009). Multiwavelength Observations of Markarian 421 in 2005-2006. *The Astrophysical Journal*, 695:596–618.

Horan, D. and Weekes, T. C. (2003). Extragalactic Sources of TeV Gamma Rays: A Summary. *arXiv.org*.

Huppenkothen, D., Watts, A. L., Uttley, P., van der Horst, A. J., van der Klis, M., Kouveliotou, C., Göğüş, E., Granot, J., Vaughan, S., and Finger, M. H. (2013). Quasi-periodic Oscillations and Broadband Variability in Short Magnetar Bursts. *The Astrophysical Journal*, 768(1):87.

Ivezić, Ž., Connolly, A. J., VanderPlas, J. T., and Gray, A. (2014). *Statistics, Data Mining, and Machine Learning in Astronomy: A Practical Python Guide for the Analysis of Survey Data.* Princeton University Press.

Karttunen, H., Kröger, P., Oja, H., Poutanen, M., and Donner, K. J. (2007). *Fundamental astronomy.* Springer.

Kim, D.-W., Protopapas, P., Bailer-Jones, C. A. L., Byun, Y.-I., Chang, S.-W., Marquette, J.-B., and Shin, M.-S. (2014). The EPOCH Project. I. Periodic variable stars in the EROS-2 LMC database. *Astronomy and Astrophysics*, 566:A43.

Knoetig, M. L., Biland, A., Bretz, T., Buß, J., Dorner, D., Einecke, S., Eisenacher, D., Hildebrand, D., Krähenbühl, T., Lustermann, W., Mannheim, K., Meier, K., Neise, D., Overkemping, A.-K., Paravac, A., Pauss, F., Rhode, W., Ribordy, M., Steinbring, T., Temme, F., Thaele, J., Vogler, P., Walter, R., Weitzel, Q., and Zänglein, M. (2013). FACT - Long-term stability and observations during strong Moon light. *ArXiv e-prints*.

Komossa, S. (2003). Observational evidence for supermassive black hole binaries. In Centrella, J. M., editor, *The Astrophysics of Gravitational Wave Sources*, volume 686 of *American Institute of Physics Conference Series*, pages 161–174.

Kranich, D. (2001). *Temporal and spectral characteristics of the active galactic nucleus Mkn 501 during a phase of high activity in the TeV range.* PhD thesis, Technische Universität München.

Lauer, R. J. (2016). Monitoring the Variable Gamma-Ray Sky with HAWC. *ArXiv e-prints*.

Li, T.-P. and Ma, Y.-Q. (1983). Analysis methods for results in gamma-ray astronomy. *The Astrophysical Journal*, 272:317–324.

Lomb, N. R. (1976). Least-squares frequency analysis of unequally spaced data. *Astrophysics and Space Science*, 39(2):447–462.

Lorenz, E. and Wagner, R. (2012). Very-High Energy Gamma-Ray Astronomy: A 23-Year Success Story in Astroparticle Physics. In *From Ultra Rays to Astroparticles*, pages 143–185. Springer Netherlands, Dordrecht.

Mahlke, M., Bretz, T., and Collaboration, F. (2017). Fact - searching for periodicity in five-year light-curves of active galactic nuclei. In *PoS - ICRC 2017*.

Marscher, A. P. (2005). The relationship between radio and higher-frequency emission in active galactic nuclei. *Memorie della Societa Astronomica Italiana*, 76:13.

Marscher, A. P. (2006). Relativistic jets in active galactic nuclei. In *AIP Conference Proceedings*, volume 856, pages 1–22. AIP.

McEnery, J., Bond, I. H., Boyle, P. J., Bradbury, S. M., Breslin, A. C., Buckley, J. H., Burdett, A., Bussons Gordo, J., Carter-Lewis, D. A., Catanese, M. A., Cawley, M. F., Fegan, D. J., Finley, J. P., Gaidos, J. A., Hall, A., Hillas, A. M., Krennrich, F., Lamb, R. C., Lessard, R. W., Masterson, C., Mohanty, G., Moriarty, P., Quinn, J., Rodgers, A. J., Rose, H. J., Samuelson, F. W., Sembroski, G. H., Srinivasan, R., Weekes, T. C., and Zweerink, J. A. (1997). TeV Observations of the Variability and Spectrum of Markarian 421. *International Cosmic Ray Conference*, 3:257.

Mostafa, M. (2013). The High Altitude Water Cherenkov Observatory. *ArXiv e-prints*.

Netzer, H. (2015). Revisiting the Unified Model of Active Galactic Nuclei. *arXiv.org*, pages 365–408.

Nishikawa, D. and The Utah Seven Telescope Array collaboration (1999). Periodicity in the TeV gamma rays and X rays from Markarian 501. *ArXiv Astrophysics e-prints*.

Papadakis, I. E. and Lawrence, A. (1993). Improved methods for power spectrum modelling of red noise. *Monthly Notices of the Royal Astronomical Society*, 261(3):612–624.

Parzen, E. (1962). On estimation of a probability density function and mode. *The annals of mathematical statistics*, 33(3):1065–1076.

Press, W. H. (1978). Flicker noises in astronomy and elsewhere. *Comments on Modern Physics*, 7:103–119.

Priestley, M. B. (1981). *Spectral analysis and time series*. Academic Press, London.

Punch, M., Akerlof, C. W., Cawley, M. F., Chantell, M., Fegan, D. J., Fennell, S., Gaidos, J. A., Hagan, J., Hillas, A. M., Jiang, Y., Kerrick, A. D., Lamb, R. C., Lawrence, M. A., Lewis, D. A., Meyer, D. I., Mohanty, G., O'Flaherty, K. S., Reynolds, P. T., Rovero, A. C., Schubnell, M. S., Sembroski, G., Weekes, T. C., Whitaker, T., and Wilson, C. (1992). Detection of TeV photons from the active galaxy Markarian 421. *Nature*, 358(6386):477–478.

Quinn, J., Akerlof, C. W., Biller, S., Buckley, J., Carter-Lewis, D. A., Cawley, M. F., Catanese, M., Connaughton, V., Fegan, D. J., Finley, J. P., Gaidos, J., Hillas, A. M., Lamb, R. C., Krennrich, F., Lessard, R., McEnery, J. E., Meyer, D. I., Mohanty, G., Rodgers, A. J., Rose, H. J., Sembroski, G., Schubnell, M. S., Weekes, T. C., Wilson, C., and Zweerink, J. (1996). Detection of Gamma Rays with E > 300 GeV from Markarian 501. *The Astrophysical Journal*, 456:L83.

Rieger, F. M. (2004). On the Geometrical Origin of Periodicity in Blazar-type Sources. *The Astrophysical Journal*, 615(1):L5–L8.

Rieger, F. M. and Mannheim, K. (2003). On the central black hole mass in Mkn 501. *Astronomy and Astrophysics*, 397:121–125.

Romero, G. E., Boettcher, M., Markoff, S., and Tavecchio, F. (2017). Relativistic Jets in Active Galactic Nuclei and Microquasars. *Space Science Reviews*, 207:5–61.

Ruan, J. J., Anderson, S. F., MacLeod, C. L., Becker, A. C., Burnett, T. H., Davenport, J. R. A., Ivezić, Ž., Kochanek, C. S., Plotkin, R. M., Sesar, B., and Stuart, J. S. (2012). Characterizing the Optical Variability of Bright Blazars: Variability-based Selection of Fermi Active Galactic Nuclei. *The Astrophysical Journal*, 760:51.

Sahu, S., Miranda, L. S., and Rajpoot, S. (2016). Multi-TeV flaring from blazars: Markarian 421 as a case study. *European Physical Journal C*, 76:127.

Sambruna, R. M. (2006). High-energy Variability of Blazars. In Miller, H. R., Marshall, K., Webb, J. R., and Aller, M. F., editors, *Blazar Variability Workshop II: Entering the GLAST Era*, volume 350 of *Astronomical Society of the Pacific Conference Series*, page 86.

Scargle, J. D. (1982). Studies in astronomical time series analysis. ii-statistical aspects of spectral analysis of unevenly spaced data. *The Astrophysical Journal*, 263:835–853.

Schmidt, M. (1963). 3C 273 : A Star-Like Object with Large Red-Shift. *Nature*, 197(4872):1040–1040.

Schreiber, T. and Schmitz, A. (1996). Improved surrogate data for nonlinearity tests. *Phys. Rev. Lett.*, 77:635–638.

Schuster, A. (1898). On the investigation of hidden periodicities with application to a supposed 26 day period of meteorological phenomena. *Terrestrial Magnetism*, 3(1):13–41.

Schwabe, M. (1844). Sonnenbeobachtungen im jahre 1843. von herrn hofrath schwabe in dessau. *Astronomische Nachrichten*, 21:233.

Spurio, M. (2014). *Particles and Astrophysics - A Multi-Messenger Approach*. Springer.

Tavani, M., Bulgarelli, A., Vittorini, V., Pellizzoni, A., Striani, E., Caraveo, P., Weisskopf, M. C., Tennant, A., Pucella, G., Trois, A., Costa, E., Evangelista, Y., Pittori, C., Verrecchia, F., Del Monte, E., Campana, R., Pilia, M., De Luca, A., Donnarumma, I., Horns, D., Ferrigno, C., Heinke, C. O., Trifoglio, M., Gianotti, F., Vercellone, S., Argan, A., Barbiellini, G., Cattaneo, P. W., Chen, A. W., Contessi, T., D'Ammando, F., DeParis, G., Di Cocco, G., Di Persio, G., Feroci, M., Ferrari, A., Galli, M., Giuliani, A., Giusti, M., Labanti, C., Lapshov, I., Lazzarotto, F., Lipari, P., Longo, F., Fuschino, F., Marisaldi, M., Mereghetti, S., Morelli, E., Moretti, E., Morselli, A., Pacciani, L., Perotti, F., Piano, G., Picozza, P., Prest, M., Rapisarda, M., Rappoldi, A., Rubini, A., Sabatini, S., Soffitta, P., Vallazza, E., Zambra, A., Zanello, D., Lucarelli, F., Santolamazza, P., Giommi, P., Salotti, L., and Bignami, G. F. (2011). Discovery of Powerful Gamma-Ray Flares from the Crab Nebula. *Science*, 331:736.

Timmer, J. and König, M. (1995). On generating power law noise. *Astronomy and Astrophysics*, 300:707.

Tridon, D. B., Schweizer, T., Goebel, F., Mirzoyan, R., Teshima, M., collaboration, M., et al. (2010). The magic-ii gamma-ray stereoscopic telescope system. *Nuclear Instruments and Methods in Physics Research Section A: Accelerators, Spectrometers, Detectors and Associated Equipment*, 623(1):437–439.

Ulrich, M.-H., Kinman, T. D., Lynds, C. R., Rieke, G. H., and Ekers, R. D. (1975). Non-thermal continuum radiation in three elliptical galaxies. *The Astrophysical Journal*, 198:261–266.

Ulrich, M.-H., Maraschi, L., and Urry, C. M. (1997). Variability of active galactic nuclei. *Annual Review of Astronomy and Astrophysics*, 35(1):445–502.

Urry, C. M. and Padovani, P. (1995). Unified Schemes for Radio-Loud Active Galactic Nuclei. *arXiv.org*, (715):803.

Uttley, P., McHardy, I., and Papadakis, I. (2002). Measuring the broad-band power spectra of active galactic nuclei with rxte. *Monthly Notices of the Royal Astronomical Society*, 332(1):231–250.

Uttley, P. and McHardy, I. M. (2001). The flux-dependent amplitude of broadband noise variability in X-ray binaries and active galaxies. *arXiv.org*, (2):L26–L30.

VanderPlas, J. T. (2017). Understanding the Lomb-Scargle Periodogram. *ArXiv e-prints*.

Vaughan, S. (2005). A simple test for periodic signals in red noise. *Astronomy & Astrophysics*, 431(1):391–403.

Vaughan, S., Edelson, R., Warwick, R., and Uttley, P. (2003). On characterizing the variability properties of x-ray light curves from active galaxies. *Monthly Notices of the Royal Astronomical Society*, 345(4):1271–1284.

Weekes, T. C., Cawley, M. F., Fegan, D. J., Gibbs, K. G., Hillas, A. M., Kowk, P. W., Lamb, R. C., Lewis, D. A., Macomb, D., Porter, N. A., Reynolds, P. T., and Vacanti, G. (1989). Observation of TeV gamma rays from the Crab nebula using the atmospheric Cerenkov imaging technique. *The Astrophysical Journal*, 342:379–395.

Wijnands, R. and van der Klis, M. (1999). The broadband power spectra of x-ray binaries. *The Astrophysical Journal*, 514(2):939.

Zechmeister, M. and Kürster, M. (2009). The generalised lomb-scargle periodogram- a new formalism for the floating-mean and keplerian periodograms. *Astronomy & Astrophysics*, 496(2):577–584.

ACKNOWLEDGEMENTS

Eidesstattliche Versicherung
Statutory Declaration in Lieu of an Oath

_____   _____

Name, Vorname/Last Name, First Name   Matrikelnummer (freiwillige Angabe)
Matriculation No. (optional)

Ich versichere hiermit an Eides Statt, dass ich die vorliegende Arbeit/Bachelorarbeit/
Masterarbeit* mit dem Titel
I hereby declare in lieu of an oath that I have completed the present paper/Bachelor thesis/Master thesis* entitled

_____

_____

_____

selbstständig und ohne unzulässige fremde Hilfe erbracht habe. Ich habe keine anderen als die angegebenen Quellen und Hilfsmittel benutzt. Für den Fall, dass die Arbeit zusätzlich auf einem Datenträger eingereicht wird, erkläre ich, dass die schriftliche und die elektronische Form vollständig übereinstimmen. Die Arbeit hat in gleicher oder ähnlicher Form noch keiner Prüfungsbehörde vorgelegen.

independently and without illegitimate assistance from third parties. I have used no other than the specified sources and aids. In case that the thesis is additionally submitted in an electronic format, I declare that the written and electronic versions are fully identical. The thesis has not been submitted to any examination body in this, or similar, form.

_____   _____

Ort, Datum/City, Date   Unterschrift/Signature

*Nichtzutreffendes bitte streichen
*Please delete as appropriate

Belehrung:
Official Notification:

§ 156 StGB: Falsche Versicherung an Eides Statt
Wer vor einer zur Abnahme einer Versicherung an Eides Statt zuständigen Behörde eine solche Versicherung falsch abgibt oder unter Berufung auf eine solche Versicherung falsch aussagt, wird mit Freiheitsstrafe bis zu drei Jahren oder mit Geldstrafe bestraft.
Para. 156 StGB (German Criminal Code): False Statutory Declarations
Whoever before a public authority competent to administer statutory declarations falsely makes such a declaration or falsely testifies while referring to such a declaration shall be liable to imprisonment not exceeding three years or a fine.
§ 161 StGB: Fahrlässiger Falscheid; fahrlässige falsche Versicherung an Eides Statt
(1) Wenn eine der in den §§ 154 bis 156 bezeichneten Handlungen aus Fahrlässigkeit begangen worden ist, so tritt Freiheitsstrafe bis zu einem Jahr oder Geldstrafe ein.
(2) Straflosigkeit tritt ein, wenn der Täter die falsche Angabe rechtzeitig berichtigt. Die Vorschriften des § 158 Abs. 2 und 3 gelten entsprechend.
Para. 161 StGB (German Criminal Code): False Statutory Declarations Due to Negligence
(1) If a person commits one of the offences listed in sections 154 through 156 negligently the penalty shall be imprisonment not exceeding one year or a fine.
(2) The offender shall be exempt from liability if he or she corrects their false testimony in time. The provisions of section 158 (2) and (3) shall apply accordingly.

Die vorstehende Belehrung habe ich zur Kenntnis genommen:
I have read and understood the above official notification:

_____   _____

Ort, Datum/City, Date   Unterschrift/Signature